

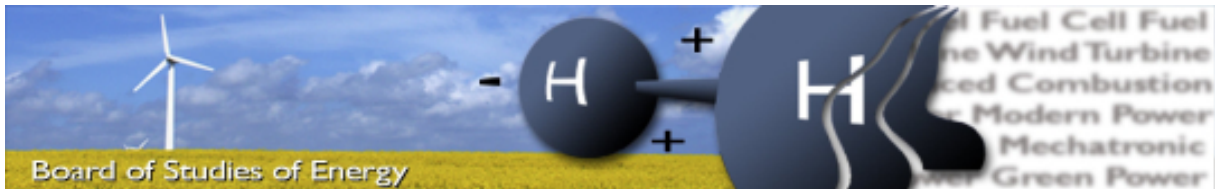
# **IMPLEMENTATION AND CONTROL OF AN INDUCTION MOTOR ON A GO-CART**



Group MCE2-822

Spring semester, 2011





**Title:** Implementation and Control of an Induction Motor on a Go-cart  
**Semester:** 2nd master semester, Mechatronic Control Engineering 2011  
**Semester theme:** Advanced control of electrical machines  
**Project period:** 01.02.11 to 25.05.11  
**ECTS:** 15  
**Supervisor:** Michael Møller Bech  
**Project group:** MCE2-822

---

Cemre Yigen

---

John Andersen

---

Mikkel P. Ehmsen

---

Anders R. Pedersen

#### SYNOPSIS:

This report deals with a combustion engine powered go-cart, that is converted into an electric vehicle supplied from a 48[V] battery pack. The new motor is a 7.3[kW], 24[Vrms] squirrel-cage induction motor. To drive the motor a Sauer-Danfoss BPI inverter is used. The motor and the mechanical load of the go-cart are modeled in *MATLAB ® Simulink*. The models are validated by comparison of simulated and measured current and rotational speed. Four different PWM methods, have been analyzed with respect to switch losses, and a strategy of switching between two is simulated. Two different control strategies have been developed and tested; Scalar and Field Oriented Vector Control. Both have performed well in the model, but only the Scalar Controller have been implemented with success in the DSP controlling the inverter. The go-cart have been converted to the electrical drive system, and in a limited final test drive, a speed of 38 [km/h] was easily achieved.

Copies: 6  
Pages, total: 122  
Appendix: 34  
Supplements: CD

**By signing this document, each member of the group confirms that all participated in the project work and thereby all members are collectively liable for the content of the report.**



# Preface

This report is written by group MCE2-822 at Aalborg University in the period 1st of February 2011 to 25th of May 2011. The report is part of the second semester master programme at the Department of Energy Engineering, and is directed to engineers and engineering students. The semester theme is “Advanced Control of Electrical Machines” covering design of mechatronic systems and components. The picture on the front page is the actual go-cart that has been the main theme for the project.

The report uses the Vancouver method for citations. On the back cover of the report is a CD, where all data sheets and MATLAB ®m-scripts and MATLAB ® Simulink models used in the report are found.



# Table of contents

<b>1</b>	<b>Introduction</b>	<b>1</b>
1.1	Initial problem statement . . . . .	3
1.2	Specifications for the product . . . . .	3
<b>2</b>	<b>System analysis</b>	<b>5</b>
2.1	Description of the go-cart . . . . .	5
2.2	General Dimensioning . . . . .	7
2.3	Inverter Design . . . . .	10
2.4	Digital Signal Processor . . . . .	17
2.5	Induction motor model . . . . .	23
2.6	Go-cart model . . . . .	34
2.7	Parameter Estimation . . . . .	36
2.8	Validation of the induction motor model . . . . .	42
2.9	Performance estimation . . . . .	47
<b>3</b>	<b>Problem statement</b>	<b>49</b>
<b>4</b>	<b>Problem solution</b>	<b>51</b>
4.1	Pulse Width Modulation of the phases . . . . .	51
4.2	SVPWM . . . . .	52
4.3	DPWM . . . . .	54
4.4	Losses from harmonic distortion and switching . . . . .	55
4.5	Switching between modulation strategies . . . . .	57
4.6	Design optimisation . . . . .	58
4.7	Scalar Control . . . . .	58
4.8	Field Oriented Control (FOC) . . . . .	68
4.9	Flux Observer . . . . .	74

<b>5 Conclusion</b>	<b>79</b>
<b>6 Future Work</b>	<b>81</b>
<b>7 Appendix</b>	<b>83</b>
.1 Inverter . . . . .	83
.2 Power supply PCB . . . . .	87
.3 Sensors . . . . .	89
.4 Derivation of the time constants for SVPWM . . . . .	94
.5 Harmonic Distortion and Switching Loss Functions . . . . .	95
.6 Derivation of the state space flux model . . . . .	96
.7 Design of motor shaft extension . . . . .	98
.8 Contents of CD . . . . .	99
<b>A Experiments</b>	<b>101</b>
A.1 DC test . . . . .	101
A.2 Voltage measurements in labview . . . . .	106
A.3 Test drive . . . . .	108

---

# Introduction

# 1

---

In the recent years there has been an increasing focus on electrically driven vehicles. Many people see the use of electric vehicles as one of the solutions to reduce the air pollution caused by combustion engines used in cars today. In 2006 there were 2.5 million registered cars in Denmark [1]. To say that the vast majority of these cars were gasoline cars won't be a big mistake, simply because of the small number of electric vehicles available on the marked.

The effects of the climate changes, which is seen around the world in the last decades, is a highly active topic for debate on all levels. Emissions of  $CO_2$  along with other greenhouse gases, which is leading to climate change, is the main subscriber for global warming. As a consequence, in United Nations it have been decided to decrease the  $CO_2$  emissions worldwide and reduce the man-made impacts on global warming [2]. According to the Kyoto Protocol, Denmark is committed to reduce its emission of greenhouse gases by up to 21 percent by the year 2012, compared to the level in 1990. Many other countries have made similar engagement.

The main part of renewable and  $CO_2$ -neutral energy source in Denmark comes from wind power and in 2009 the wind turbines produced 19.6% of the total electricity consumed in Denmark [3]. An electric car charged by wind power would not only reduce the problems with noise and air pollution in connection with engines in heavily populated areas, but would in fact also provide the user with a  $CO_2$ -neutral vehicle.

When *Tesla Motors* in 2008 released a competitive electric sport automobile, *Tesla Roadster*, it became clear that electric cars had the potential to become serious competitors to combustion engine sport cars in performance [4]. The *Tesla Roadster* is capable of driving up to 350[km] per charge, and with an acceleration from 0 – 100[km/t] in 4[s] it is comparable with more traditional super sports cars powered by combustion engines.

Building an electric car or even rebuilding a conventional car is a big task. Therefore, it is desirable for a single semester project to reduce the complexity by choosing a simpler goal. Many famous race car drivers are known to have started their career racing go-carts. A go-cart is a small open frame automobile optimized for circuit racing. The construction is very simple compared to regular cars, which gives access to enter the world of motor sport very cost effectively [5]. For competition use, on outdoor circuits the go-carts are normally powered by high performance two-stroke gasoline engines. For more recreational use, the applied engines are less maintenance demanding four-stroke engines. In that category the Danish company *Dino* supplies go-carts with 5.5[Hp] up to 13[Hp] engines [6].



Figure 1.1: *Dino* go-cart [6].

The drive cycle of a go-cart mostly consists of fast accelerations and fast deceleration (braking). Unlike a conventional car a go-cart does not need a large range per charge. As long as it can run a full heat, which lasts approximately 10 minutes, the batteries are acceptable for use. Designing an electric go-cart is therefore an interesting challenge because of the relatively simple construction and because it can be kept fairly light due to the reduced battery capacity. In addition, the climate in indoor race tracks would benefit greatly from the change from combustion to electric powered go-carts, as there are no pollution or exhaust gases. On broader perspective, the technical knowledge gained from an electrically driven go-cart , can be used in the quest for making electric vehicles more available and competitive. This will, inevitable, help to decrease  $CO_2$  emissions and prevent global warming.

## 1.1 Initial problem statement

The introduction leads to the following initial problem statement,

**What alterations and considerations are necessary to replace the combustion engine and implement an electric motor in an existing go-cart ?**

## 1.2 Specifications for the product

The go-cart should be able to function as a regular go-cart , and therefore the following set of requirements are set up for the development of the go-cart .

- The go-cart should be driven manually by a person.
- The speed of the go-cart is desired to be at least  $50[km/h]$ .
- The controls of go-cart should be controlled using an onboard Digital Signal Controller (DSC).
- The go-cart should have enough battery capacity to drive for at least  $10[min]$  before recharging is necessary.

## 1.2 Specifications for the product

---

# System analysis 2

---

## 2.1 Description of the go-cart

This section aims to quantify the demands and limitations in the process of rebuilding an existing go-cart in order to state a specific problem statement and define some design specifications. Therefore, it is necessary to describe the existing system, what alterations are to be made and which parts are left untouched. Moreover, this section contains a derivations of both the motor and the mechanical models of the go-cart.

The available go-cart is a *Dino Leisure* go-cart. The combustion engine is removed and the bare frame is used as a platform for the rebuild. The mechanical alterations on the frame, such as different mounts and brackets are omitted from the description in this report, partly because some of the mounts already have been made by other project groups, and primarily because the scope of this project is to control and drive a three phase electric motor. This means that also the existing brake and steering systems from the **Dino** go-cart are kept in the new go-cart design.

An overview of the components of the go-cart are shown in Figure 2.1

## 2.1 Description of the go-cart

---

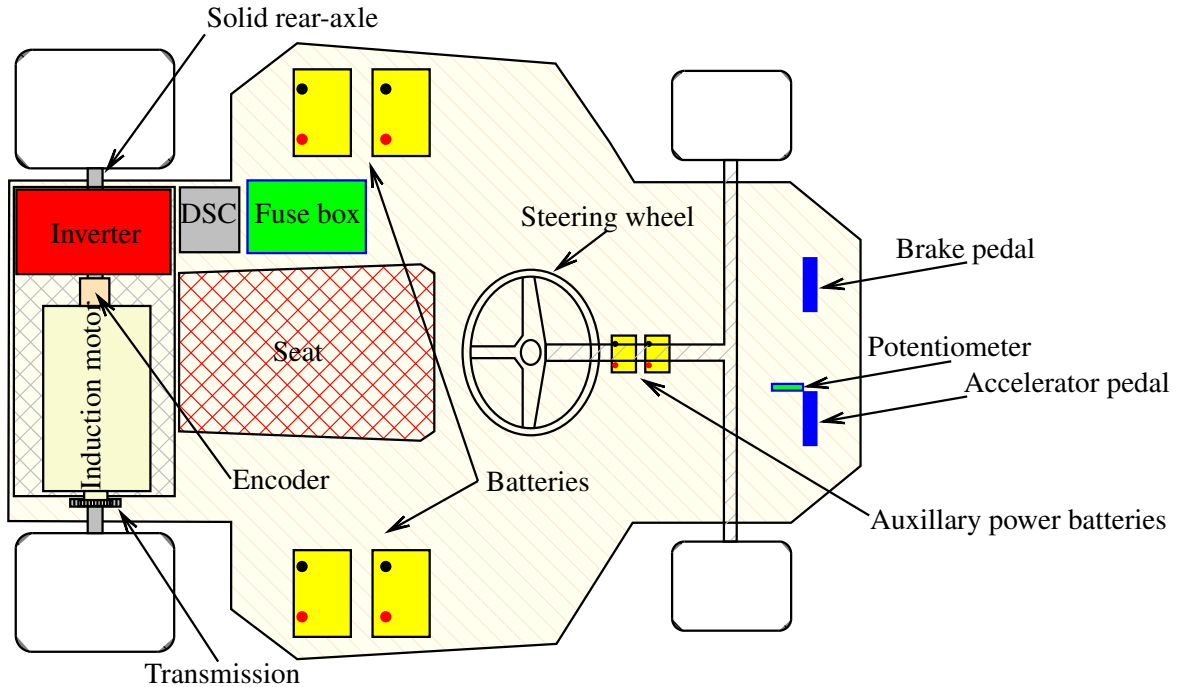


Figure 2.1: Overview of the components of the electrically driven system.

The electrically driven go-cart consists apart from the existing frame, wheels, steering, brakes, and mounts of the following major components;

- An induction motor to convert electrical power to mechanical power through magnetization.
- A transmission line to transfer rotational power (torque) from the motor to the drive shaft.
- An inverter to generate a sinusoidal signal with a controllable amplitude and frequency.
- A DSC to control the PWM signals for the inverter.
- Batteries with large capacity to supply the motor.
- Fuse box for safety and cables to handle the current drawn from the batteries.
- Auxillary power batteries to supply the electronic control circuits on the go-cart .

All these components will be considered and dimensioned in order to replace the combustion engine on the go-cart . The available electric motor to be mounted on the go-cart is a *Sauer-Danfoss* AC-motor with model number: TSA170-210-038. It is a 4-pole squirrel cage induction motor [7]. It is specifically designed for pump and traction operation on battery-powered vehicles, such as forklifts. The motor is a prototype motor hence no specific data sheet with the motor parameters is available. Therefore the motor parameters in table 2.1 are put together from partly the motor name plate and a DC test A.1. Furthermore, the motor has previously been used in other projects regarding electric vehicles at AAU, hence test results from previously performed parameter test, [8],[9] are available for this motor.

Parameter	Symbol	Value
Nominal power	$P_{nom}$	5.3[kW]
Nominal frequency	$f_{1-nom}$	58[Hz]
Nominal AC RMS voltage	$U_{s-nom}$	24[V <sub>RMS</sub> ]
Nominal winding temperature	$T_{nom-Wind}$	20[°C]
Nominal velocity	$n_{nom}$	1685[rpm]
Nominal current	$I_{nom}$	189[A]
Efficiency	$\eta$	88.7[%]
Peak power	$P_{peak}$	7.3[kW]
Phases	$m_s$	3[.]
Polepairs	$P_b$	2[.]
Moment of inertia	$J$	0.0151[kg · m <sup>2</sup> ]
Average DC resistance per phase	$R_{DC}/R_s$	2.69[mΩ]
Rotor resistance	$R_r$	2.50[mΩ]
Phase to phase resistance	$R_{Ph} - R_{Ph}$	4.01[mΩ]
Main resistance	$R_m$	1.33[Ω]
Power factor	$\cos(\phi)$	0.76
Stator inductance	$L_s$	31.16[μH]
Main inductance	$L_m$	0.38[mH]
Rotor inductance	$L_r$	31.16[μH]

Table 2.1: Data for Sauer-Danfoss AC motor.

## 2.2 General Dimensioning

To run the go-cart with the specified motor, initially, it is necessary to dimension the batteries to supply the motor and the cables to handle the current.

### 2.2.1 Batteries

The induction motor is rated to 24[V] RMS. The requirement for the batteries are to supply the rated RMS voltage is  $2 \cdot \sqrt{2} \cdot 24 = 67.9[V]$  to produce alternating voltages for the motor terminals. The energy source for the electric go-cart is chosen to be 12[V] lead acid batteries. More modern battery technologies, like *Li-ion* that are used in many new electric vehicles, offer a better energy density to weight ratio. However the low price of the lead-acid battery compared with the Li-ion type, and especially the robustness of the lead-acid type makes it well suited for the development of the electric go-cart. The chosen battery solution is 4 *Optima®* batteries connected in series with a total DC link voltage of 48[V]. Choosing 5 batteries would give a voltage range closer to the rated value, but since the batteries are to be mounted with two on each side of the driver to distribute the weight, this is not feasible in practice. These batteries are designed for engine start of combustion engines and deep-cycle applications and are furthermore very resistant to vibration and spill-proof [10]. The battery data can be seen in table 2.2.

Voltage [V]	12
Cranking Amps at 0°C[A]	870
Capacity ( $C_{20}$ rate)[Ah]	55
Internal resistance [ $\Omega$ ]	0.0028
Lengh [mm]	254
Width [mm]	175
Height [mm]	200
Weight [kg]	19.9

Table 2.2: Data for Optima®YellowTop®battery.

The capacity of 55[Ah] is given in the  $C_{20}$  standard. It is the total power reserve of the battery, defined as a constant current draw during 20 hours, until the final battery voltage is 10.5[V] for a 12[V] battery [11]. This reveals a current draw during 20 hours for the battery in table 2.2 of the size:

$$I_{C20} = \frac{\text{Capacity}[Ah]}{20[\text{hour}]} = 2.75[A] \quad (2.1)$$

The same battery would reveal different capacities according to the drawn test current. If the battery was to be tested with a smaller current for a longer time (eg.  $C_{100}$  standard), the test would reveal a larger total capacity than shown by a  $C_{20}$  standard. The opposite are to be expected when larger currents are drawn. For further calculation, the capacity of 55[Ah] will be used as it is the only value specified in the data sheet of the chosen *Optima*® battery.

To avoid interference from the motor currents drawn from the 48[V] main battery pack, the electronic control circuits on the go-cart are to be supplied from a separate auxiliary battery pack. Two 12[V], 7.2[Ah] lead acid batteries coupled in series will be adequate for the purpose. A power supply PCB containing voltage regulates for the different required voltages will have to be designed.

### 2.2.2 Fuses and cables

As a security measure the electrical system must at least include some fuses, to ensure that the batteries are not unintentionally short-circuited. A fuse acts as an inserted weak point in the system, so that if a short-circuit or over current occurs the fuse is the weakest component and breaks first, hereby protecting the circuit, see figure 2.2.

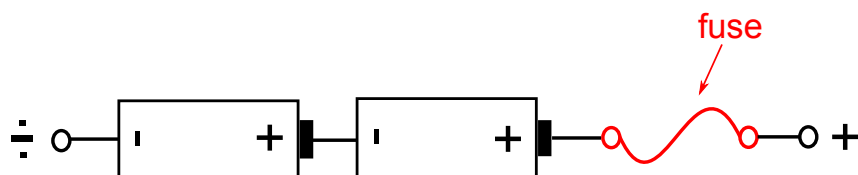


Figure 2.2: Series connected batteries with a fuse for security measures.

The cables are the means of transmitting current from the battery to the inverter and from the inverter

to the motor. The cables are to be dimensioned to carry the currents needed to drive the motor without causing a large voltage drop. These two demands calls for the cables to be as large as possible, but the essence of a go-cart is that it is a light vehicle, therefore the cables should not be larger than necessary. The nominal current of the motors name plate is 189 [A], which sets a demand for the cables to be able to carry this current. From table of maximal current in the Danish law for high voltage installations a fuse of 200 [A] demands a minimum cross sectional area of the copper wire to be 25 [ $mm^2$ ]. Electrical vehicles are not governed by this law, but the rules are a good guideline in the selection of the cables. As the cables will have a substantial length and carry up to 200 [A] the internal resistance of the cables becomes important, as the power-loss in the cables is proportional to the current squared [12].

The resistance of a wire is given by Equation A.7. The cables are roughly estimated to be 6 [m] in total. Using a 25 [ $mm^2$ ] cable yields a power-loss at rated current of  $P_{loss,c} = 145$  and a total voltage drop in the cables of  $V_{drop,w} = 0.77$ . Driving an induction machine open-loop and without control calls for a larger start-up current for the motor. A rule of thumb is up to 6 times the rated current. This calls for a larger cross-sectional area. Therefore an area of 50 [ $mm^2$ ] is selected, which is allowed to be used for up to 315 [A][12]. A 50 [ $mm^2$ ] cable reduces the power-loss and voltage drop to:  $P_{loss,c} = 72.9[W]$  and  $V_{drop,w} = 0.38[V]$  which is deemed acceptable.

### 2.2.3 Transmission

The drive line transmitting rotational power from combustion engine to the drive shaft was originally designed with two sprockets connected to each other by a chain. The drive line connection for the electric motor will be designed in the same way. Since the motor is connected directly to the drive shaft through the chain, the final gear ratio is specified only by the ration of the two sprockets. To implement the electric motor as the new power source, a new gear ratio has to be calculated based on the nominal rotational speed of the motor, and the desired nominal speed of the go-cart. It is decided that the desired nominal speed should be 50[ $km/h$ ]. With a rear wheel radius measured to be,  $R_{wheel} = 0.1375[m]$ , the rear wheels rotational speed at 50[ $km/h$ ] is calculated to be:

$$50[\text{km}/\text{h}] \cdot \frac{1000[\text{m}]}{3600[\text{s}]} = 13.89[\text{m}/\text{s}] \Rightarrow \frac{13.89}{2 \cdot \pi \cdot 0.1375} = 16.08[\text{rev}/\text{s}] = 964.58[\text{rpm}] \quad (2.2)$$

From the name plate of the Sauer-Danfoss motor it is seen that at the nominal frequency of 58[ $Hz$ ] the rotational speed is 1685[ $rpm$ ]. The required gear ratio is then calculated to be:

$$G_{ratio} = \frac{1685}{964.58} = 1.747[\cdot] \quad (2.3)$$

A chain and two gear sprockets are picked from a dealer of go-cart parts [6]. For a Leisure Line go-cart it is recommended by the dealer to use a *type 428* chain and sprockets that fits the dimensions of the chain. For the motor a sprocket with 24 teeth is chosen, and for the rear axle is chosen a 42 teeth sprocket, revealing a gear ratio very close to the desired:

$$G_{ratio} = \frac{42}{24} = 1.75[\cdot] \quad (2.4)$$

### Length of the chain

A type 428 chain has a pitch, or length of link, of  $4/8'' = 1/2'' = 12.7[mm]$ . From that the radius of the two gear sprockets can be calculated. Radius for the 24 tooth sprocket for the motor:

$$r_{24} = \frac{24[\cdot] \cdot 12.7[mm/link]}{2 \cdot \pi} = 48.51[mm] \quad (2.5)$$

And the radius for the 42 tooth sprocket for the drive shaft:

$$r_{42} = \frac{42[\cdot] \cdot 12.7[mm/link]}{2 \cdot \pi} = 84.89[mm] \quad (2.6)$$

From the radii of the sprockets and the measured height from the motor down to the drive shaft,  $h_{motor} = 280[mm]$ , the approximate length of the drive chain can be estimated:

$$l_{chain} \approx (r_{24} \cdot \pi) + (r_{42} \cdot \pi) + (2 \cdot \sqrt{h_{motor}^2 + (r_{24} - r_{42})^2}) = \quad (2.7)$$

$$(48.51 \cdot \pi) + (84.89 \cdot \pi) + (2 \cdot \sqrt{280^2 + (48.51 - 84.89)^2}) \approx 983.81[mm] \Rightarrow \quad (2.8)$$

$$\frac{983.81[mm]}{12.7[mm/link]} = 77.47[link] \quad (2.9)$$

Clearly the chain has to have an integer number of links. Due to the construction of the chain, with the links connected in pairs, it should furthermore consist of an even number of links, therefore the estimated length of the chain should be:

$$l_{chain} = 78[link] \Rightarrow 78[link] \cdot 12.7[mm/link] = 990.6[mm] \quad (2.10)$$

The design of the motor mount allows for adjustment of the height of the motor. Thereby any additional chain slack can be picked up in the final assembling process.

## 2.3 Inverter Design

The inverter is the device that converts the DC voltage from the batteries to three alternating voltages, to be connected to the motor. The basic outline of a 3 phase inverter consists of 6 transistors and 6 diodes coupled in three inverter legs. Shown in Figure 2.3. The idea is that the transistors connect the middle point of each phase leg to either + or -, and hereby creating a series of voltage pulses (PWM) of varying

duration, after a filtering (done by the motors windings) the resulting current should appear sinusoidal.

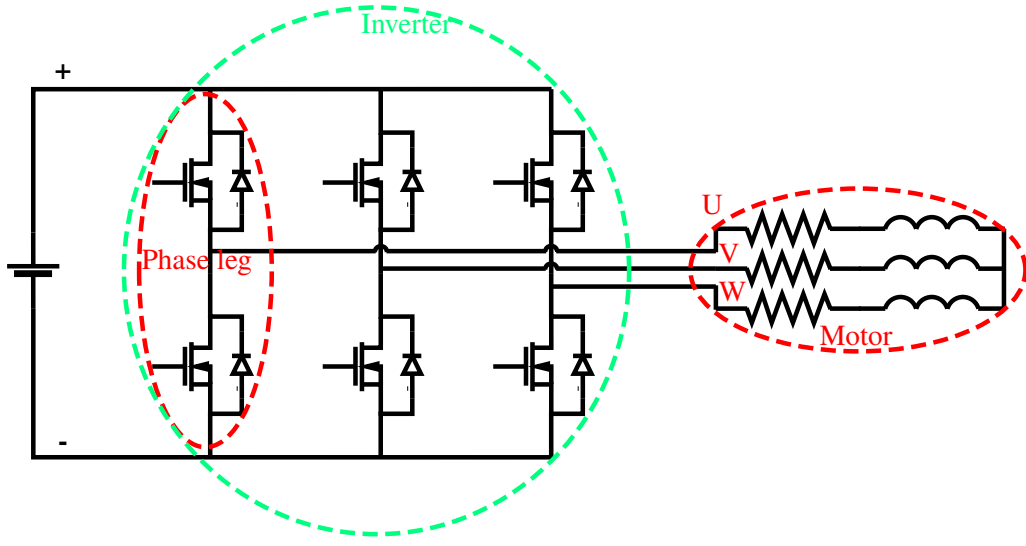


Figure 2.3: Schematic of the inverter setup (The transistors are sketched as N-channel MOSFET's).

The state of the two transistors in each phase leg are inverted, i.e. if one is open the other is closed and vice versa. Therefore each phase leg only needs one input signal to control two transistors (the other is the inverted signal). However this imposes a problem as the transistors are not ideal (infinitely fast switching). If both transistors in one leg are open at any time this will cause a short-circuit (shoot-through) of the DC link voltage. To avoid this during transitions from one state to another a dead-time (or blanking time) is introduced using either a logic circuit or a gate-driver with this feature. The dead-time is a time period inserted in each transition, this allows the transistor that was conducting to open before the other transistor begins to conduct. The duration of the dead-time should be designed to fit the application, and the management of the dead-time should preferably be hardware integrated so that no programming error can cause malfunctions.

### 2.3.1 Power MOSFETs

The main component of an inverter is the transistor, typically a power MOSFET, which acts as a switch connecting two voltage potentials and thereby letting current flow through it. Turning a MOSFET on is done by supplying the gate with a charge, which makes the MOSFET conduct current.

To select a MOSFET for the inverter, some of the characteristics of a transistor are to be examined, mainly the losses in a transistor is important. If the transistor is operated correctly and without excessive currents, the main cause of malfunction is normally heat generated by the power loss in the transistor.

The transistor should be able to conduct the current needed to drive the motor, i.e. 189[A] plus a safety margin. Alternatively more transistors can be coupled in parallel to distribute the current between them. This is a definite possibility with power MOSFETs as their ON resistance  $R_{DS}$  increases with increasing temperature [13], ensuring an even distribution of the current. The MOSFET should also be able to

## 2.3 Inverter Design

---

withstand the voltage difference from source to drain, i.e. at least half the DC link voltage 24[V]. To limit the losses in the inverter the MOSFETs should both have a low ON resistance ( $R_{DS}$ ) and be fast switching. The ON resistance is stated in the data sheet of a MOSFET. The average power loss in one MOSFET due to the ON resistance can be estimated by:

$$P_{loss-ON_1} = U_{DS-on} \cdot I_{DS} \cdot \frac{t_{on}}{T_s} = I_{DS}^2 \cdot \frac{t_{on}}{T_s} \cdot R_{DS} \quad (2.11)$$

With  $\frac{t_{on}}{T_s}$  being the duty cycle. Considering the entire inverter consisting of 6 MOSFETs, with three MOSFETs conducting at any time <sup>1</sup>, makes the loss due to ON resistance non dependent of the duty cycle. The average loss due to ON resistance in the entire inverter and at rated current for the motor can then be estimated by:

$$P_{loss-ON_{inverter}} = 3 \cdot I_{DS}^2 \cdot R_{DS} \approx 10^5 \cdot R_{DS}. \quad (2.12)$$

The approximated power loss suggests that the optimal MOSFET for this task should have a low ON resistance. Parallel coupling of more MOSFETs gives an advantage in this case as well, as the equivalent On resistance is lowered according to  $R_{eq} = 1/n \cdot R_{DS}$ , with  $n$  being the number of MOSFETs in parallel. The switching of a MOSFET also generates a power loss in the inverter, and generally the faster  $t_{c(on)}$  and  $t_{c(off)}$  time the MOSFET has, the lower the losses, where  $t_{on}$  is referring to the rise time and  $t_{off}$  the fall time. The loss in a single MOSFET due to switching is given by Equation 2.13 [14]:

$$P_{switch-loss} = \frac{1}{2} \cdot V_d \cdot I \frac{1}{T_s} \cdot (t_{c(on)} + t_{c(off)}) \quad (2.13)$$

In Figure 2.4 a switching procedure is shown, assuming the  $I_{DS}$  is constant during a switching period. The turn ON sequence based on the circuit of Figure 2-6 p. 21 in [14] is as follows:

- The control signal goes high, and the turn on delay time  $t_{d(on)}$  starts.
- Gate voltage ( $V_{GS}$ ) begins to rise, and the MOSFET starts to conduct current. The time  $t_{ri}$  is the time it takes for the driver circuit to supply the gate charge ( $Q_G$ ).
- When all of the current flows through the transistor(after  $t_{ri}$ ), the voltage drop ( $V_{DS}$ ) begin to decrease.
- When  $V_{DS}$  reaches the on voltage:  $V_{DS} = I^2 * R_{DS}$  the ON-switching is done, and the power loss is dominated by Equation 2.12.

---

<sup>1</sup>Disregarding blanking time

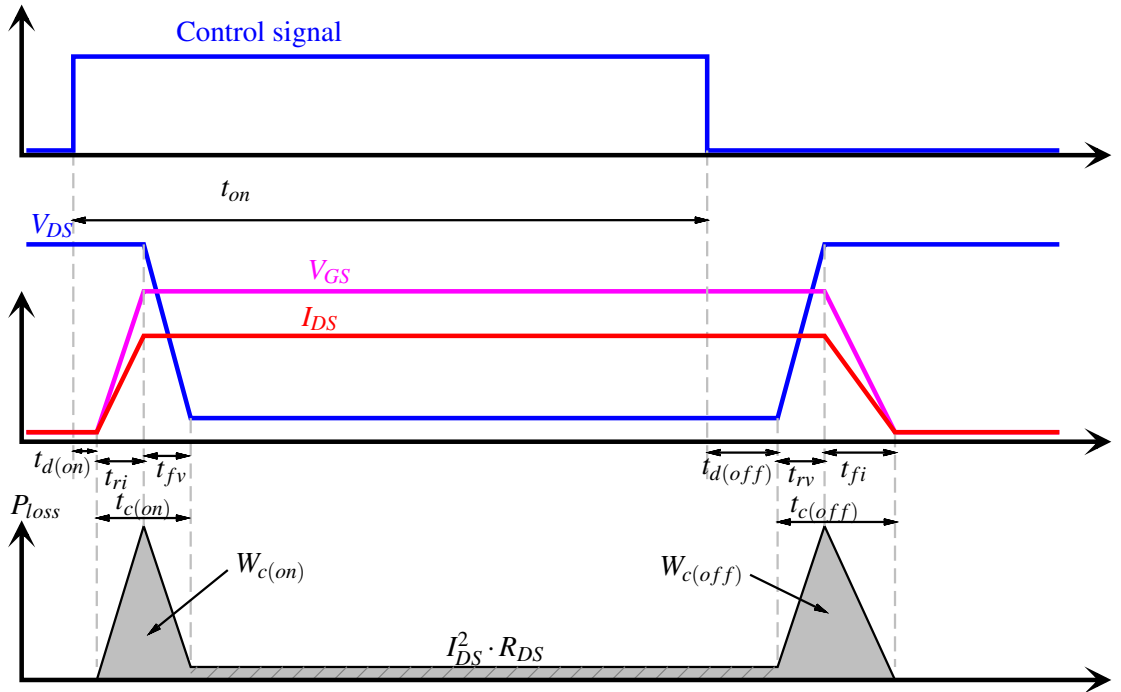


Figure 2.4: Linearized switching pattern of a MOSFETtransistor. [14]

Most of the values used to calculate the losses can be extracted from the data sheet of a MOSFET. For the inverter to be designed for the go-cart a MOSFET from *International Rectifier*, IRFP4368PbF [15] is chosen for further investigation. The main specification for the transistor can be seen in tabel 2.3.

Continuous Drain current	$I_D$	195[A]
Drain-to-Source breakdown voltage(min)	$V_{(BR)DSS}$	75[V]
Drain-to-Source On-resistance(max)	$R_{DS(on)}$	1.85[mΩ]
Total gate charge	$Q_g$	380[nC]
Turn-On delay time	$t_{d(on)}$	43[nS]
Rise time	$t_r$	220[nS]
Fall time	$t_f$	260[nS]

Table 2.3: IRFP4368PbF MOSFET transistor specifications.

To drive the MOSFETs a driver circuit is necessary and generally the driver circuit is a gate driver. The purpose of the gate driver is to amplify the power of the input signal in order to deliver the gate charge ( $Q_G$  capacity). Succeedingly, this component will be considered.

### 2.3.2 Gate driver

There are a large variety of different types of driver circuits, but as inverter topology calls for a driver circuit capable of driving the high side MOSFETs only integrated circuit half bridge drivers are considered for this application.

To avoid shoot through in any of the phase legs, the Gate driver also must feature blanking time capabil-

## 2.3 Inverter Design

---

ity. Preferably the blanking time should be programmable, as the actual blanking time for a given MOSFET is complicated to estimate, and because it is only an estimate it is better to measure the actual turn off time of the MOSFET at rated current [?].

The Gate driver should also have a capability of supplying the MOSFET with a large current to ensure short switching time (short  $t_{ri}$  on Figure 2.4). To deliver the gate charge ( $Q_G = 380[nC]$  needed for a  $t_{ri}$  of 220 [ns] a continuous current of  $\approx 1.73[A]$  is needed. Therefore a Gate driver is chosen, a IR21834 that is capable of delivering 1.8 [A] and has programmable blanking time.

To assist the chosen Gate driver in supplying the gate charge, a bootstrap capacitor can be implemented. The bootstrap capacitor is coupled as shown in Figure 2.5 and works as follow: When the high side MOSFET is off, and the low side is conducting, the high side bootstrap capacitor is connected to ground and to  $V_{cc}$ , through the forward biased diode, and hereby gets charged. When the Gate driver switches state, the bootstrap capacitors charge is sent into the MOSFET.

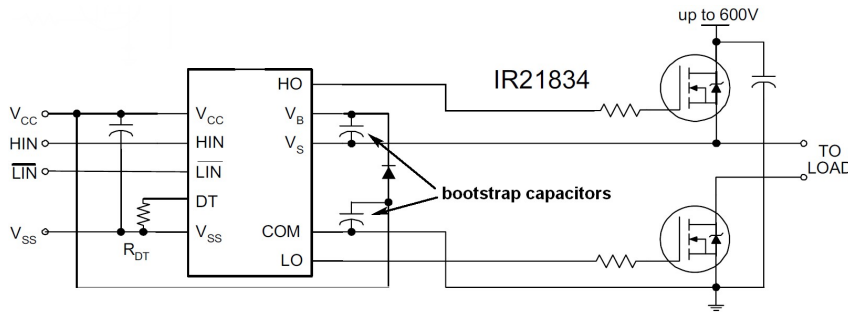


Figure 2.5: Typical connection scheme for IR21834 and two MOSFETs including two bootstrap capacitors. [16]

There are two things to be aware of on a circuit illustrated on the figure. First, the capacitance of the bootstrap capacitors and the values of the other components should be calculated in accordance with application notes from the manufacturer[17]. Second, the distance between the two nodes of respectively the source of the MOSFET and the Gate Driver source measurement node should be kept at a minimum. Having it too long may cause stray inductance, which can lead to undesired oscillations due to slowed down turn-offs. This is illustrated in figure 2.6.

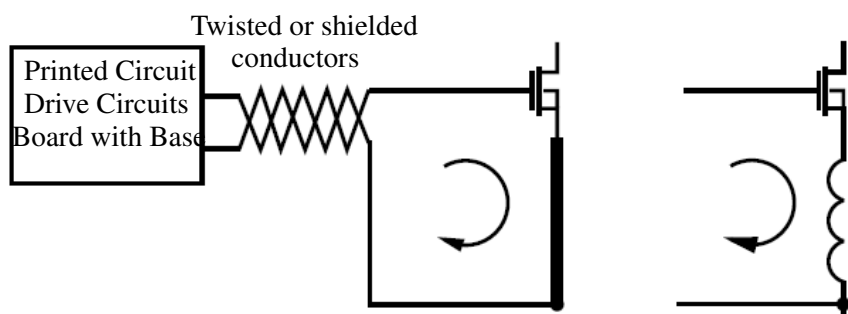


Figure 2.6: Minimizing stray inductance

When the gate driver operates the MOSFETs, the print circuit board should be able withstand the nominal current  $I_{rated}$  for the motor and how this will be achieved is considered next.

### 2.3.3 PCB conductor width dimensioning

High peak currents are expected when the system is excited intensely. Due to the high peak currents, it is important that the tracks on the printed circuit board are dimensioned according to that. Similar to the calculations on the cables connecting the motor and the batteries, see section 2.2.2, the calculations are based on the square area of the conductor. The necessary track width  $W_{track}$  is calculated using equation 2.14, that are based on general guidelines for PCB layout [18],[19].

$$A_{track}[\text{mils}^2] = \left( \frac{I_{track}[\text{A}]}{0.048 \cdot T_{rice}[\text{ }^{\circ}\text{C}]^{0.44}} \right)^{\frac{1}{0.725}}$$

$$W_{track}[\text{mm}] = \frac{A_{track}[\text{mils}^2] \cdot (0.0254^2)}{H_{track}[\text{mm}]} \quad (2.14)$$

With the height of the copper tracks set to be  $H_{track} = 0.1[\text{mm}]$  and the allowed temperature rise of the conductor to be  $T_{rice} = 20[\text{ }^{\circ}\text{C}]$  at a maximum current of  $I_{track} = 200[\text{A}]$ , calculating the track width using equation 2.14 reveals a minimum width of  $W = 103[\text{mm}]$ .

Figure 2.7 illustrates the recommended relationship between the current flow and the PCB track width, based on formula 2.14 at two different temperature rises,  $T_{rice} = 20[\text{ }^{\circ}\text{C}]$  and  $T_{rice} = 50[\text{ }^{\circ}\text{C}]$ . The copper track thickness is again set to be  $Tr_{thick} = 0.1[\text{mm}]$ .

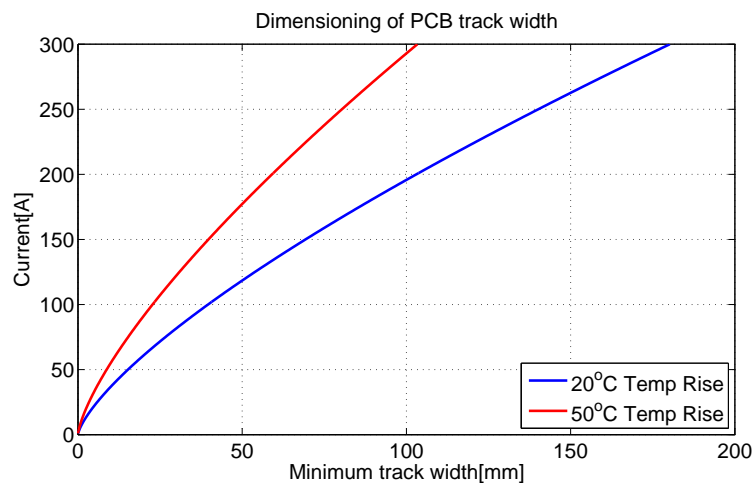


Figure 2.7: Copper track thickness at two different allowed temperature rises.

Another approach to calculate the required cross-sectional area of the conductor, is to follow the guidelines for cable dimensioning, [12] as was used in section 2.2.2. If the conductive area is chosen to be  $25[\text{mm}^2]$  as was the minimum cable area, the PCB track width at  $0.1[\text{mm}]$  thickness calculates to:

$$W_{track}[\text{mm}] = \frac{25[\text{mm}^2]}{0.1[\text{mm}]} = 250[\text{mm}] \quad (2.15)$$

## 2.3 Inverter Design

---

It is concluded that a standard PCB is not usable. Even if a temperature build up, and thereby additional power loss in the inverter, is accepted. The circuit tracks would simply be difficult to design due to the large width required. An obvious solution would be to design the PCB with thicker copper tracks. A standard PCB could be modified by plating the copper surface with a layer of solder to the desired thickness.

Another design approach is to fabricate the necessary high current tracks in plates of aluminum. They are available in various sizes, where for example a thickness of 2[mm] would minimize the problem of wide tracks with a factor of 20 (not accounting for the difference in conductivity of aluminum and copper). Multiple conductive layers can be built using isolating material between the layers of aluminum. It is therefore concluded that the design of the inverter should include a mix of traditional PCB layout for the driver control circuits combined with a customized high-current circuit for the driver MOSFET's.

### 2.3.4 Optocoupler

To connect the DSP with the BPI an optocoupler interface is considered. An optocoupler is used to provide galvanic isolation to a signal between two circuits. The input and the output of the optocoupler is only connected by a beam of light. Galvanic isolation is desirable between a microprocessor circuit that are sensitive to electric noise, and power electronics generating switching pulses and high current spikes, which can be expected in the inverter circuit.

A optocoupler often contains of a housing with an internal LED emitting light, received by an internal photo transistor. To obtain further distance between the control electronics and the power electronics, an optocoupler using two separate housings for the emitter and receiver side can be used, see figure 2.8. The connection between the two is then made up by an optical fiber cable of the length required.

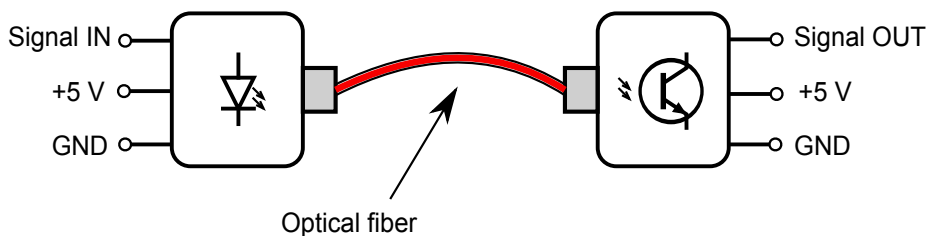


Figure 2.8: Using optocouplers for galvanic isolation of control signals.

### 2.3.5 Sauer-Danfoss inverter that meets the requirements

Initially the aim have been to build a custom designed inverter. However it is decided to use an available working inverter that fits the requirements, due to time constraints in the project. The selected inverter is a *Sauer Danfoss BPI 5435*, capable of running the selected motor. The BPI has been fitted with a custom made BPI-interface, see appendix .1.1, produced by another project group [20]. The interface board consists of a FPGA programmed to control the switches securely, and with a programmable dead-time, see appendix .1.1.1.

It is therefore possible to move on to the system modeling, with the aim of controlling the BPI to drive the go-cart. Both the motor model and the go-cart model will be derived in the following section.

## 2.4 Digital Signal Processor

The go-cart is to be driven by a three phase AC-motor, powered by batteries supplying a DC-source. Therefore power electronics are used to drive the motor. The power electronics needs to be controlled and for the sake of implementing different control strategies a Digital Signal Processor (DSP) is used.

The major purpose of the DSP is to measure the currents and the rotational speed of the motor, compare the output with a reference signal, and convert this into an output for the inverter. This should be done according to which ever control strategy is chosen. The reference input is a voltage signal from a potentiometer connected to the gas pedal. A *Texas Instrument TMS320 C2000 Series* DSP is chosen for the purpose.

A DSP is a microprocessor designed for high performance tasks. A Digital Signal Controller (DSC) is a DSP with peripheral circuits included in the chip, such as Pulse Width Modulation (PWM), Analog to Digital Conversion (ADC), watchdog timers etc.. The DSC is usually used in connection with real time data acquisition and processing that often requires fast operation, thus low latency. The latency of a system refers to the experienced time delay to execute a given instruction. In order to achieve low latency, the architecture of the chip is optimized and the instruction set reduced when comparing with a microprocessor used in a personal computer (PC). This optimized architecture includes implementation of hardware accelerated mathematical operations, namely multiplication units, binary shifting units and floating point units. When calculating decimal numbers a floating point DSP is approximately 12.5 times faster than a fixed point DSP [21]. The DSC is mainly applied in embedded solutions that often requires low power, small physical dimensions, low latency and a number of peripherals. From this point on the microprocessor will be referred to as the DSP. The chosen unit is a DSP with the production name *Texas Instrument TMS320 C2000 Series* that uses a 32 bit line and runs at 150[MHz]. An overview of the task for the DSP is illustrated in figure 2.9.



Figure 2.9: A block diagram that shows an overview of the general structure of a Digital Signal Processor (DSP)

The main task of the DSP is to sample analog and digital signals to use in the further calculations as defined in the embedded software. The result of the calculations are then used to output control signals for the application that requires to be controlled. It requires configuration of parallel interrupts at specified intervals that avoids conflicting behavior. When an interrupt occurs, the current operation of the DSP is stopped until a subprocess has executed. After the execution of the subprocess the DSP returns to the previous operation before the interrupt. In other words, the interrupt is a way to run a different code when an event occurs, for instance in connection with sampling of data at specific intervals or in connection with calculating the PWM signal at certain instants. Two interrupts are used in the application; one for sampling at a specific interval and one for updating the PWM register. See an illustration of this logic in figure 2.10

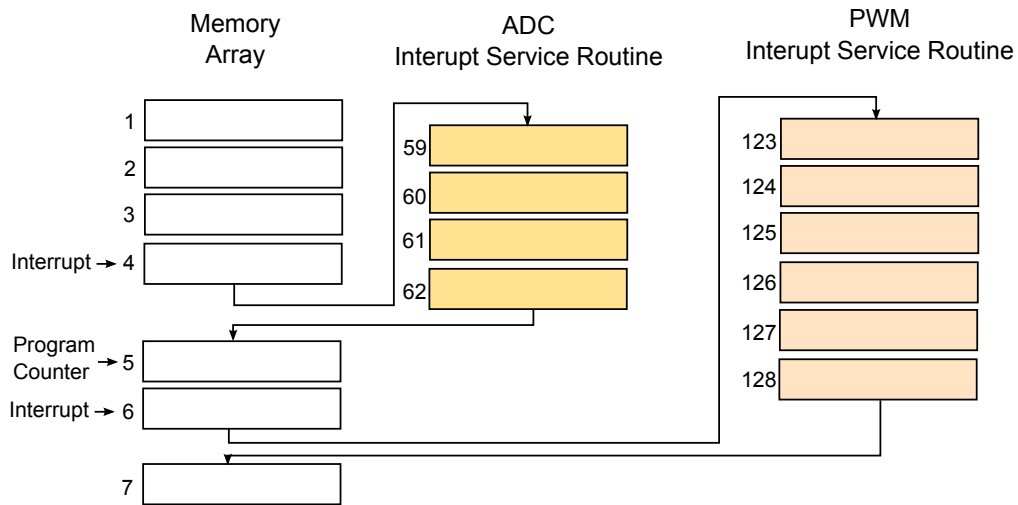


Figure 2.10: An illustration of an interrupt-routine executed in the DSP

The program counter (PC) is counting upwards with one digit for every clock cycle, and the instruction from the matching memory cell is executed. In this example, at the PC count from 4 to 5 an ADC interrupt occurs, which means the memory cell 59 – 62 is looped through before returning to the main loop, i.e. memory cell 5. This basic example shows an overview of how the software is setup in the application. A more specific introduction to the code is given next.

#### 2.4.1 Software Structure

Initially the software was created, so whenever the DSP received an interrupt from the ADC it calculated the next output and placed this in a global variable that the PWM interrupt then could read from and set the PWM registers accordingly. The problem with this strategy is that the code for the calculations also happens in the interrupts. This means that a lot of time is spent in the interrupt, and thus a lower priority can be neglected for the run-time of the interrupt service routine.

To overcome this problem it is decided to use the Model-View-Controller(MVC) pattern for structuring the software, however with a slight modification. Figure 2.11 shows the general structure of MVC.

The Model contains all important informations regarding the application, e.g. measured current values and calculated fluxes. The Model in this application is simply represented by a struct.

The View is used to display the information for the user. A secondary micro controller has been implemented to act as the View, thus freeing up the DSP for its main responsibility to control the go-cart motor. This means the View does not access the actual Model, however, the user only needs a rough estimate of the data stored in the model.

The functionality of the Controller is to process the informations it receives from the interrupts and then act upon these, including updating the Model (and the View - normally). It is in the Controller that all the calculations are made. The interrupts now only updates the Model. In bigger applications the interrupts

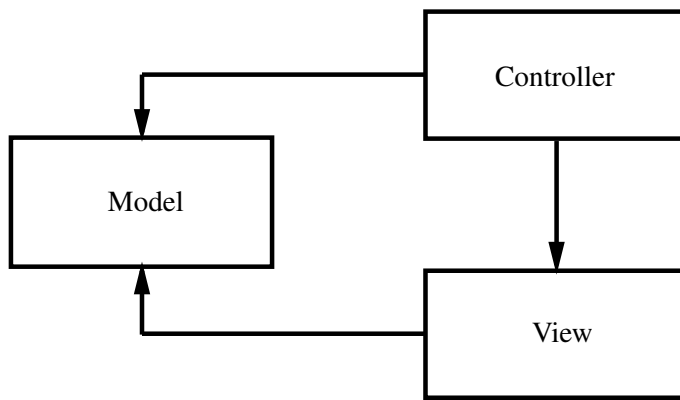


Figure 2.11: The Model-View-Controller pattern

would not directly access the Model, but instead simply inform the Control. However as this application is fairly small, and the Model basically consists of this information, this is deemed acceptable.

Instead of using the ADC to define the sampling time, a timer is set up to generate an interrupt which does not run the Controller code itself, but merely allows it to be run. It is here of importance that the run-time of the code does not exceed the time in between the interrupts. Below is seen a pseudo code for the program run on the DSP.

```

int runcontroller = 0;

void main(void) {
    initDSP();
    // Start the infinite loop
    while(1) {
        if(runcontroller == 1){
            Controller();
            runcontroller = 0
        }
    }
}

void Controller (void)// Run state for every sample
{
    Time_Update(); // Update time variable
    ADC_load(); // Load inputs from the ADC
    Current_calc(); // Calculate currents at each sample
    Omega_calc(); // Calculate omega
    Controller_calc(); // Calculate controller output values
    PWM_calc(); // Apply PWM modulation
    PWM_Update();
}
  
```

```
}
```

```
interrupt void timer0_isr(void)
{
    runcontroller = 1
    TIMER0ACK=1 //acknowledge interrupt, so next interrupt can be generated
}
```

The performance of this structure is optimal in the sense that all the calculations are made outside the interrupt routines. This means that the calculations are carried out before hand and then used when an interrupt occurs. Further analysis is carried out in order to detect boost the performance of the DSP.

### 2.4.2 Software performance optimization

First of all, the DSP is a floating point unit which means that floating point operations are carried out on hardware level. A floating point unit saves a number using the following representation:

$$x = s \cdot b^e \quad (2.16)$$

Where  $x$  is a real value number,  $s$  is the significant digits,  $b$  is the base and  $e$  the exponent. The idea behind this representation is to store all significant digits within in the number that needs to be represented and then place the decimal point where ever it has to be. The precision of the number is restricted by the available memory. The floating point units comes with a number of simple mathematical operations such as addition, subtraction, multiplication, division etc.. If some operations are not included on hardware level, they are usually included as a library written in assembly code or a higher level programming language for specific operations. These mathematical operations are then performed using the available simple hardware operations. This is also what happens in fixed-point unit DSPs, the only difference is that all floating point operations are carried out using libraries that translates floating point operations into fixed point and then back again.

Texas Instrument has both fixed-point and floating-point unit DSPs in their assortment. Therefore, they have written a library called *IQmath* that can perform floating point operations in a fixed point unit. Using these libraries the compiled machine code will be optimized for the TI DSPs. Using this library gives a performance boost compared to using the standard *c math library*. By changing one line of code in the IQmath header file the written code can also be used in a floating point unit DSP making the code scalable between different DSPs.

Another more relevant library for the C2000 TMS320 DSP is called *Floating Point Unit Fast Run- Time Support* (fastRTS). This library contains highly optimized floating point math operations that reduces the execution time considerably for a given math operation. The resolution of the library is 32 bit thus giving access to floating point and double operations. In the DSP both *long* and *float* data types are defined as 32 bit. This library uses a *Newton-Raphson* algorithm to perform division, and lookup tables to optimize the following mathematical operations: *sin*, *cos*, *atan*, *atan2*, *isqrt*, *sqrt* and *sincos*. Using this library in the code, the time for the controller to perform its operations are calculated to be  $\approx 1750$  pulses on a  $150[\text{MHz}]$  DSP. This means that the main software can potentially be operated at a speed of  $85.7[\text{kH}\zeta]$ . Using the standard RTS library the number of pulses to execute the code increases to  $\approx 2400$  thus reducing the maximum operation speed to  $62.5[\text{kH}\zeta]$ . In our application the speed of the code is

increased by 36.8% just by including the fastRTS library. Generally, the sampling frequency is defined by the bandwidth of the system. A rule of thumb says that this should at least be 20 times this. However, since the system is only excited by a 50[Hz] signal the sampling frequency should not go under 1[kHz]. Hence, the standard library is plentiful to operate the go-cart .

### 2.4.3 Analog to digital conversion

The analog to digital converter (ADC) converts an analog signal into a digital signal, as the name reveals. This conversion happens at intervals that can be changed for each ADC. The ADC converter within the DSP has a 12-bit resolution, and the input voltage measurement range is specified to be between 0[V] to 3[V]. This gives a resolution and quantization error of the size calculated in 2.17.

$$R = 2^{12} = 4096[\text{digit}]$$

$$Q = \frac{3[\text{V}]}{2^{12}[\text{digit}]} = 7.3 \cdot 10^{-4}[\text{V}/\text{digit}] \quad (2.17)$$

This means that the voltage range 0 to 3[V] is divided into 4096 levels, and at each level the voltage jumps by  $7.3 \cdot 10^{-4}[\text{V}]$ . The quantization error is not the only signal of error in the conversion, also noise and jitter from the crystal can directly cause wrong conversions. Another source of error in ADC conversions is not related to the amplitude of the converter signal but rather the frequency of conversion (sampling rate). In between each sample the value of the signal is not known for the DSP. If the signal is slowly varying it could be interpolated, but if the signal is rapidly changing the interpolation can come shortfull and this behavior is known as aliasing. The principle of aliasing is illustrated in figure 2.12.

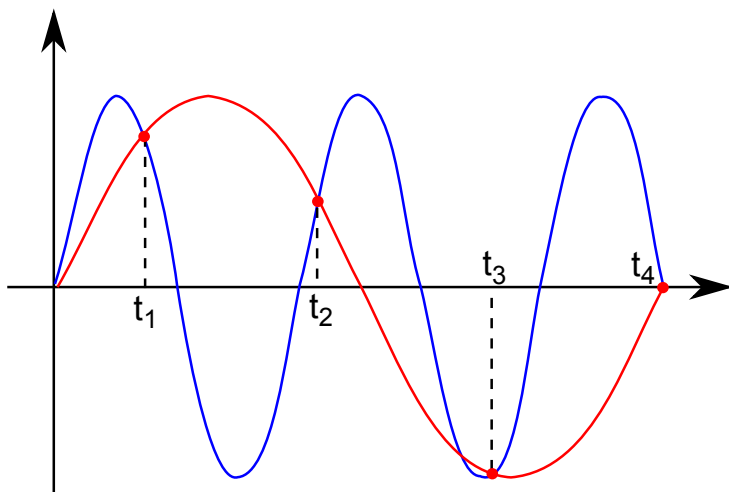


Figure 2.12: An illustration of the principle of aliasing in signal reconstruction.  $t_1, t_2, t_3$  and  $t_4$  is the sampling times. A high frequency signal sampled at the given time instants mimics a low frequency signal.

If the sampling frequency is lower than twice the highest frequency of the analog signal, which is called the *Nyquist rate*, this problem may occur. In order to avoid this problem Harry Nyquist stated that the sampling frequency must be larger than the Nyquist rate in order to digitally reconstruct the analog signal.

The analog signal is converted using a sample-and-hold circuit. This circuit is necessary since the conversion can not happen instantaneously. In this circuit a capacitor is charged to hold the current voltage level, then a switch disconnects the capacitor so the conversion can happen by measuring up against a constant time invariant value. In fact, the DSP has two sample-and-hold circuits within its ADC module. Even though only one 12-bit ADC is available, it is possible to convert two channels simultaneously. This, obviously, increases the latency of the ADC module since two AD conversions has to happen before a the sample-and-hold circuit takes in new values.

The ADC is used to convert analog signals from current transducers, which are measuring the current in the three phases of the AC-motor.

The sampled data is saved in two different locations in 16 bit registers in the memory of the DSP. That is in the *AdcRegs* and *AdcMirror* registers. The *AdcRegs* register contains two 2-bit wait states in the lower bits, which means the data is saved in the upper bits. The *AdcMirror* register only has the 12-bit data placed in the lower bits. According to the data sheet, this mirrored ADC register is the recommended register to use in high speed continuous applications, since the delay caused by the wait state in order to access the memory is not present.

### 2.4.4 General Purpose Input/Output ports

General Purpose Input/Output ports are a common part of a DSP. Depending on the purpose of the application, the ports can be configured through specific registers to run as either an input port or an output port. Notice, these ports are digital ports and therefore only accept high or low values. A high value for the *TI C2000* is  $3[V]$  and a low value is  $0[V]$ . A signal from a encoder, used to measure the rotational speed of a motor, is read through a digital input port, while a PWM signal to an inverter is generated through the digital output ports. The theory behind encoder (put it here)

### 2.4.5 PWM module

The PWM module in the DSP is called Enhanced Pulse Width Modulation (ePWM) and it comes with a highly optimized and automated hardware solution that requires minimal CPU usage and minimal software intervention once the module is setup to run. This means that the hardware between the two PWM units on the DSP are not shared, but instead build by separate hardware resources. The PWM module can be used for a wide range of applications, such as motor control, control for switch mode power supplies, or used for Uninterruptible Power Supplies (UPS). The way the PWM module works is quiet simple. A counter *CNT* is counting from 0 to a predefined value *PR*. Once the counter value is equal to a value in a predefined compare register *CMP* the output port is logical high. This procedure can be implemented with an up-counter (sawtooth wave), a down-counter (inverse sawtooth wave) or an up-down-counter (triangle wave). On figure 2.13(left) the up-down counter is illustrated and on figure 2.13(right) the up-counter is present.

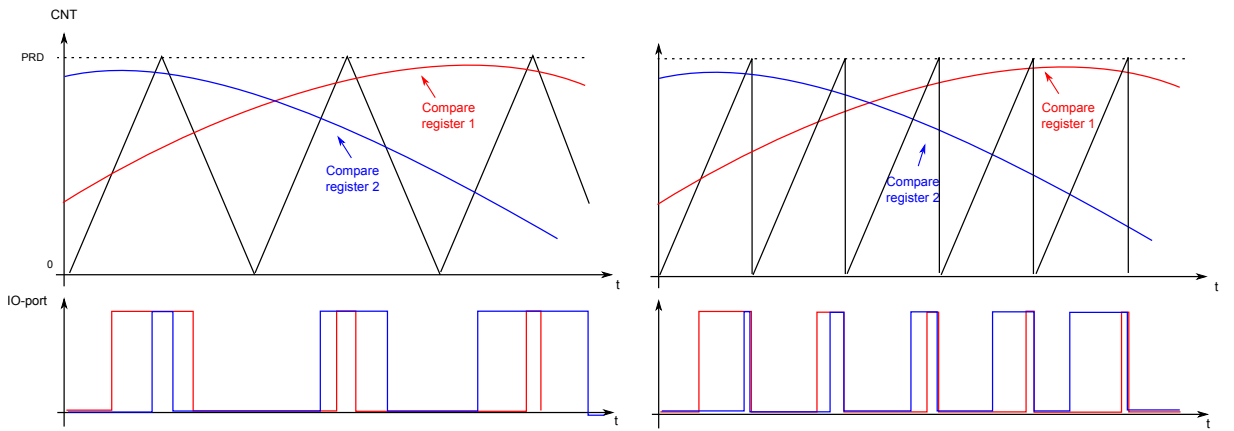


Figure 2.13: Different counter methods for PWM signal generation

At the top part of the figure the counter is continuously counting in the specified method (up, down or up-down) resulting in a pulse between the intersections as illustrated at the bottom part. The difference between the two PWM-modulation methods lies in the pulses. As evident from the figures, for a sawtooth wave the falling-edge happens at the same time instant moving the pulses to the end of the period. Similarly, the inverse sawtooth wave has its rising edge on same time instant thus moving the pulses towards the beginning of the period. At a triangle wave method the pulses will be located at the center of the period.

The PWM module comes with a lot of build in features one of them is a dead-band generator. This feature is useful for inverter control application because it gives access to avoid potential risk for short circuit (at falling and rising edge) between the upper and lower transistor. When the PWM module generates a pulse, an inverted pulse is also generated. The actual PWM signal could for instance be connected to the upper transistor and the inverted signal to the lower. Since the rising and falling edges between the actual and the inverse pulse can be programmed individually, this will give total control over dead-time implementation. The only downside with this DSP build in dead-band generator is that in case of DSP failure, it is difficult to predict the state of the dead-band generator. Therefore an external dead-band generator on hardware level is preferable.

## 2.5 Induction motor model

The following sections describes the modeling of an induction motor. The induction motor consists of a squirrel-cage rotor surrounded by three field coils with equal resistance, which are connected in a star-connection. Two models needs to be derived, consequently steady state model to estimate the performance of the motor and a dynamic model to predict the motors transient behavior. The steady state model of the induction motor, which is described in 2.5.2, consist of a single phase equivalent circuit modeling in order to calculate the total current flow in the motor. The dynamic model of the induction motor consists of transforming the three field coils into an equivalent model using two field coils arranged in a quadrature, using an  $\alpha\beta$ -transformation described in 2.5.4.1. Additionally, a rotating reference frame is introduced called a dq-transformation. The benefit of using this reference frame, described in 2.5.4.2, is the fact that rotating space vectors will appear constant in the given reference frame which gives access to apply closed loop control.

### 2.5.1 Basics of an induction motor

An induction motor basically consists of 2 parts, a stator and a rotor. The stator consists of metal sheets in which the coils are wound onto. The amount of parts the coils are divided into, decides the number of poles. The purpose of the stator is to generate a rotating magnetic field. The angular velocity of the magnetic field depends on the input frequency and the number of poles. As mentioned in 2.1 the rotor of the used motor is constructed as a squirrel-cage, see figure 2.14.

When the magnetic field rotates, the rotor bars are cut by the rotating magnetic field and therefore induces a voltage in the rotor, and rotor current  $i_r$  flows in the conductor. The current in the rotor bar creates a magnetic force, which acts opposite of magnetic force of the stator, this makes the rotor rotate. The magnetic force on the rotor depends on the magnetic flux density  $B$ , the current  $i_r$ , and the length of the rotor bar  $L$ , in the magnetic field. The force can be expressed as

$$\vec{F} = \vec{i} \cdot L \times \vec{B}$$

Assuming the magnetic field  $\vec{B}$  is perpendicular to the conductor  $\vec{i} \cdot L$  the notation simplifies to:

$$F = i \cdot L \cdot B \cdot \sin(\theta) = B \cdot i \cdot L$$

where  $\theta$  is the angle between the magnetic field and the conductor. How the magnetic field and the forces act upon each other can be seen in figure 2.14.

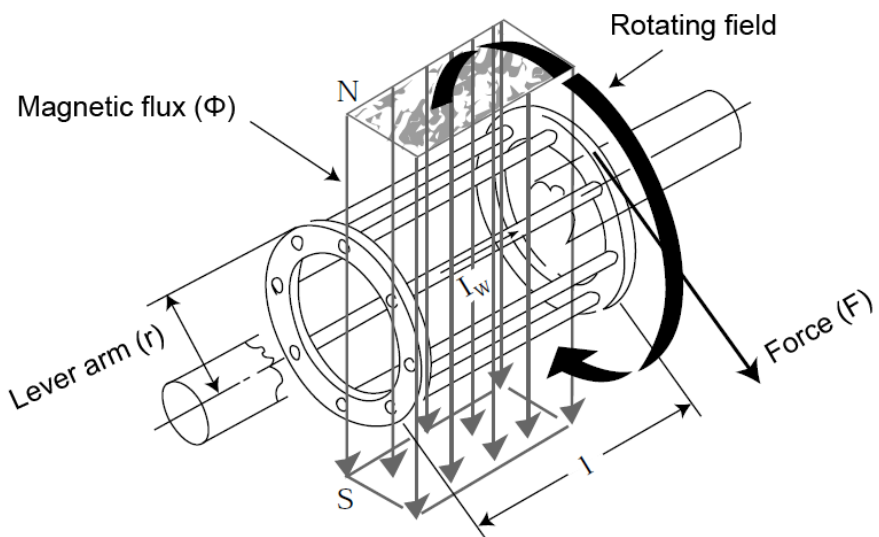


Figure 2.14: Rotating field and the squirrel-cage rotor[22]

The angular velocity of the rotor will not reach the angular velocity of the magnetic field for any load. If the two angular velocities were the same, rotor bars would not be moving through the magnetic field,

thus no currents would be induced in the rotor bars. This difference in angular velocities is known as the slip. For a given slip the steady state performance of the motor can be calculated.

### 2.5.2 Steady state single phase induction motor model

The equivalent steady state diagram for a single phase can be drawn as in figure 2.15 using an ideal transformer to model the back-emf for the stator  $E_s$  and the rotor  $E_r$ . The polarity of the back-emfs is marked using the dot convention.

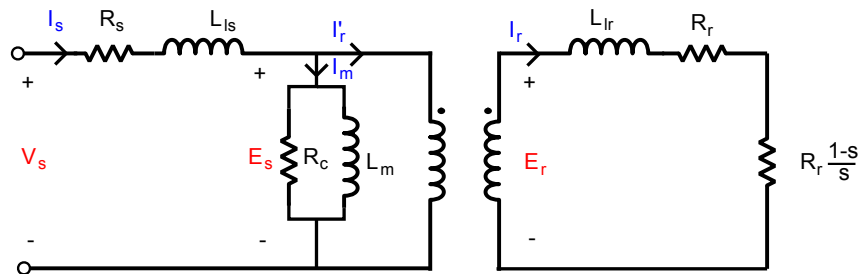


Figure 2.15: Equivalent steady state diagram of one phase

There is an  $R_c$  resistor in this circuit modeling the magnetic core losses as a result of hysteresis and eddy currents. Hysteresis losses is associated with the change of the magnetization of the core material and eddy current losses is a current that tries to work opposite to the change in flux that causes the current to run in the first place. The core losses are usually neglected in the model due to high resistance values leading to the current flowing through the magnetization inductance and transformer.

The stator circuit and the rotor circuit is coupled through an ideal transformer. Transforming the rotor side through the ideal transformer to the stator side and also turns ratio transforming the components gives a less complex equivalent circuit as seen in figure 2.16.

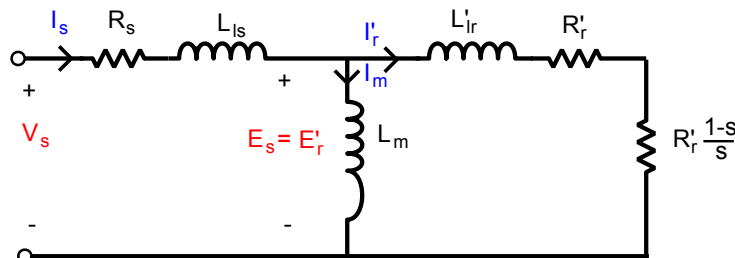


Figure 2.16: Equivalent stator side transformed steady state diagram of one phase with turns ratio transformed parameters

It is important to note that also the currents in the rotor are turns ratio transformed, which is illustrated by the apostrophe notation. This means that the calculated current  $i'_r$  is not the actual current flowing in the rotor windings. Since it is standard practice to set up the transformed steady state circuit, the apostrophe notation is left out for the remaining part of the report. Using the circuit in figure 2.16 the following single phase model can be set up in the Laplace domain.

$$U_s = I_s \cdot (R_s + j\omega_e \cdot L_{ls}) + I_s \cdot \frac{(j\omega_e \cdot L_m) \cdot (j\omega_e \cdot L_{lr} + \frac{R_r}{s})}{j\omega_e \cdot (L_{lr} + L_m) + \frac{R_r}{s}} \quad (2.18)$$

Rearranging the terms in order to obtain a transfer function describing the steady state dynamics from voltage to current:

$$\frac{I_s}{U_s} = \frac{1}{(R_s + s \cdot L_{ls}) + \frac{(s \cdot L_m) \cdot (s \cdot L_{lr} + \frac{R_r}{s_l})}{s \cdot (L_{lr} + L_m) + \frac{R_r}{s_l}}} \quad (2.19)$$

Inserting the parameters obtained in 2.7 the poles and zeros for the steady state system can be obtained.

$$\frac{I_s}{U_s} = \frac{37.80e3 \cdot (s + 0.581)}{(s + 835.5)(s + 0.05533)} = \frac{3.44e - 2s + 0.02}{9.11e - 7 \cdot s^2 + 7.61e - 4 \cdot s + 4.21e - 5} \quad (2.20)$$

The poles of the steady state system are in the left half plane, which means the system is stable and a bode plot can be used to obtain useful parameters (phase and gain margins), see figure 2.17. Further, if desired the eigen frequency and the damping coefficient for the motor can be calculated if desired. These showed to be:

$$\begin{aligned} \zeta &= 0.059 \quad [.] \\ \omega_n &= 4.21e - 5 \quad [rad/s] \end{aligned}$$

Not only is the damping coefficient  $\zeta$  very low which can give rise to oscillations, but also one of the open loop poles of the system is near the imaginary axis making the system very slow. Even though this is a steady state model, it describes the transient behavior of the motor for constant slip. Since, this is hard to realize in practice a dynamic model is necessary to derive, which will be done in section 2.5.4. However, the steady state model can, on the other, be used to estimate the performance of the motor using the torque equations.

### 2.5.3 Steady-state torque equation

The torque equation for the induction motor can be derived using the model in figure 2.16. This model represents the mechanical output power as the outermost resistor. This resistor models the real mechanical power transfer which is given in 2.21 as a function of the rotor current  $I_r$ , slip  $s$  and the rotor winding resistance  $R_r$ .

$$P_{mech} = m \cdot R_r \frac{1-s}{s} \cdot I_r^2 \quad (2.21)$$

The torque produced by the motor is a function of the power and the speed of the motor, both electrical

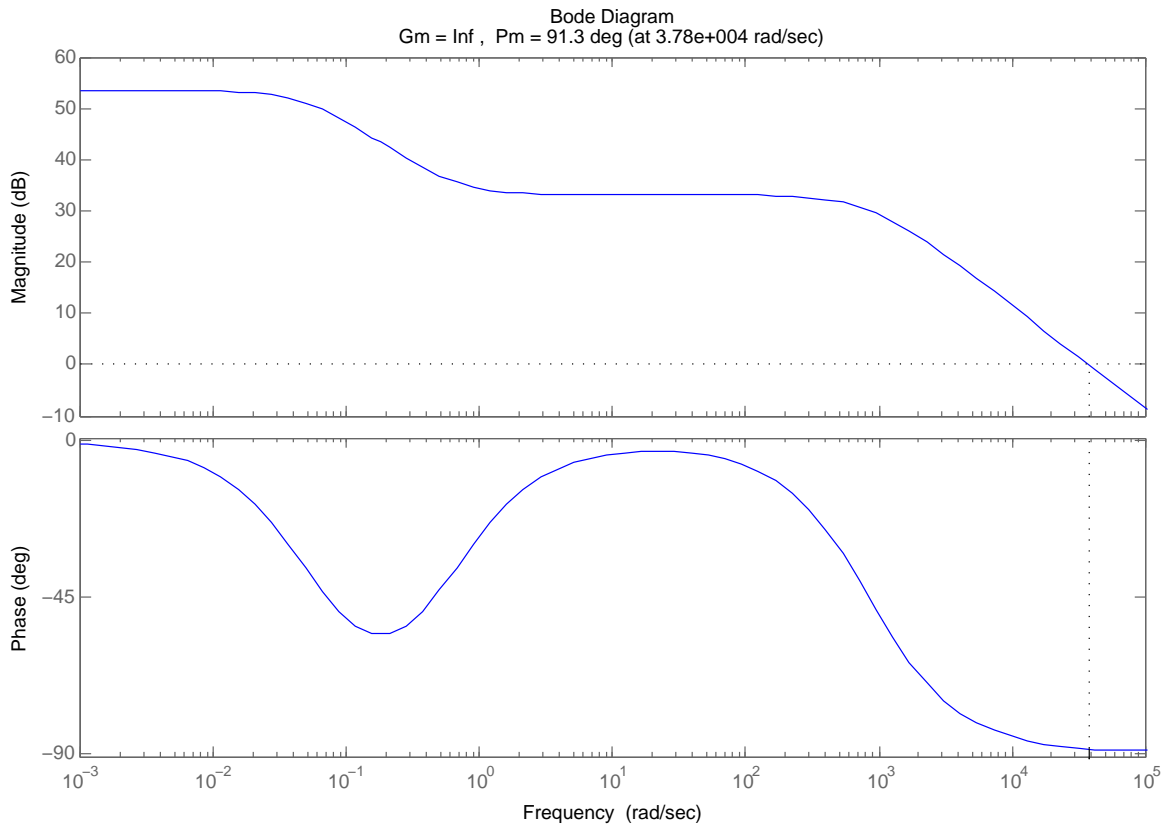


Figure 2.17: Bode plot of the steady state motor model

and mechanical speed.

$$\tau = \frac{P_{mech}}{\Omega_r} = \frac{P_{mech}}{(1-s) \cdot \Omega_s} = \frac{p_b \cdot P_{mech}}{(1-s) \cdot \omega_s} \quad (2.22)$$

Inserting equation 2.21 in 2.22 gives.

$$\tau = \frac{p_b \cdot m \cdot R_r \cdot I_r^2}{s \cdot \omega_s} = \frac{p_b \cdot m \cdot R_r \cdot I_r^2}{\omega_{sl}} \quad (2.23)$$

In order to obtain the torque characteristic, the rotor current has to be derived. Since the input voltage is known  $U_s$  Thevenin's Theorem is applied to obtain a single loop describing the rotor current flow  $I_r$ , see figure 2.18.

## 2.5 Induction motor model

---

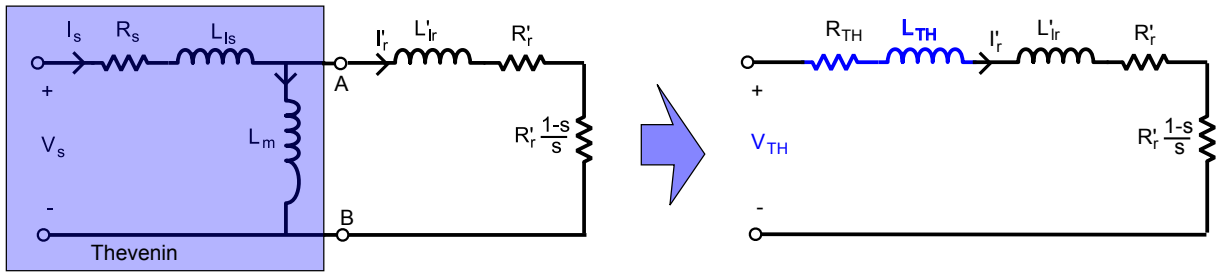


Figure 2.18: Thevenin equivalent circuit for calculating the rotor current  $I_r$

After deriving the thevenin terms and manipulating the equation the following expression is obtained for the rotor current:

$$I_r = \frac{V_{th}}{\sqrt{(R_{th} + \frac{R_r}{s})^2 + (\omega \cdot L_{th} + \omega \cdot L_{lr})^2}} \quad (2.24)$$

Using the rated parameters from table 2.1 for the motor and the calculated rotor current in 2.24 gives the torque response for steady state input shown in figure 2.19.

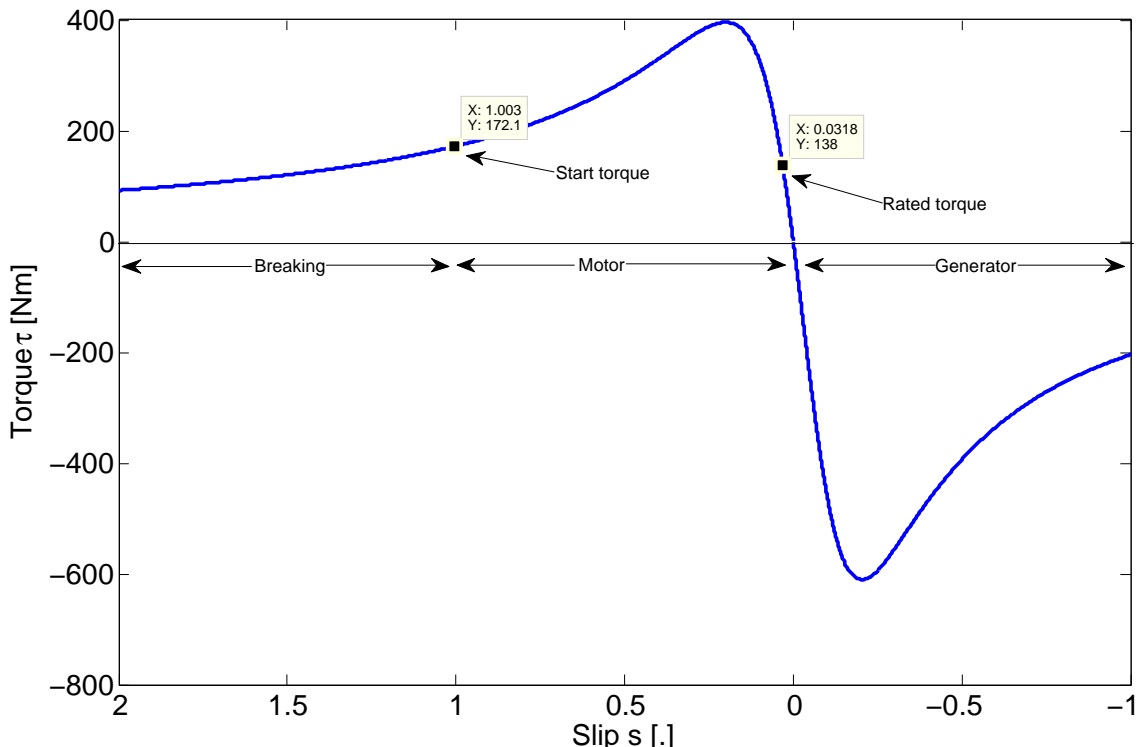


Figure 2.19: The torque slip characteristic for the Sauer-Danfoss AC-motor with model number: TSA170-210-038.

The figure is divided in generator, motor and braking intervals. For negative slip the induction machine

is running as a generator, for positive slip the machine is running as a motor and for  $s>2$  the machine is braking. Additionally, it is seen in the figure that the motor is capable of pulling a load of up to 172[Nm] from stand still ( $s=1$ ). According to the calculations the rated torque is 138[Nm] at rated slip, which is notable more than the nominal torque obtained from the nameplate:

$$\tau_{rated} = \frac{P_{rated}}{\omega_m} = 30.03[Nm] \quad (2.25)$$

$$s_{rated} = \frac{\omega_e - \omega_r}{\omega_e} = 0.0316[.] \quad (2.26)$$

Of course the rated input power  $P_{rated}$  is not entirely being converted to mechanical power, but the significant difference between the calculated and the given value indicates wrong parameters. The data indicates that the motor should be capable of driving the go-cart even from standstill without a controller. This is, however, not a feasible solution i.e. if speed control is desired. This can be achieved using an open loop scalar controller or a closed loop field oriented controller. Before such an initiative can be put in practice a dynamic model describing the system has to be derived.

#### 2.5.4 Dynamic induction motor model

In order to model the induction motor the following assumptions are made to simplify the model

- Space harmonics of the flux linkage distribution are neglected
- Slot harmonics and deep bar effects are not considered
- Iron losses are not taken into account
- Saturation is introduced on a macroscopic basis
- Neutral point is isolated

By making these assumptions, the three-phase windings of the induction motor can be considered as three coils separated by  $120^\circ$  in a star-connection as seen on figure 2.20(a). Furthermore it is assumed that the squirrel-cage rotor also can be viewed as coils as illustrated in figure 2.20(b).

There are some resistance in the wires and the flux from inductors are linked. Thus, it can easily be seen that the model of the induction machine is made using the following equations for the voltages and fluxes.

$$\begin{bmatrix} u_{sa} \\ u_{sb} \\ u_{sc} \end{bmatrix} = R_s \begin{bmatrix} i_{sa} \\ i_{sb} \\ i_{sc} \end{bmatrix} + \frac{d}{dt} \begin{bmatrix} \lambda_{sa} \\ \lambda_{sb} \\ \lambda_{sc} \end{bmatrix} \quad \begin{bmatrix} \lambda_{sa} \\ \lambda_{sb} \\ \lambda_{sc} \end{bmatrix} = L_s \begin{bmatrix} i_{sa} \\ i_{sb} \\ i_{sc} \end{bmatrix} + L_m \begin{bmatrix} i_{ra} \\ i_{rb} \\ i_{rc} \end{bmatrix} \quad (2.27)$$

$$\begin{bmatrix} u_{ra} \\ u_{rb} \\ u_{rc} \end{bmatrix} = R_r \begin{bmatrix} i_{ra} \\ i_{rb} \\ i_{rc} \end{bmatrix} + \frac{d}{dt} \begin{bmatrix} \lambda_{ra} \\ \lambda_{rb} \\ \lambda_{rc} \end{bmatrix} \quad \begin{bmatrix} \lambda_{ra} \\ \lambda_{rb} \\ \lambda_{rc} \end{bmatrix} = L_r \begin{bmatrix} i_{ra} \\ i_{rb} \\ i_{rc} \end{bmatrix} + L_m \begin{bmatrix} i_{sa} \\ i_{sb} \\ i_{sc} \end{bmatrix} \quad (2.28)$$

These equations represents the dynamic model of an induction motor. The model can also be written in coordinate systems with two components namely dq-, qd- and  $\alpha\beta$ -reference frames in order to reduce

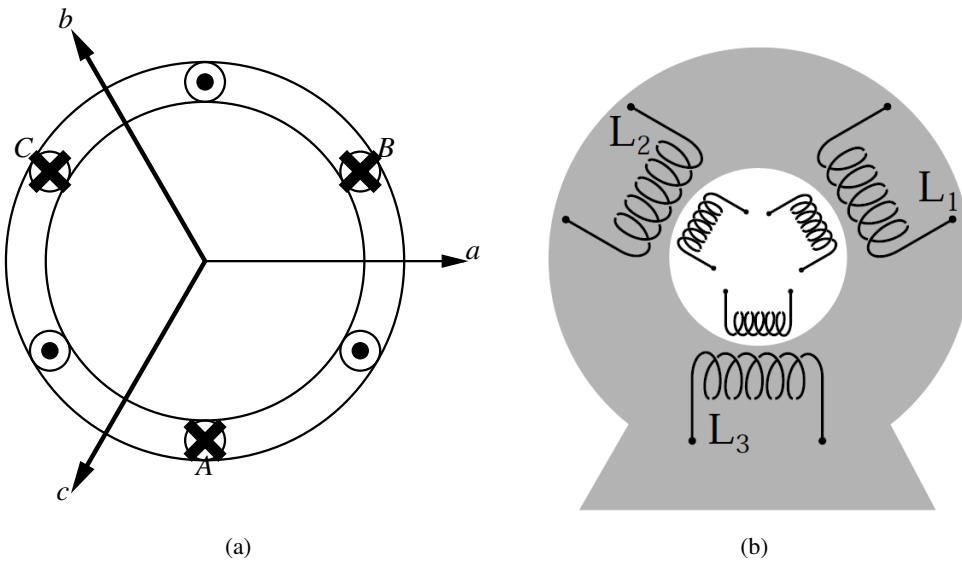


Figure 2.20: The simplified 3 coil motor model (a) and a view of the squirrel-cage rotor as three coils (b) (kilde:Danfoss)

the set of equations. Succedingly, the transformation for the reference frames which are relevant in the project will be described, hence  $\alpha\beta$ - and  $dq$ -reference frame.

#### 2.5.4.1 Clarke-transformation

In order to reduce the computational load, the 3 phase  $f_a$ ,  $f_b$  and  $f_c$  are instead expressed as a single space vector, using the following transformation, also called the Clarke transformation.

$$|\bar{f}| = K \cdot \left| f_a e^{j0} + f_b e^{j\frac{2\pi}{3}} + f_c e^{j\frac{4\pi}{3}} \right| \quad (2.29)$$

The transformation takes the scalar values of the variables in abc and rotates the variables according to the phases geometric position. Hence, each phase is modelled by fixed vectors. Adding the three vectors together will make a (space) vector rotate for balanced input as seen in figure 2.21.

The space vector  $f$  is commonly expressed via its two perpendicular components  $\alpha$  (real axis) and  $\beta$  (imaginary axis) in order to apply geometric calculations. The scalar  $k$  is added to give the transformation a desired characteristic ie.  $\frac{2}{3}$  to maintain the amplitude or  $\sqrt{\frac{2}{3}}$  to make the transformation power invariant. For the later case the proof for this can be seen by evaluating equation 2.30.

$$P = 3R I_{3-phase}^2 = 3R \left( \sqrt{\frac{2}{3}} I_{2-phase} \right)^2 = 2R I_{2-phase} \quad (2.30)$$

For the former case  $k = \frac{2}{3}$  can be chosen to maintain the same amplitude for balanced input. Say the amplitude of the 3-phase is set to 1, then the instantaneous values of the three phases at  $t = 0$ , are given as

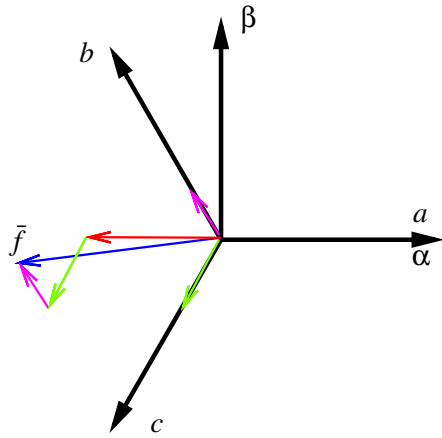


Figure 2.21: the simplified 3 coil motor model

$$f_a = 1 \cdot \sin(0) = 0 \quad (2.31)$$

$$f_b = 1 \cdot \sin\left(\frac{2\pi}{3}\right) = \frac{\sqrt{3}}{2} \quad (2.32)$$

$$f_c = 1 \cdot \sin\left(-\frac{2\pi}{3}\right) = -\frac{\sqrt{3}}{2} \quad (2.33)$$

which means the amplitude of the vector is given as

$$|\bar{f}| = k \left| f_a e^{j0} + f_b e^{j\frac{2\pi}{3}} + f_c e^{-j\frac{2\pi}{3}} \right| = k \left| 0 + \frac{\sqrt{3}}{2} e^{j\frac{2\pi}{3}} - \frac{\sqrt{3}}{2} e^{-j\frac{2\pi}{3}} \right| \quad (2.34)$$

$$= k \left| 0 + \frac{\sqrt{3}}{2} \left( \frac{1}{2} + j \frac{\sqrt{3}}{2} \right) - \frac{\sqrt{3}}{2} \left( \frac{1}{2} - j \frac{\sqrt{3}}{2} \right) \right| = k \left| 0 + j \frac{3}{2} \right| = k \frac{3}{2} \quad (2.35)$$

so as it can be seen the  $k$  needs to be  $\frac{2}{3}$  for  $\bar{f}$  to maintain an amplitude of 1 as well. Utilizing this coefficient for the Clarke transformation on the  $abc$  stator and rotor equations yields the following set of equations.

$$u_{s\alpha\beta} = R_s i_{s\alpha\beta} + \frac{d\lambda_{s\alpha\beta}}{dt} \quad (2.36)$$

$$u_{r\alpha\beta} = R_r i_{r\alpha\beta} + \frac{d\lambda_{r\alpha\beta}}{dt} \quad (2.37)$$

$$\lambda_{s\alpha\beta} = L_s i_{s\alpha\beta} + L_m i_{r\alpha\beta} \quad (2.38)$$

$$\lambda_{r\alpha\beta} = L_r i_{r\alpha\beta} + L_m i_{s\alpha\beta} \quad (2.39)$$

### 2.5.4.2 Park-transformation

The problem with the  $\alpha\beta$ -transformation is that the vector representing the stator and rotor vectors are rotating relative to the reference frame. This makes it more difficult to apply classical control theory to obtain zero steady state error for a ramp input since the system including the controller has to be of type 2 (2 free integrators). It is therefore of interest to find a rotating reference frame that rotates with the vectors. This will make the vector appear constant relative to the reference frame. For some control strategies it is beneficial that the reference frame is fixed on the rotor flux as will be obvious in section 4.7. The relation between the stator fixed and the rotating arbitrary reference frames can be seen illustrated in figure 2.22.

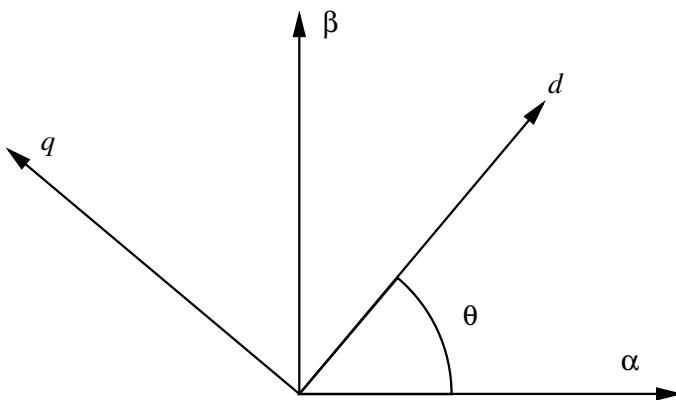


Figure 2.22: Relationship between the  $\alpha\beta$  and the  $dq$  reference frame

Using Euler's formula it is possible to transform a  $\alpha\beta$  reference frame to a  $dq$  reference frame. It requires rotation of the stator space vector by the mathematical equation expressed in 2.40.

$$f_{dq} = e^{-j\theta} \bar{f} \quad (2.40)$$

Applying this transformation, it can be shown that the voltage and flux linkage equations for the motor will be given by equations 2.41-2.44, when  $dq$ -reference frame is rotating with angle  $\omega_0$ . Notice, the angular velocity  $\omega_r$  in the rotor voltage equation. The reference frame rotation observed by the rotor is relative its own rotation but in the case of rotor fixed reference frame this term cancel out.

$$u_{sdq} = R_r i_{rdq} + \frac{d\lambda_{rdq}}{dt} + j\omega_0 \lambda_{rdq} \quad (2.41)$$

$$u_{rdq} = R_r i_{rdq} + \frac{d\lambda_{rdq}}{dt} + j(\omega_0 - \omega_r) \lambda_{rdq} \quad (2.42)$$

$$\lambda_{sdq} = L_s i_{sda\beta} + L_m i_{rd\alpha\beta} \quad (2.43)$$

$$\lambda_{rdq} = L_r i_{rq\alpha\beta} + L_m i_{sq\alpha\beta} \quad (2.44)$$

Comparing equation 2.41 to equation 2.36 shows one more term in the  $dq$ -reference frame. This extra term for the stator voltages comes from differentiation of the term (1) in:

$$e^{-j\theta} u_{\alpha\beta} = e^{-j\theta} R_s i_{\alpha\beta} + \underbrace{e^{-j\theta} \frac{d\lambda_{s\alpha\beta}}{dt}}_{(1)} \quad (2.45)$$

Using the product rule of differentiation for a rotor fixed the last term can be rewritten to

$$\frac{de^{-j\theta}\lambda_{s\alpha\beta}}{dt} = e^{-j\theta} \frac{d\lambda_{s\alpha\beta}}{dt} + \frac{de^{-j\theta}}{dt} \lambda_{s\alpha\beta} \Leftrightarrow \quad (2.46)$$

$$e^{-j\theta} \frac{d\lambda_{s\alpha\beta}}{dt} = \frac{de^{-j\theta}\lambda_{s\alpha\beta}}{dt} - \frac{de^{-j\theta}}{dt} \lambda_{s\alpha\beta} = \frac{d\lambda_{sdq}}{dt} - \frac{de^{-j\theta}}{dt} e^{j\theta} \lambda_{sdq} \quad (2.47)$$

$$= \frac{d\lambda_{sdq}}{dt} + j\dot{\theta} e^{-j\theta} e^{j\theta} \lambda_{sdq} = \frac{d\lambda_{sdq}}{dt} + j\omega_r \lambda_{sdq} \quad (2.48)$$

Similar calculations can be carried out for the rotor voltage equations to derive the extra term.

### 2.5.5 Instantaneous torque equation of the motor

The instantaneous input power to the motor,  $P_{in}$ , is given by the mechanical power of the motor,  $P_{mec}$ , the change of energy stored in the magnetic field,  $W_{mf}$ , and the power dissipated due to the core loss,  $P_{rlloss}$ , see question 2.49

$$P_{in} = P_{rlloss} + \frac{dW_{mf}}{dt} + P_{mec} \quad (2.49)$$

As mentioned in the assumptions the core loss is neglected, meaning  $P_{mec}$  can be expressed as

$$P_{mec} = P_{in} - \frac{dW_{mf}}{dt} \quad (2.50)$$

Through derivations it can be shown that this can be written as equation 2.51, where  $\omega_r$  is the electrical angular velocity of the rotor.

$$P_{in} - \frac{dW_{mf}}{dt} = \frac{3}{2} \omega_r L_m (i_{qs} i_{dr} - i_{ds} i_{dr}) \quad (2.51)$$

The instantaneous mechanical power can also be written as the product of the torque of the motor,  $\tau_m$ , and the mechanical angular velocity of the rotor,  $\omega_m$ .

$$P_{mec} = \tau_m \omega_m \quad (2.52)$$

The torque equation of the motor is thus given by

$$\tau_m = \frac{P_{mec}}{\omega_m} = \frac{3}{2} \frac{\omega_r}{\omega_m} L_m (i_{qs} i_{dr} - i_{ds} i_{dr}) \quad (2.53)$$

Where it is used that  $\omega_r$  and  $\omega_m$  relate by the number of pole pairs,  $p_b$

$$\omega_r = p_b \omega_m \quad (2.54)$$

$$\omega_e = \omega_r - s \omega_e \quad (2.55)$$

equation 2.55 shows how the synchronous angular velocity,  $\omega_e$ , and the slip,  $s$ , relate to  $\omega_r$ .

## 2.6 Go-cart model

In order to fully understand the system, a mathematical model of the mechanical system is needed. This model is used for simulating the total system with the motor model to see how it reacts under specific conditions. Furthermore, it is used for simulating how a chosen control strategy influences the system. The go-cart is modeled using a free body diagram and applying Newton's 2<sup>nd</sup> law, which yields:

$$\sum F_x = m_{tot} \cdot \ddot{x} \quad (2.56)$$

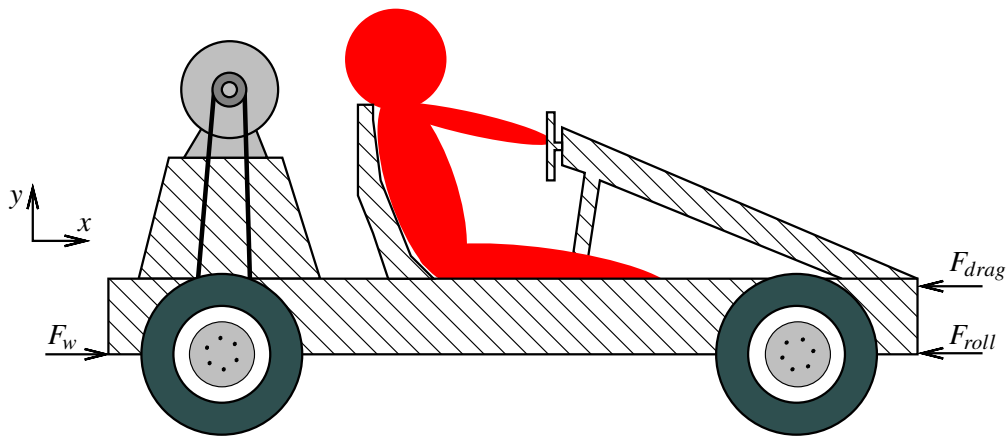


Figure 2.23: Free body diagram of the go-cart, with definitions of forces and references. The forces in the  $y$  direction are neglected.

The forces acting on the go-cart in the  $x$  direction are the drag force ( $F_{drag}$ ), rolling resistance ( $F_{roll}$ ) and force from the wheel to the ground ( $F_w$ ) created by the applied torque from the motor. Equation 2.56 then becomes:

$$F_w - F_{drag} - F_{roll} = m_{tot} \cdot \ddot{x} \quad (2.57)$$

The dragforce is described by the relation between front area of the go-cart with driver,  $A_{front}$ , the density of the air traveled through,  $\rho$ , at the velocity,  $\dot{x}$ , and the drag coefficient,  $C_d$ .

$$F_{drag} = \frac{1}{2} \cdot \rho \cdot C_d \cdot A_{front} \cdot \dot{x}^2 \quad (2.58)$$

The drag coefficient and front area for a similar go-cart is found in [23] to be:  $C_d = 0.804$  and  $A_{front} = 0.57484 [m^2]$ . These go-carts are almost alike, and because the governing part of both the drag and front area is subject to the drivers geometry these constants are deemed valid for this project. The go-cart is modeled using a free body diagram and applying Newtons 2<sup>nd</sup> law, which yields:

The force from the rolling resistance is given by equation 2.59. The rolling resistance coefficients  $c_1$  and  $c_2$  are also found in [23].

$$F_{roll} = M_{tot}g(c_1 + c_2v) \quad (2.59)$$

The force from the wheel to the ground comes from the torque of the motor,  $\tau_m$ , transfer via the gearing with the ratio  $G_r$  to the wheel with the radius  $r_w$ .

$$F_w = G_r \frac{\tau_m}{r_w} \quad (2.60)$$

The equations can be combined in order to derive a transfer function from torque  $\tau_m(s)$  to velocity  $\dot{x}(s)$ . Inserting all the terms and linearising the nonlinear terms yield the following expression:

$$\tau_m(s) \cdot \frac{G_r}{r_w} - \rho \cdot C_d \cdot A_{front} \cdot \dot{x}(s) - M_{tot} \cdot g \cdot c_2 \cdot \dot{x}(s) = s \cdot M_{tot} \cdot \dot{x}(s) \quad (2.61)$$

Collecting the velocities and rearranging the terms yields the following transfer function.

$$\begin{aligned} \tau_m(s) \cdot \frac{G_r}{r_w} &= \dot{x}(s) \cdot (\rho \cdot C_d \cdot A_{front} + M_{tot} \cdot g \cdot c_2 + s \cdot M_{tot}) \\ \frac{\dot{x}(s)}{\tau_m(s)} &= \frac{\frac{G_r}{r_w}}{s \cdot M_{tot} + \rho \cdot C_d \cdot A_{front} + M_{tot} \cdot g \cdot c_2} \end{aligned} \quad (2.62)$$

As seen the transfer function is a first order system and calculating the terms reveals a mechanical time constant  $\tau_{mech} =$ . The bode plot for the system is shown in figure 2.24. The only comments that can be addressed to this plot is that the mechanical system is a type 0 system, thus there will be steady state error for a step input. If instead position control was desired a free integrator is introduced increasing the type and removing the steady state error for a step input.

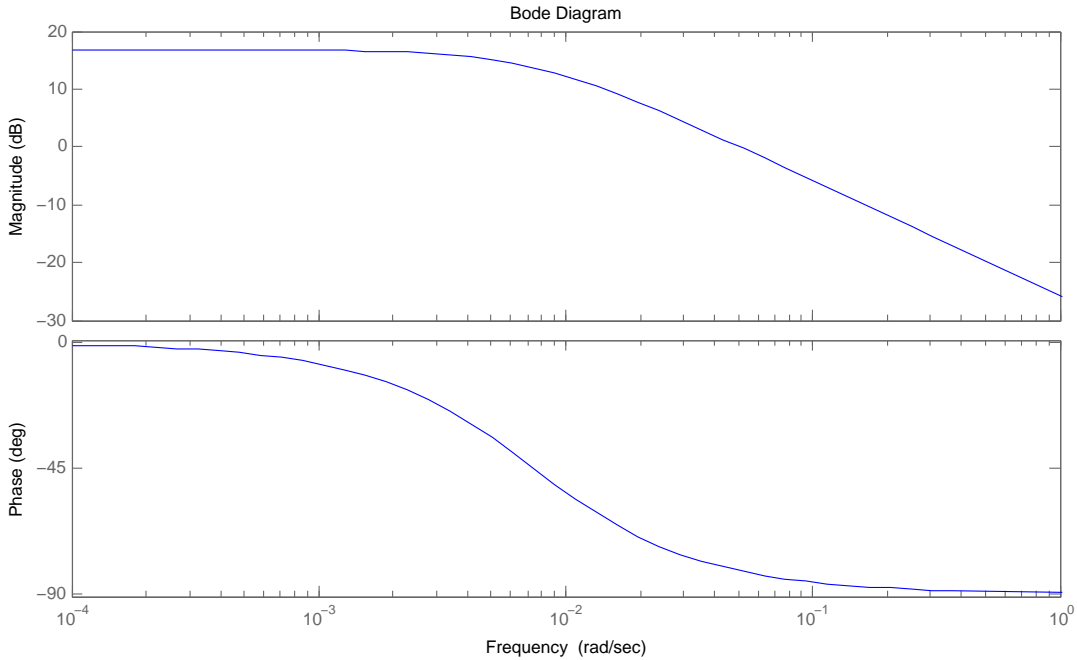


Figure 2.24: Bodeplot of the mechanical system from motor torque to output velocity

## 2.7 Parameter Estimation

The parameters of the Induction Motor Model has to be measured in order to obtain a correct model. The parameters obtained from the nameplate of the motor are not sufficient in view of contradictory parameter values from different sources. The general method to estimate the motor parameters involves a *blocked-rotor test* and a *no-load test*. Both test methods have been considered, but there have been some practical obstacles, that have required alternative methods. No power supply able of delivering the rated 24[VAC] and 189[A] for the induction machine have been available. Furthermore, a blocked-rotor test have not been possible to perform due to limitations at the test setup. Instead different methods are considered to estimate the parameters. Firstly, a method called Prediction-Error Minimization Method (PEM) is considered.

### 2.7.1 Prediction-Error Minimization

If the system is perceived linear, the input, output and noise at the time  $t$  may be described by the Linear Difference Equation (LDE):

$$y(t) + a_1y(t-1) + \cdots + a_{n_a}y(t-n_a) = b_1u(t-1) + \cdots + b_{n_b}u(t-n_b) \quad (2.63)$$

In vector form the LDE may be written as:

$$y(t) = \varphi_n^T \theta \quad (2.64)$$

Where  $\theta$  contains the coefficients for the LDE, and  $\varphi(t)$  contains the inputs and outputs of the system.

$$\theta = [a_1 \cdots a_n \ b_1 \cdots b_n]^T \quad (2.65)$$

$$\varphi_n(t) = [-y(t-1) \cdots -y(t-n) \ u(t-1) \cdots u(t-n)) \quad (2.66)$$

depends on the parameters of  $\theta$  the notation  $\hat{y}(t|\theta)$  is introduced. Given that  $N$  samples have been taken from a systems input and output,  $Z^N$ , it now only remains to find parameter vector,  $\theta$ , that results in the minimum error,  $\varepsilon(t)$ , between actual system output,  $y(t)$ , and the estimated output,  $y(t|\theta)$ .

$$Z^N = [u(1) \ y(1) \ \cdots \ u(N) \ y(N)] \quad (2.67)$$

$$\varepsilon(t) = y(t) - \hat{y}(t|\theta) = y(t) - \varphi_n^T \theta \quad (2.68)$$

This can be done by using the least square method

$$V(\theta) = \frac{1}{2} \frac{1}{N} \sum_{t=1}^N (y(t) - \varphi^T(t)\theta)^2 \quad (2.69)$$

since  $V(\theta)$  is a positive second order function of  $\theta$  it has a minimum. The minimum of the performance function can be found by setting its derivative to zero.

$$\frac{dV(\theta)}{d\theta} = -\frac{1}{N} \sum_{t=1}^N \varphi(t)(y(t) - \varphi^T(t)\theta) \quad (2.70)$$

$$= -\frac{1}{N} \sum_{t=1}^N \varphi(t)y(t) + \frac{1}{N} \sum_{t=1}^N \varphi(t)\varphi^T(t)\theta = 0 \Leftrightarrow \quad (2.71)$$

$$\sum_{t=1}^N \varphi(t)y(t) = \sum_{t=1}^N \varphi(t)\varphi^T(t)\theta \Leftrightarrow \quad (2.72)$$

$$\theta = \left[ \sum_{t=1}^N \varphi(t)y(t) \right]^{-1} \sum_{t=1}^N \varphi(t)\varphi^T(t)\theta \quad (2.73)$$

In order for  $\theta$  to be the minimum of  $V(\theta)$  its Hessian also has to be positive definite.

$$\frac{\delta^2 V}{\delta \theta_j^2} = \frac{\delta}{\delta \theta_j} \left( -\frac{1}{N} \sum_{t=1}^N \varphi(t)(y(t) - \varphi^T(t)\theta) \right) = \frac{1}{N} \sum_{t=1}^N \varphi(t)\varphi^T(t) \quad (2.74)$$

### 2.7.1.1 Linear difference model of the induction motor

The linear difference model of the induction machine will be derived using the steady state equivalent circuit model which is given in equation . This model describes the steady state performance for input voltage  $U_s$  and output current  $I_s$ . Expanding this equation in to a more general arrangement gives the following expression.

$$\frac{I_s}{U_s} = \frac{s \cdot (L_{lr} + L_m) + \frac{R_r}{s_l}}{s^2 \cdot (L_{ls} \cdot (L_{lr} + L_m) + L_m \cdot L_{lr}) + s \cdot \left( R_s \cdot (L_{lr} + L_m) + L_{ls} \cdot \frac{R_r}{s_l} + L_m \cdot \frac{R_r}{s_l} \right) + \frac{R_r \cdot R_s}{s_l}} \quad (2.75)$$

with  $s$  being the Laplace operator and  $s_l$  the slip. Marking the coefficient with the following names makes the succeeding calculations easier to digest.

$$\begin{aligned} b_1 &= L_{lr} + L_m \\ b_2 &= \frac{R_r}{s_l} \\ a_1 &= L_{ls} \cdot (L_{lr} + L_m) + L_m \cdot L_{lr} \\ a_2 &= R_s \cdot (L_{lr} + L_m) + L_{ls} \cdot \frac{R_r}{s_l} + L_m \cdot \frac{R_r}{s_l} \\ a_3 &= \frac{R_r \cdot R_s}{s_l} \end{aligned}$$

First the bilinear transformation is used ( $s \approx \frac{2}{T} \cdot \frac{1-Z^{-1}}{1+Z^{-1}}$ ) to discretize the transfer function, then the equation are rearranged for the  $z^{-n}$  terms and finally the difference equation is obtained in a straight forward manner.

$$\begin{aligned} \frac{I_s}{U_s} &= \frac{\left(\frac{2}{T} \cdot \frac{1-Z^{-1}}{1+Z^{-1}}\right) \cdot b_1 + b_2}{\left(\frac{2}{T} \cdot \frac{1-Z^{-1}}{1+Z^{-1}}\right)^2 \cdot a_1 + \left(\frac{2}{T} \cdot \frac{1-Z^{-1}}{1+Z^{-1}}\right) \cdot a_2 + a_3} \\ \frac{I_s}{U_s} &= \frac{\left(\frac{2}{T} \cdot (1-Z^{-1}) \cdot (1+Z^{-1})\right) \cdot b_1 + (1+Z^{-1})^2 \cdot b_2}{\left(\frac{2}{T} \cdot (1-Z^{-1})\right)^2 \cdot a_1 + \left(\frac{2}{T} \cdot (1-Z^{-1}) \cdot (1+Z^{-1})\right) \cdot a_2 + (1+Z^{-1})^2 \cdot a_3} \\ \frac{I_s}{U_s} &= \frac{\frac{2}{T} \cdot (1+Z^{-2}) \cdot b_1 + (1+Z^{-2}+2 \cdot Z^{-1}) \cdot b_2}{\left(\frac{4}{T^2} \cdot (1+Z^{-2}-2 \cdot Z^{-1})\right) \cdot a_1 + \left(\frac{2}{T} \cdot (1+Z^{-2})\right) \cdot a_2 + (1+Z^{-2}+2 \cdot Z^{-1}) \cdot a_3} \\ \frac{I_s}{U_s} &= \frac{Z^{-2} \cdot \left(\frac{2}{T} \cdot b_1 + b_2\right) + Z^{-1} \cdot (2 \cdot b_2) + \left(\frac{2}{T} \cdot b_1 + b_2\right)}{Z^{-2} \cdot \left(\frac{4}{T^2} \cdot a_1 + \frac{2}{T} \cdot a_2 + a_3\right) + Z^{-1} \cdot \left(\frac{-8}{T^2} \cdot a_1 + 2 \cdot a_3\right) + \left(\frac{4}{T^2} \cdot a_1 + \frac{2}{T} \cdot a_2 + a_3\right)} \quad (2.76) \end{aligned}$$

Once again new coefficients are defined in order to write a more simple equation. The following terms are collected:

$$\begin{aligned} d_1 &= \frac{2}{T} \cdot b_1 + b_2 \\ d_2 &= 2 \cdot b_2 \\ d_3 &= \frac{2}{T} \cdot b_1 + b_2 \\ c_1 &= \frac{4}{T^2} \cdot a_1 + \frac{2}{T} \cdot a_2 + a_3 \\ c_2 &= \frac{-8}{T^2} \cdot a_1 + 2 \cdot a_3 \\ c_3 &= \frac{4}{T^2} \cdot a_1 + \frac{2}{T} \cdot a_2 + a_3 \end{aligned}$$

The difference equation becomes

$$\begin{aligned} i_s \cdot (c_3 + c_2 \cdot Z^{-1} + c_1 \cdot Z^{-2}) &= u_s \cdot (d_3 + d_2 \cdot Z^{-1} + d_1 \cdot Z^{-2}) \\ i_s(t) + i_s(t-1) \cdot \frac{c_2}{c_3} + i_s(t-2) \cdot \frac{c_1}{c_3} &= u_s(t) \cdot \frac{d_3}{c_3} + u_s(t-1) \cdot \frac{d_2}{c_3} + u_s(t-2) \cdot \frac{d_1}{c_3} \end{aligned}$$

Now, the difference equation is obtained it can be transformed into the general form with  $\theta$  and  $\phi$

$$\theta = \left[ \frac{c_2}{c_3} \frac{c_1}{c_3} \frac{d_2}{c_3} \frac{d_1}{c_3} \right]^T \quad (2.77)$$

$$\phi_n(t) = [-i_s(t-1) - i_s(t-2) \ u_s(t) \ u_s(t-1) \ u_s(t-2)] \quad (2.78)$$

The algorithm can now be used using data from the induction machine for steady state measurements. Actually, the term steady state in this model only refers to the constant slip value. As long as the slip stays constant, the steady state equations should be able to predict the currents in the system. Nonetheless, it is difficult to obtain constant slip for different frequencies without a controller so data is desired to be collected at specific frequencies. After exciting the system with inputs such as random noise, step input, constant input and ramp input the difference equation could not be estimated entirely. The best result obtained is shown in figure 2.25 which shows good coherence at some frequencies. In spite of this, the method cannot be used since the estimated discrete transfer function has to be converted back to the unknown parameters ( $R_r$ ,  $L_{ls}$ ,  $L_{lr}$  and  $L_m$ ).

The pem method has proven to result in numerical errors due to transformations needed between continuous and discrete time. This is also evident from the definition of the tustin approximation:

$$s = \frac{1}{T} \ln(z) \quad (2.79)$$

$$= \frac{2}{T} \left[ \frac{z-1}{z+1} + \frac{1}{3} \left( \frac{z-1}{z+1} \right)^3 + \frac{1}{5} \left( \frac{z-1}{z+1} \right)^5 + \frac{1}{7} \left( \frac{z-1}{z+1} \right)^7 + \dots \right] \quad (2.80)$$

$$\approx \frac{2}{T} \frac{z-1}{z+1} \quad (2.81)$$

It is only the first order approximation of equation 2.79 that is used. The calculations has simply showed that this is not enough. Therefore it is chosen to go on with a strategy that instead deploys a continuous strategy.

## 2.7.2 Optimization using least mean square

This strategy uses the idea of minimizing the least mean square of the error between the measured output and the estimated output, see figure 2.26 for an illustration of how the method minimizes the sum of the errors

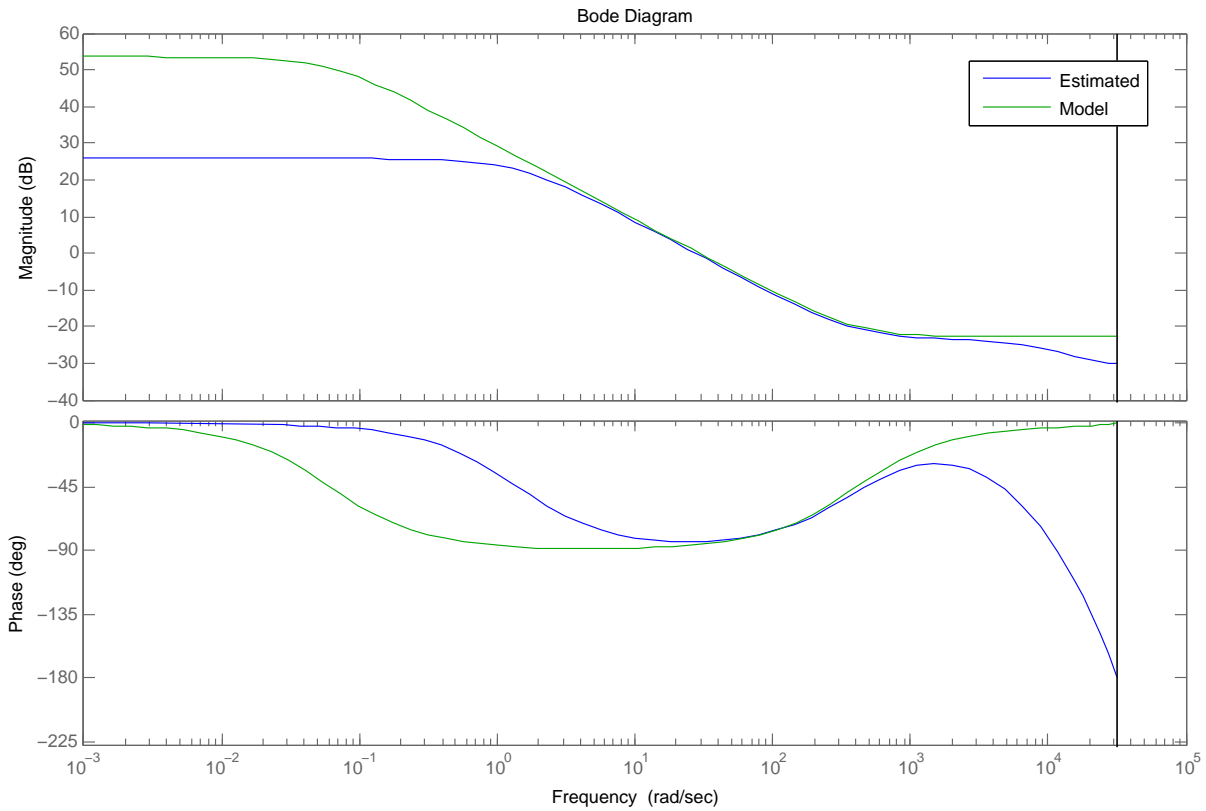


Figure 2.25: Bode plot of the steady state transfer function discretized from parameters obtained from other cites and the estimated discrete transfer function

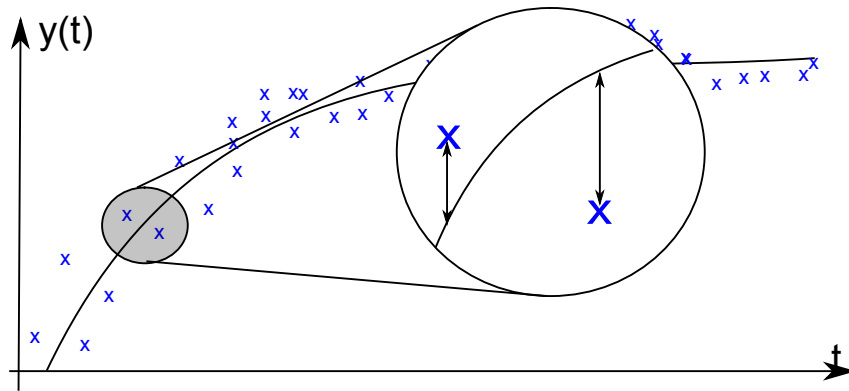


Figure 2.26: Output signal from a continuous time model (black) and the sampled data from the system to estimate (blue). The least mean square method sums the error between the sampled data and the model response.

The outputs are separated in rotor current  $I_r$  and magnetization current  $I_m$ . For high frequencies the most of the current from  $I_s$  flow through  $I_r$  and for low frequencies the current flows through  $I_m$ . The estimated outputs are found by using the transfer functions 2.82 and 2.83.

$$\frac{I_r}{U_s} = \frac{1}{(L_{ls} + L_{lr})s + R_s + R_r} \quad (2.82)$$

$$\frac{I_m}{U_s} = \frac{1}{(L_{ls} + L_{lm})s + R_s} \quad (2.83)$$

The brief derivation below shows that this actually is the case when the core loss is here disregarded.

$$I_s = I_m + I_r \quad (2.84)$$

$$I_m = I_s \cdot \frac{Z_r}{Z_r + Z_m} = I_s \cdot \frac{sL_{lr} + R_r}{s(L_{lr} + L_m) + R_r} \quad (2.85)$$

$$I_r = I_s \cdot \frac{Z_m}{Z_r + Z_m} = I_s \cdot \frac{sL_{lm}}{s(L_{lr} + L_m) + R_r} \quad (2.86)$$

For  $s \rightarrow \infty$  this results in the following quantities.

$$I_m = I_s \cdot \frac{L_r}{L_{lr} + L_m} = 3.8E - 4 \cdot I \quad (2.87)$$

$$I_r = I_s \cdot \frac{L_m}{L_{lr} + L_m} = 1 \cdot I \quad (2.88)$$

In similar fashion it can be shown that for low frequencies most of the current from  $I_s$  will flow through  $I_m$ . This means that depending signal applied to the terminal only the inner or the outer loop needs to be considered.

In order to validate this a Sallen-Key filter is introduced. This filter has narrow passband which can be specified so only the frequencies within the bandwidth are left untouched and the remaining frequencies are attenuated. The equation for the filter is given by:

$$H = \frac{G \cdot B \cdot s}{s^2 + B \cdot s + \omega_0^2} \quad (2.89)$$

where  $G$  is the gain [dB] in the bandwidth,  $B$  is the width of the passband [rad/s] and  $\omega_0$  [rad/s] is the geometric center frequency of the bandwidth. Utilizing this filter the noise from the signal can be damped, the fundamental frequency can be identified using a FFT (Fast Fourier Transformation) in order to excite the model with the same signal. This is expected to ease the LMS method to estimate the correct parameters.

Figure 2.27 shows the output of the motor and the output of model, both having their signals filtered. As can be seen there is both a change in the phase and the amplitude is higher in the simulations, thus this method also does not show feasible results.

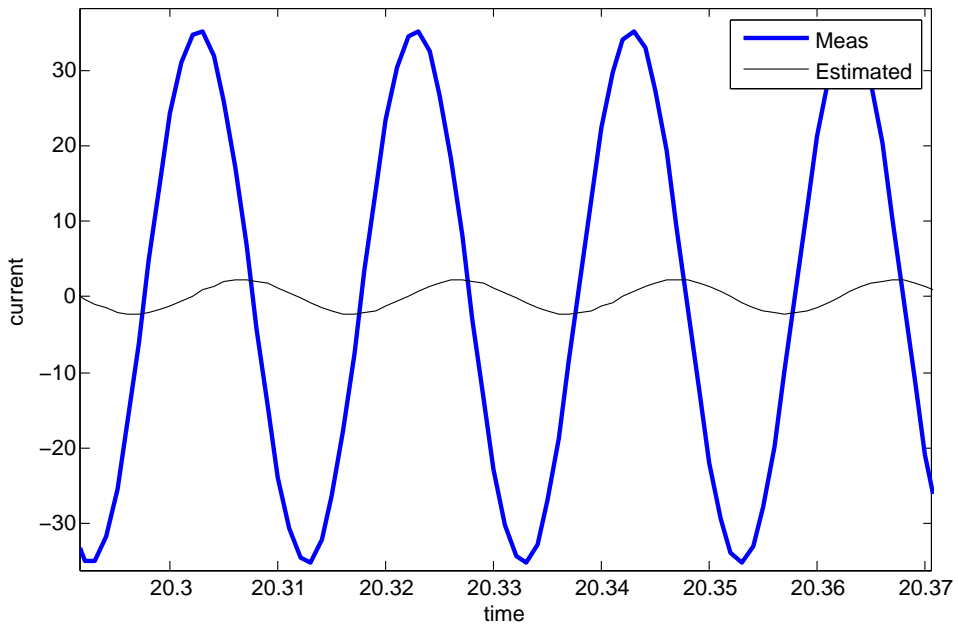


Figure 2.27: LMS estimation using optimization

## 2.8 Validation of the induction motor model

The mathematical model must first be verified to be able to use the induction motor model for designing and testing of different controllers.

### 2.8.1 Test method

The validation will be based on the states that are measured in the tests, which are the voltages, the currents and the rotational speed. In all tests the measured phase voltages on the motor terminals are used as inputs to the MATLAB ® Simulink model. Subjecting the model to the same input as the motor receives should, in the case that the motor model is correct, give the same currents and speed. First the steady state performance of the motor and model will be compared, then the dynamic behavior during a series of succeeding step inputs on the speed reference, using a simple  $\frac{v}{f}$  control. Further description of the test can be found in section A.3

### 2.8.2 Steady state performance

The motor is supplied with 50 [Hz] RMS phase voltages of 1.41 [V], without load, and the rotor spins to 1431 [RPM], corresponding to a slip of 4.6%. Applying the same voltages and conditions to the model, and it predicts a slip of 4.4% which corresponds to a rotational speed of 1434 [RPM]. These values are relatively close to each other.

The phase currents at steady state are plotted in Figure 2.28

As it is evident from Figure 2.28 the currents are of approximately the same size, the difference in RMS values of the current are; 25.9 [A] for the measured, and 29.3 [A] for the model, this is a difference of

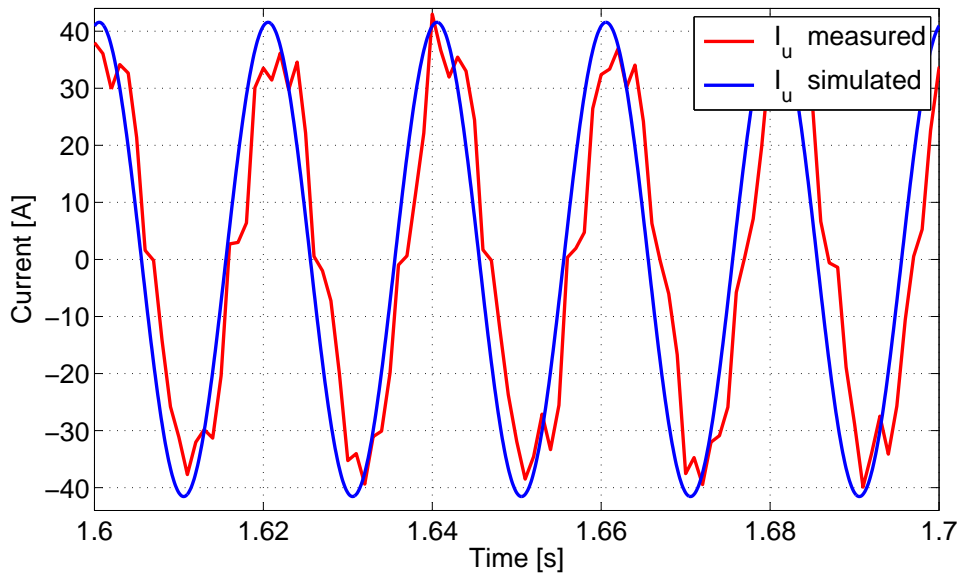


Figure 2.28: Measured and simulated currents at steady state

13 %. This could possibly be caused by a voltage drop in the cables from the inverter to the motor and a small difference in the load model.

The previous comparisons of the predicted and the measured states of the induction motor are assumed to be sufficient to deem the model valid in steady state, as no tests with a known load were conducted.

### 2.8.3 Dynamic performance

The dynamic performance of the model will be validated against measured data, with the motor mounted on the go-cart and connected to the rear axle. The added inertia and friction from the rear axle and drive chain is approximated, by trial and error, estimated to be 3 times the inertia of the motor and 5 times the viscous friction. These factor for viscous friction seems to be in a reasonable range, as there are two small ball bearings in the motor and three larger ones on the rear axle, plus added friction from the chain drive. These two factors are the same used all the plots in this section.

As in the steady state validation the only measured internal states are the currents and the rotational speed. Therefore the validation will be based on these states.

The motor is subjected to a series of step inputs as seen in Figure 2.29. The MATLAB ® Simulink model is tested with the measured phase voltages, and the simulated responses are plotted against the measured.

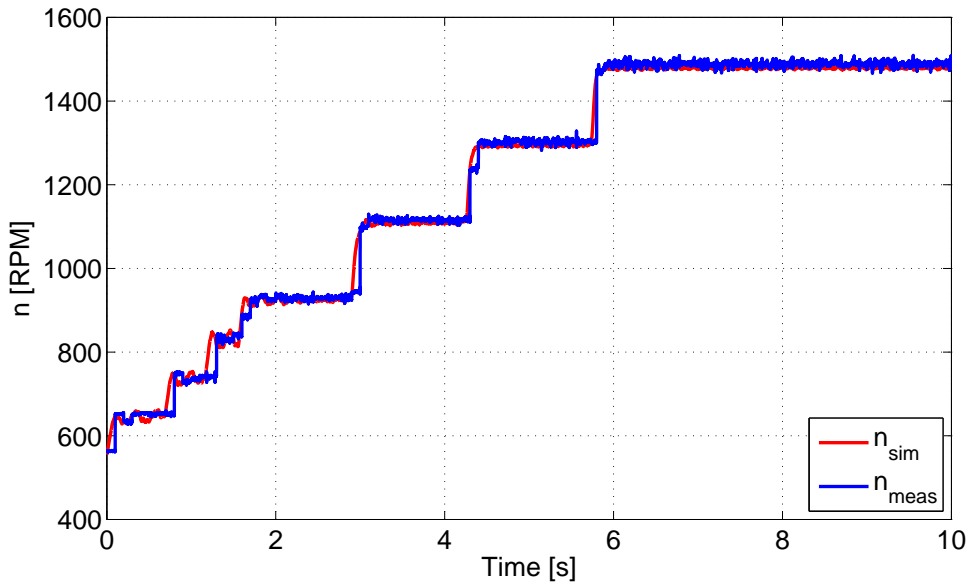


Figure 2.29: Measured and simulated speed during the full dynamics test, consisting of 7 succeeding steps

In Figure 2.29 both responses seems to be similar. To highlight the differences the first 2.5 [s] are shown in figure Figure 2.30.

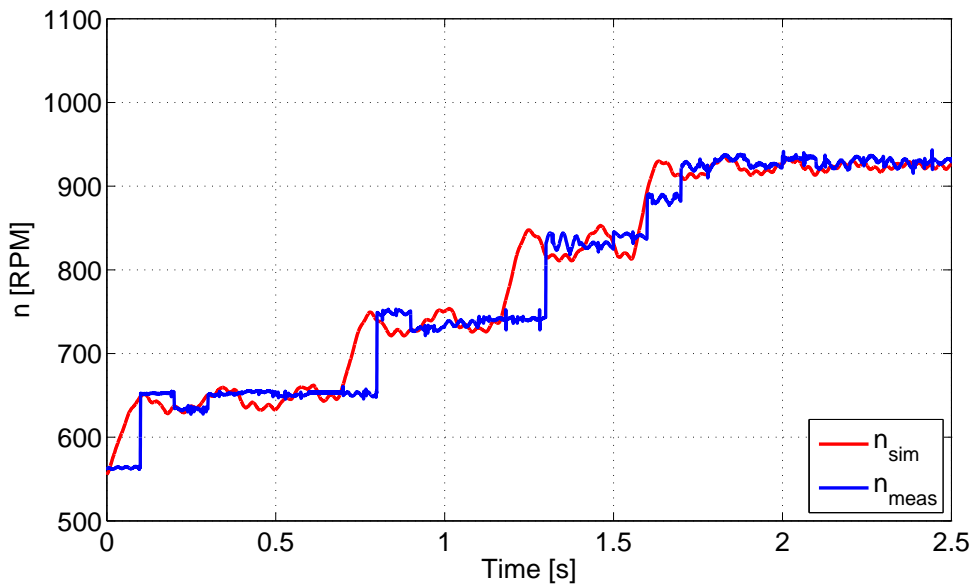


Figure 2.30: Zoomed wiew on the first 2.5 [s] of Figure 2.29, of the measured and simulated speed during the dynamics test

The closer look at the transitions at the step inputs, reveals that the simulated responses seems to react earlier than the measured responses. The model has a realistic response at the steps, whereas the measured response shows an almost instant velocity change. Looking closer at this change reveals what

appears to be a fault in the measured data series. The frequency measurement routine used in the Lab-view program are located in a different loop than the other measurements. This frequency loop gathers 100 samples and sends them to the other loop that appends them to the file. The second loop runs at 10 [Hz] appending 100 samples from both the ADC and the frequency measurement. This gives a sampling frequency of 1 [kHz]. The data from the frequency measurement seems to be distorted in series of 100 samples (0.1 [s]) before the rapid changes in velocity, as it can be seen in Figure 2.31

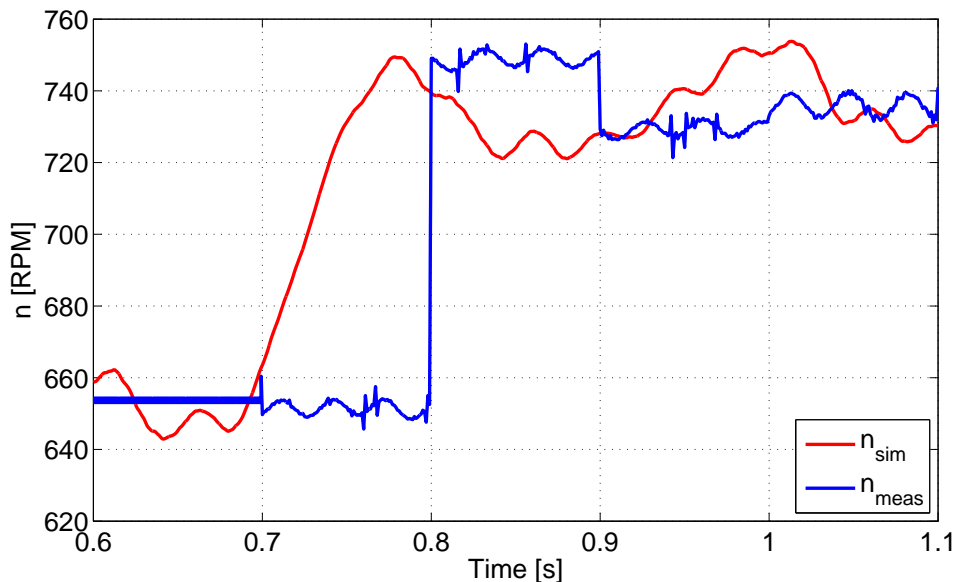


Figure 2.31: Close up look at the distorted frequency measurements. The samples before the frequency change are grouped in series of 0.1 [s]

The rotational speed of the simulation is very close to the measured, and it could be improved by adjusting the friction and inertia, but as the aim is to use the model with a different load, there is no real need for more accurate results as long as the model is validated.

To further verify the model, the measured voltages are compared to the simulated currents. To let the plots be easily interpreted only currents from the U phase are plotted.

In Figure 2.33 the measured currents from the full test are plotted, and as it can be seen large currents are conducted right at the steps as expected when the synchronous speed is suddenly changed.

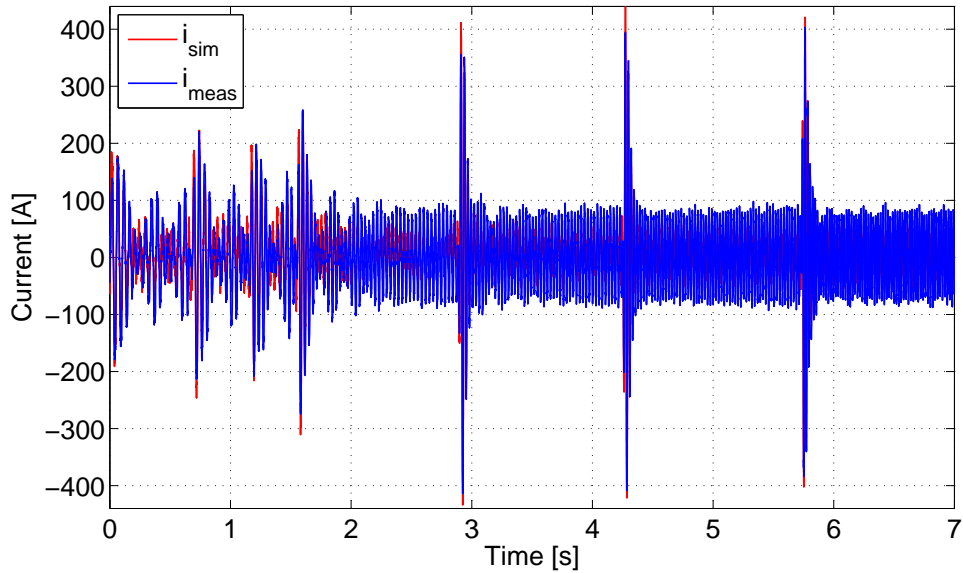


Figure 2.32: Current spike of the step input at 5.7 [s] in Figure 2.33.

For the dynamic model to be valid it should be fairly accurate in the transient periods of the test, therefore the points of interest are at the current "spikes". The fluctuations in the current in the beginning of the test are plotted in Figure 2.34.

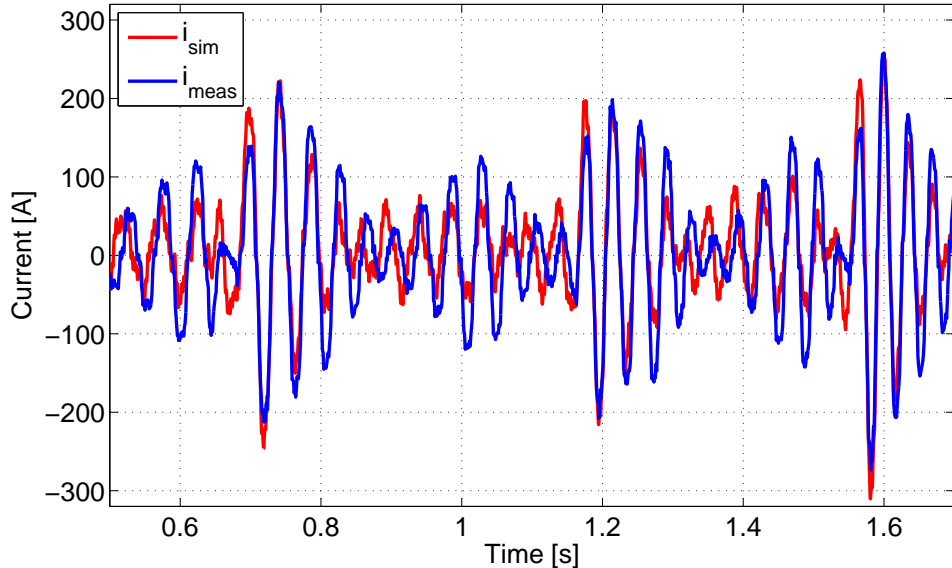


Figure 2.33: Measured and simulated currents of the full test

As it is seen in Figure 2.34 the amplitude and phase of the currents are similar, only with small deviations, that most likely are caused by measurement errors or noise. Another currents spike is investigated in Figure 2.32.

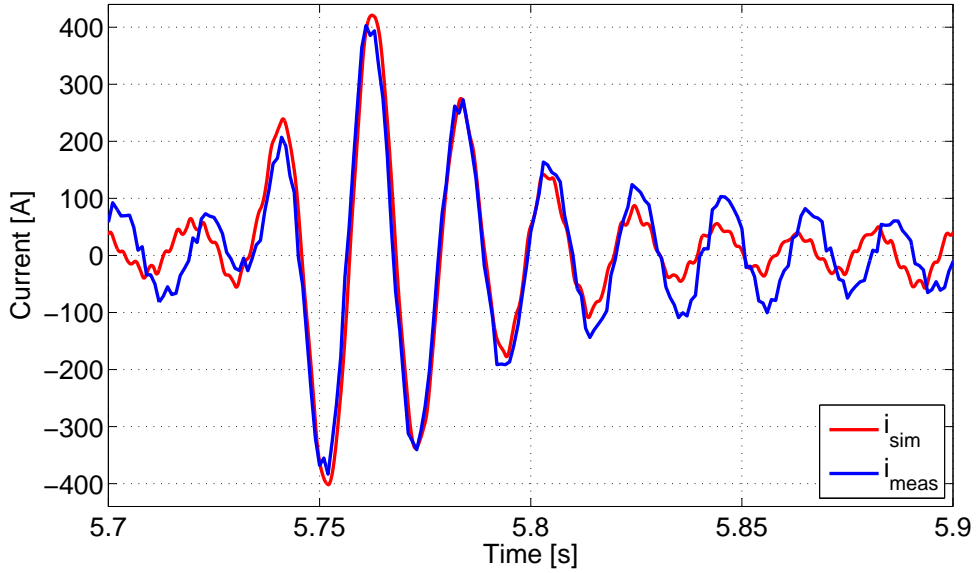


Figure 2.34: Measured and simulated current response in the beginning of the test

The current spikes in Figure 2.32 are well predicted, by the model, but at the previous and following cycles the amplitudes are smaller in the model, which suggest that the friction coefficients used in the simulation are underestimated, but as stated above this is not a concern, as the mechanical model is to be used as load for the further design. The induction motor model is hereby concluded to be valid.

## 2.9 Performance estimation

To estimate the expected performance of the go-cart, aerodynamic parameters from a rapport on a similar go-cart are used [23], together with the previous presented data. The parameters are presented in table 2.4.

Parameter	Symbol	Value
Front area of go-cart	$A_{front}$	$0.57484[m^2]$
Drag-coefficient of go-cart	$C_{drag}$	$0.9[N/kg]$
Rolling resistance coefficient	$C_{rr0}$	$0.027[\cdot]$
Rolling resistance coefficient, speed dependent	$C_{rr1}$	$-5.114 \cdot 10^{-4}[\cdot]$
Mass of go-cart and driver	$M_{gc}$	$250[kg]$
Density of air	$\rho$	$1[kg/m^3]$
Gravitation acceleration	$g$	$9.81[N/kg]$
Gear ratio	$G_{ratio}$	$1.75[\cdot]$
Radius of the rear wheel	$r_{wheel}$	$0.1375[m]$

Table 2.4: Parameters for performance estimation.

To estimate the run time with the selected configuration of the go-cart, the required motor torque,  $\tau_{mech}$ , and steady state current,  $I_{rms}$ , at the selected nominal velocity,  $v = 50[km/t] = 13.89[m/s^2]$  is calcu-

lated in equation 2.90 and 2.91. With the selected gear ratio of,  $G_{ratio} = 1.75[\cdot]$ , the motor will run at  $1688[rpm] \Rightarrow \omega_r = (1688 \cdot 2 \cdot \pi)/60 = 176.77$  to archive the desired  $50[km/t]$ .

$$\tau_{mech} = \frac{r_{wheel} \cdot M_{gc} \cdot g \cdot (C_{rr0} + C_{rr1} \cdot v) + r_{wheel} \cdot \rho \cdot v^2 \cdot C_{drag} \cdot A_{front}}{G_r} = 7.75[Nm] \quad (2.90)$$

$$I_{rms} = \frac{\tau_{mech} \cdot \omega_r}{\sqrt{3} \cdot \frac{U_{DC}}{\sqrt{2}} \cdot \cos(\phi) \cdot \eta} = 34.98[A] \quad (2.91)$$

The battery selected in section 2.2.1 is a deep cycle battery, meaning it is designed to endure many charge / discharge cycles without losing significant capacity. To prolong the life of the battery it is however recommended not to discharge it under 80% of its capacity [11]. This reveals an estimated drivetime at a constant speed of  $50[km/h]$  of:

$$Drivetime = \frac{Capacity[Ah] \cdot 0.8}{I_{rms}[A]} = 1.26[hour] \quad (2.92)$$

The calculated drive time for constant speed can not be compared to the drive pattern normal for a go-cart circuit, that will include repeatedly acceleration and braking due to the layout of the circuit. The increased current draw during accelerating will obviously reduce the drive time substantially. The actual expected drive time could be analyzed further by simulations.

To be able to drive the go-cart and control the speed, a controller is needed. This can be based on and tested in the validated dynamic model.

---

# Problem statement

---

# 3

The problem analysis leads to the following problem statement:

Which control strategies and PWM method would be beneficial to implement on a electrical go-cart powered by batteries.

Given that it needs to be power by batteries certain requirements to the strategies needs to be considered:

- minimizing power-losses
- minimizing start up currents
- maximizing the drive range of a single charge

While keeping the requirements it is also desirable to optimize the performance of the go-cart .



---

# Problem solution

---

4

## 4.1 Pulse Width Modulation of the phases

The Pulse Width Modulation is method for emulating an analogue value from a digital out. The basic idea is to generate an average DC value by filtering out high frequencies from the switchings in the periodical digital puls output. By changing the width of the periodical pulses, the filtered output DC value changes. If the sampling freqency is set sufficiently lower than the fundamental frequency of a desired sinusoidal, PWM can also be using to generate this signal.

### 4.1.1 Generating the PWM

With regards to implementation of the PWM signals for the inverter there generally exists 2 different forms of implementation. One uses space vector theory to calculate the length of the pulses, this is described in 4.2. The other one uses triangular intersection to create the pulses. The basic idea is illustrated in figure 4.1.

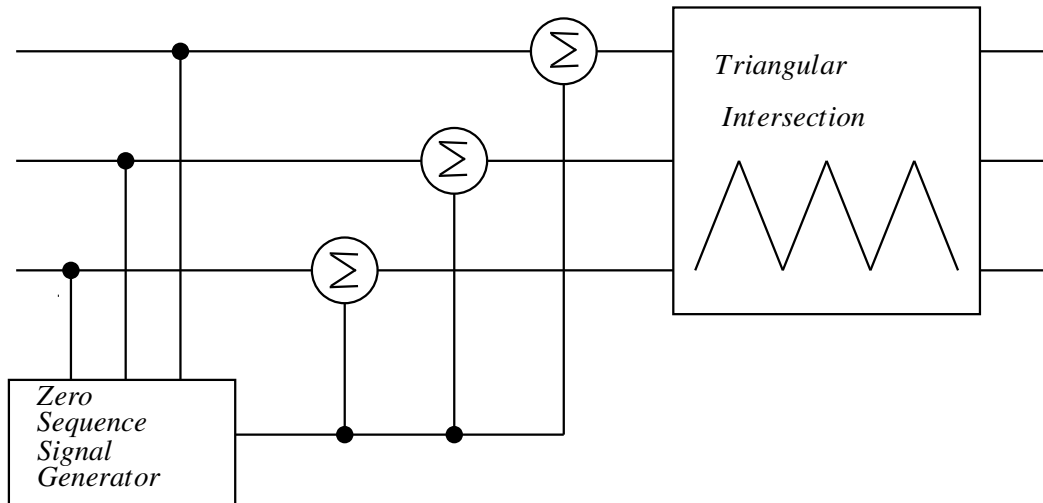


Figure 4.1: Implementation of Triangular intersection

The concept is to add a zero sequence signal to the fundamental signal, and then use the intersection of the found sum and a triangular signal to create the pulses.

The idea behind the concept is that various harmonics can be injected via the zero sequence signal, giving different benefits, ie. less switching, while rotor predominantly reacts to them as if they were first

harmonic sinesoidsals.

Adding the zero sequence to the fundamental signal is simply a way of changing the common mode voltage of a signal. This is illustrated in figure 4.2.

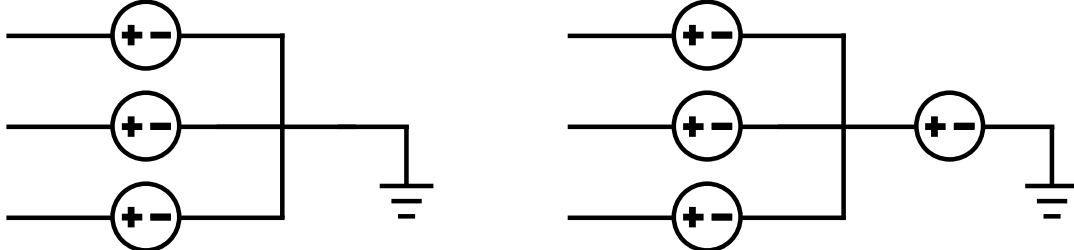


Figure 4.2: Change of the common mode voltage

Changing the common mode voltage does not change the line-to-line voltages, meaning the output of the motor will not reflect the change in common mode voltage.

#### 4.1.2 CPWM and DPWM

Within modulation strategies for PWM, there exists two categories. The Continues PWM (CPWM) and the Discontinues PWM (DPWM) strategies. The difference between the CPWM and DPWM can be seen by the fact that the DPWM will have a period in which the signal is kept at the DC-link voltage. This is due to the fact that the modulation waves are not always kept within the boundries of the triangular wave, as is the case for CPWM. Three commonly known CPWMs are: SPWM, THIPWM and SVPWM, of the three SVPWM is most used. Eventhough THIPWM is the one with the theoretical least harmonic distortion, SVPWM is favored due to its implementation simplicity and the fact that it only has slightly more harmonic distortion then THIPWM.

## 4.2 SVPWM

The purpose of the different modulation strategies, is to emulate a fundamental sinewave form in the motor, by switching the switches according to the strategy.

The SVPWM employs space vectors to calculate switching time. Given the fact that there are 6 switches that pair-wise can either apply the DC-link voltage or its negative. This gives the possibility of  $2^3$  different switch states. Having the upper of a switch pair active, while the its lower is inactive is defined as 1. The opposite is defined as 0.

The 6 states 100 – 101 are defined as active states, while the states 000 and 111 are defined as the zero states. In the zero states there are no potential difference that can induce a current.

Any space vector can be expressed as a sum of the two adjecent active vectors of the section that it is in.

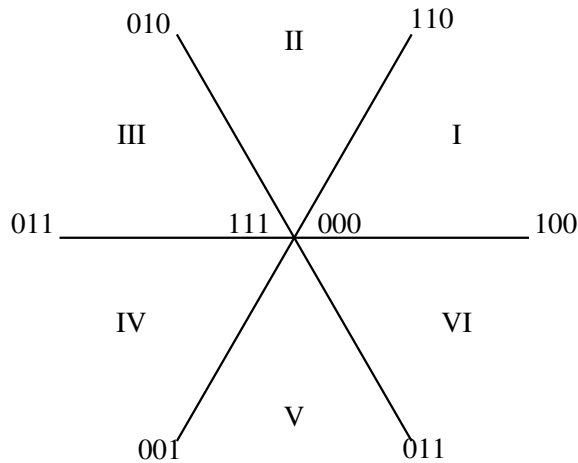


Figure 4.3: The sections and states of SVPWM

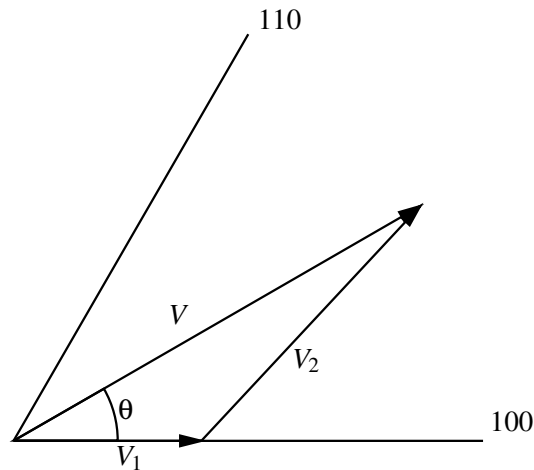


Figure 4.4: Expressing the space vector via the 2 active adjacent vectors

$$V = c_1 V_1 + c_2 V_2 \quad (4.1)$$

$c_1$  and  $c_2$  defines the time in which the inverter is in the current switch state. The total period of the pwm signal is defined by the time spent in the adjecent active vectors,  $T_1$  and  $T_2$ , and the time spent in the zero states,  $T_0$

$c_1$  and  $c_2$  are thus defined as

$$c_1 = \frac{T_1}{T} \quad c_2 = \frac{T_2}{T} \quad (4.2)$$

$T_1$  and  $T_2$  can be calculated by the following equations

$$T_1 = \frac{\sqrt{3}T_s|V|}{2V_{dc}} \sin\left(\frac{n}{3}\pi - \theta\right) \quad (4.3)$$

$$T_2 = \frac{\sqrt{3}T_s|V|}{2V_{dc}} \sin\left(\theta - \frac{n-1}{3}\pi\right) \quad (4.4)$$

$n$  defines the section the space vector is in.  $V_{dc}$  is the DC-link voltage. See appendix .4 for the derivation of the equations. Having calculated  $T_1$  and  $T_2$  the PWM signals can now be generated. The symmetric switching sequence used in figure 4.5 is used due to it being the combination of states that results in least harmonic distortion.

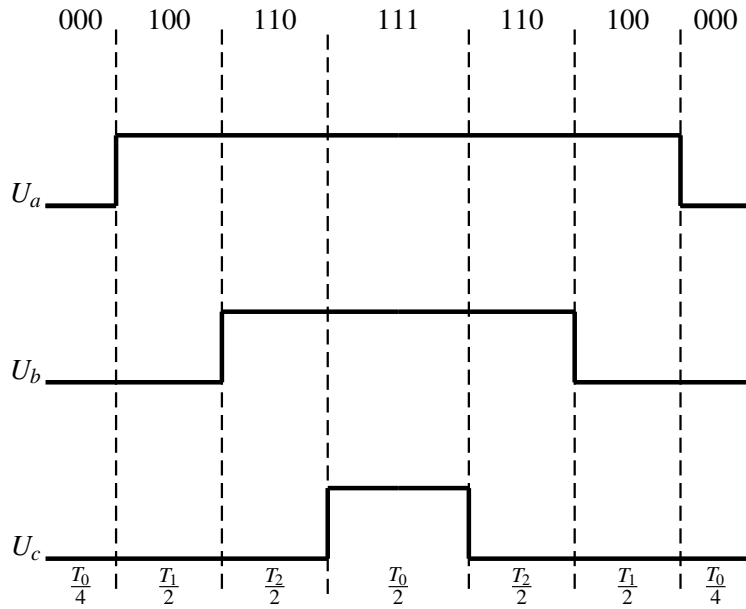


Figure 4.5: The PWM signal from SVPWM

## 4.3 DPWM

Among the DPWMs, 3 methods will here be taken into consideration.

- DPWM3: The zero sequence signal is calculated by taking the phase with the intermediate absolute value,  $|V_i|$ , and utilizing equation 4.5

$$V_0 = \text{sign}(V_i) \frac{V_{dc}}{2} - V_i \quad (4.5)$$

- DPWMMAX: The zero sequence signal is calculated by finding the phase with the maximum value,  $V_{max}$ , and utilizing equation 4.6

$$V_0 = \frac{V_{dc}}{2} - V_{max} \quad (4.6)$$

- DPWMMIN: The zero sequence signal is calculated by finding the phase with the minimum value,  $V_{min}$ , and utilizing equation 4.7

$$V_0 = \frac{V_{dc}}{2} - V_{min} \quad (4.7)$$

## 4.4 Losses from harmonic distortion and switching

Since go-cart is driven by batteries, it is of interest to minimize the losses that are caused by the modulation. The losses can be divided into two categories.

1. The harmonic distortion losses: These losses come from the injected zero sequence to the common mode voltage.
2. The switching losses: The losses that are an effect of switching the MOSFETs

The first is introduced due to the motors filtering effect, while the latter happens in the inverter itself.

### 4.4.1 Losses from harmonic distortion

To examine the losses from the harmonic distortion the following two relations are set up, where  $a_m$ ,  $b_m$  and  $c_m$  are specific for the various modulation methods.

$$HDF = a_m M_i^2 + b_m M_i^3 + c_m M_i^4 M_i = \frac{\pi |V|}{2V_{dc}} \quad (4.8)$$

The HDFs used in the report are taken from [24] and can be found in appendix .5.1. Collectively they give a good impression of how the harmonic distortions of the different methods relatively to each other act depending on the size of  $M_i$ . As  $M_i$  is basically defined by how much of the  $V_{dc}$  is utilized, the harmonic distortion is thus influenced hereby. Figure 4.6 shows the graphs for HDFs for the three DPWMs and SVPWM.

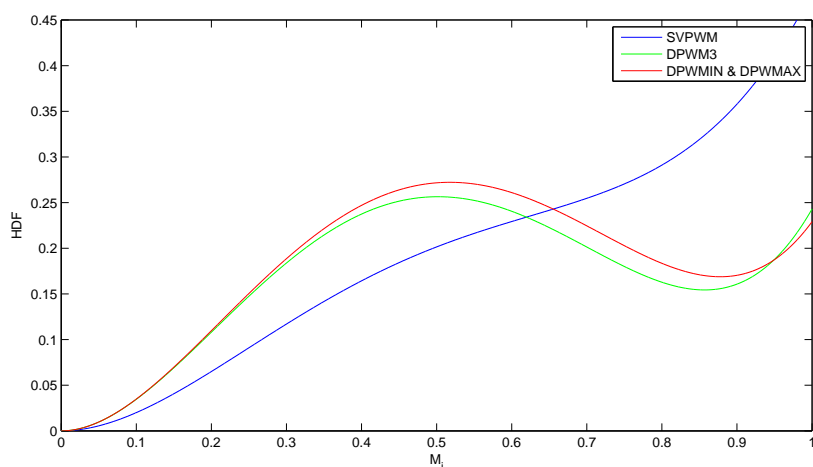


Figure 4.6: HDF of SVPWM, DPWMMIN, DPWMMAX, DPWM3

As can be seen in figure 4.6 for low values of  $M_i$ , the SVPWM is favored due to it having low harmonic distortion, while the DPWM methods are favored at higher values of  $M_i$ . The ideal strategy would thus be to used SVPWM for  $[0; M_{ix}]$ , ( $M_{ix}$  is defined the intersection between the CPMW and DPWM) and switch to ie. DPWM3 for higher values of  $M_i$ .

#### 4.4.2 Losses from harmonic distortion

Looking solely at the HDFs for the DPWMs the DPWM3 method is the most favorable. However, when taking switching losses into account the perspective may change.

Since the CPWMs do not have periods where  $V_a + V_0$  exceeds the amplitude of the triangular wave signal, all the CPWMs have the same switching loss, which thus also is higher than that of the DPWMs. Say the switching loss of CPWM per fundamental cycle is given by  $P_0$ , then the Switching Loss Functions (SLF) for the different DPWMs methods can be described by

$$SLF = \frac{P_{swave}}{P_0} \quad (4.9)$$

Where  $P_{swave}$  is the switch loss per fundamental cycle inverter per device. The SLF for the 3 mentioned DPWMs are taken from [24] and can be found in appendix .5.2. Figure 4.7 shows the Switching Loss Functions, (SLF), of the 3 DPWM. Note that the SLF for DPWMMAX and DPWMMIN are the same. The SLFs used can be found in appendix .5.2

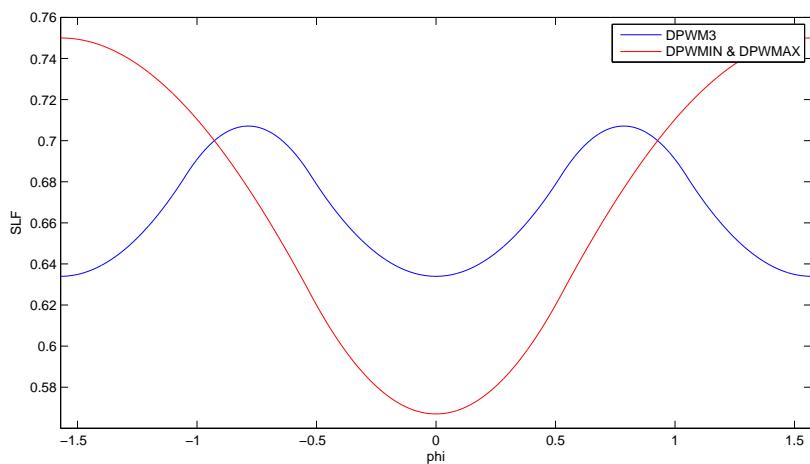


Figure 4.7: SLFs of DPWMMIN, DPWMMAX and DPWM3

As can be seen on figure 4.7 the SLF is dependent of the phase current power factor angle,  $\phi$ . The optimal strategy would thus be to switch DPWM method according to the value of  $\phi$ .

## 4.5 Switching between modulation strategies

Finally the question also arises whether switch between 2 the strategies in mid run would lead to further harmonic distortion. It is here assumed that if there is no harmonic distortion between 2 of the modulation methods, there will also be no harmonic distortion between any other combination of switching between the 3 methods.

In order to check this a simulation of the cases below is made:

1. implementation of SVPWM
2. implementation of DPWMMAX
3. implementation of SVPWM for  $M_i \leq M_{ix}$  and DPWMMAX for  $M_i > M_{ix}$

Figure 4.8 shows the block diagram of the simulation. *motora*, *motorb* and *motorc* are the outputs of a low pass filter, which in this case would represent the motor, subtracted the influence from the zero sequence for each voltage.

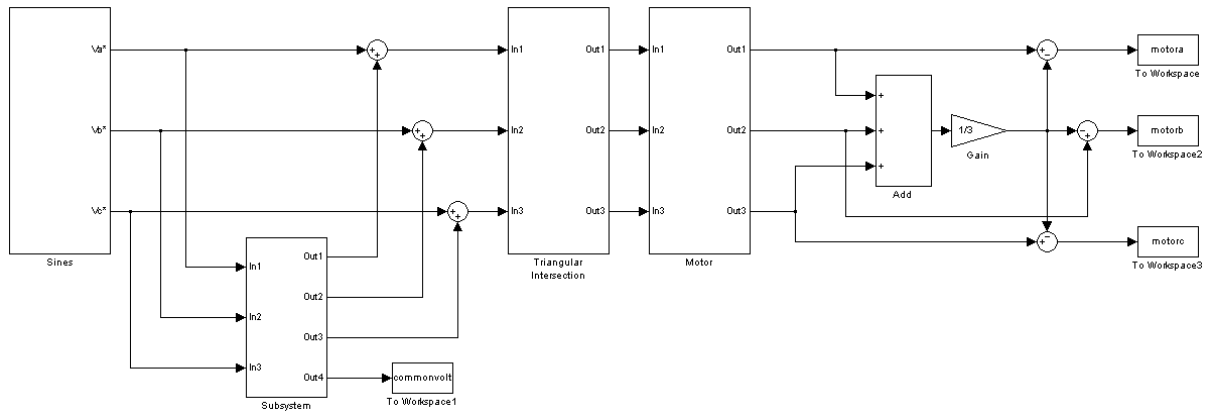


Figure 4.8: Block diagram of the simulation

The zero sequence from case 3 is displayed in figure 4.9. Here is can be seen how the switch between PWM methods happens at 0.083.

Looking solely at *motora* for the 3 cases it does seem that the switching between the 2 method has any impact on *motora*, these are shown in figure 4.10.

However, solely looking at the 3 graphs from figure 4.10 it can not be determined whether the switching of methods does introduce harmonic distortion. To see if this is the case a FFT of the signals are made, see figure 4.11

As it can be seen there is hardly a difference to spot, it is thus concluded that the strategy of switching between SVPWM and DPWMMAX is worth implementing.

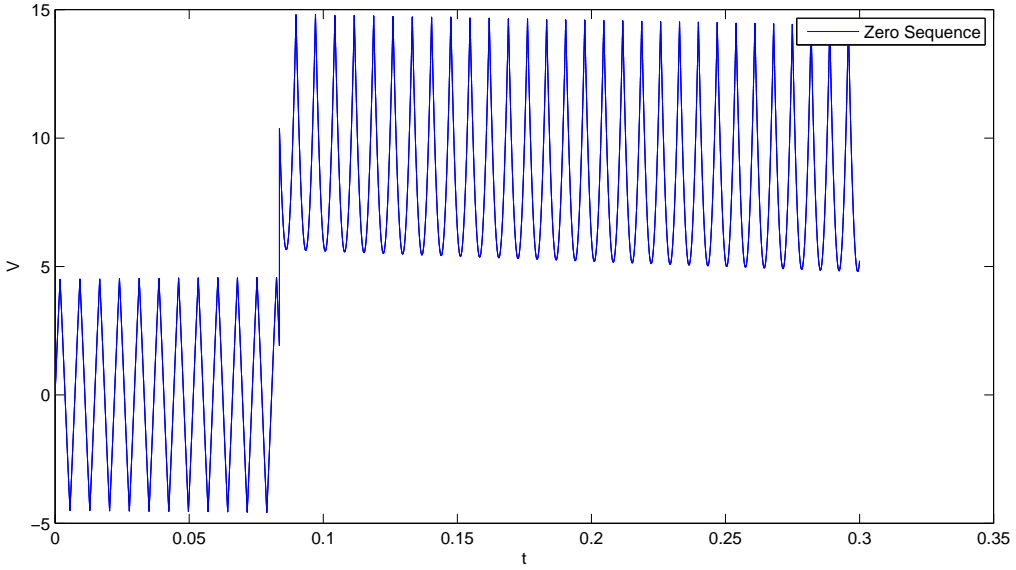


Figure 4.9: Zero Sequence of case 3

## 4.6 Design optimisation

## 4.7 Scalar Control

An induction motor is capable of delivering the rated torque for all frequencies with scalar control. The idea behind scalar control is to keep the ratio between the voltage and the frequency constant. The thoughts behind this idea, is best illustrated using the single phase lumped parameter model of the induction motor, see figure 4.12. For variable frequencies the inductive impedances will change, thus changing the currents modeling the airgap flux, copper losses in the rotor and the mechanical output power. The power transmission in an induction motor happens through the airgap flux. By keeping the airgap flux constant the motor will be capable to deliver the rated torque for any frequency given a load is present.

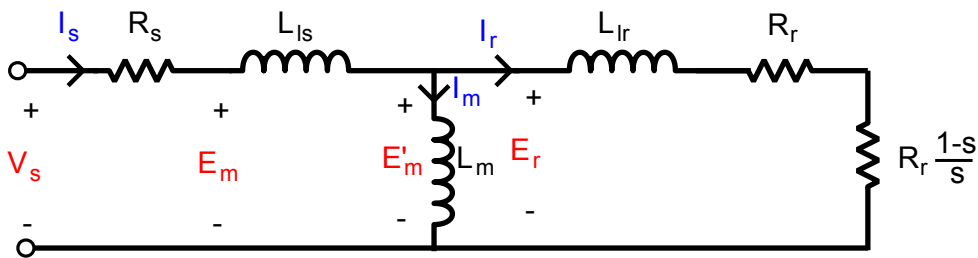
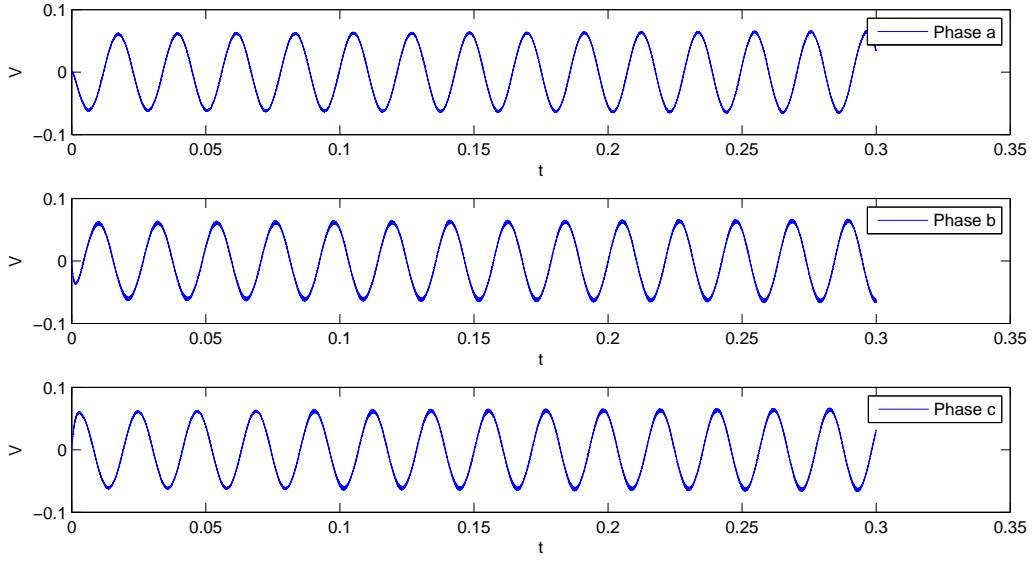


Figure 4.12: A lumped parameter model of an induction motor with the voltage terminal  $E_m$  representing the target of the scalar control

In order to understand why the voltage-frequency ratio should be kept constant, a detailed examination of the airgap flux  $\theta_{AG}$  is necessary. The airgap flux  $\theta_{AG}$  is modeled through the magnetization inductor  $L_m$  and the magnetization current  $I_m$  in the lumped parameter model. It is also known that the flux linkage

Figure 4.10: *motora* for the 3 cases

between two coils is given as the product of the flux produced by the coil and the number of windings. See equation 4.10 for the mentioned relation.

$$\lambda_m = L_m \cdot i_m(t) = N_s \cdot \theta_{AG}(t) \quad (4.10)$$

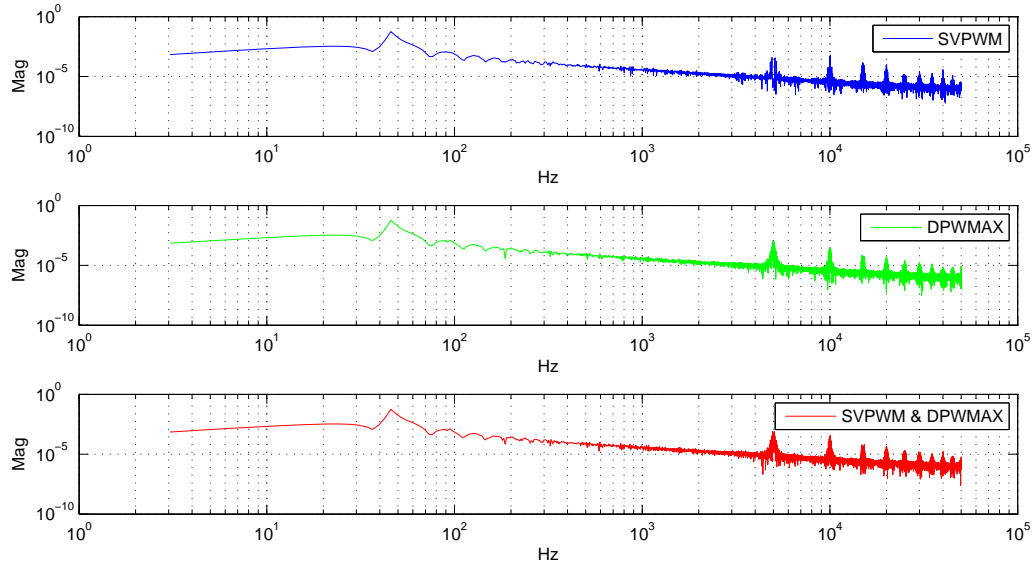
where  $N_s$  is the equivalent number of turns per stator phase and  $\lambda_m$  is the flux linkage between the stator and the rotor.

Assuming the input voltage is sinusoidal, the magnetization current hence the airgap flux linkage will inevitably also be sinusoidal. Using faradays law, the voltage drop over  $L_m$  is given as in equation 4.11, with

$$\begin{aligned} E_{m'} &= N_s \cdot \frac{d\theta_{AG}(t)}{dt} \\ &= L_m \cdot \omega \cdot \theta_{AG} \cdot \cos(\omega \cdot t) \\ &= L_m \cdot \omega \cdot I_m \cdot \cos(\omega \cdot t) \end{aligned} \quad (4.11)$$

Taking the RMS value and rearranging the equation shows how to keep the magnetization current  $I_m$  and airgap flux  $\theta_{AG}$  constant.

$$\frac{E_{m'}}{\omega} = \frac{L_m}{\sqrt{2}} \cdot I_m = \frac{N_s^2}{\sqrt{2}} \cdot \theta_{AG} \quad (4.12)$$


 Figure 4.11: FFT of *motora* for the 3 cases

### 4.7.1 Deriving an expression for airgap flux

The voltage drop over the magnetization and the rotor branch in parallel inclusive the leakage in the stator is marked with  $E_m$ . Aiming for this internal terminal  $E_m$  with the scalar control will keep the airgap flux approximately constant since the leakage inductance  $L_{ls}$  is generally much lower than the magnetization inductance  $L_m$ . In order to determine the relationship between the voltages  $V_s$ ,  $E_m$  and the current  $I_s$  KVL is used for the inner loop [25].

$$V_s - i_s \cdot R_s - E_m = 0 \quad (4.13)$$

Since the voltage  $E_m$  is dependent on the impedance of the motor there will be an angle on this component when comparing with the input voltage  $V_s$ . This yields an arbitrary triangle in vector space in the complex plane, see figure 4.13.

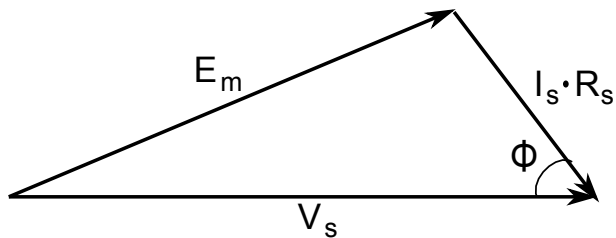


Figure 4.13: Vector representation from the KVL terms in the electric circuit that is modelling the induction motor

Using the law of cosines from trigonometry yields the following equation.

$$E_m^2 = V_s^2 + (i_s \cdot R_s)^2 - 2 \cdot V_s \cdot i_s \cdot R_s \cdot \cos(\phi) \quad (4.14)$$

In order to isolate  $V_s$ , which is the input to the motor, another equation is necessary. This is the reason  $V_s$  is found using another method. Using the vector space and dividing  $V_s$  in two components gives two right angled triangles, see figure 4.14

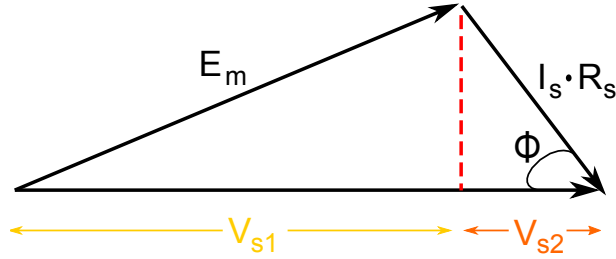


Figure 4.14: How the triangle, from the current and voltage vectors, is manipulated to obtain an expression for the input voltage  $V_s$

The two lengths that makes up  $V_s$  when added together are given in equation 4.15 and 4.16

$$V_{s1} = \sqrt{(E_m)^2 - (i_s \cdot R_s \cdot \sin(\phi))^2} \quad (4.15)$$

$$V_{s2} = i_s \cdot R_s \cdot \cos(\phi) \quad (4.16)$$

The scalar control part comes in play in equation 4.15 through the  $E_m$  component. This component needs to be replaced with a voltage that is a function of the frequency. The function is linear and based on rated parameters, see equation 4.17

$$E_m(\omega_e) = \frac{U_{rated}}{\omega_{e,rated}} \cdot \omega_e \quad (4.17)$$

Inserting equation 4.17 in equation 4.15 and multiplying this equation with equation 4.18 yields an expression for the input voltage  $V_s$  that scales the input as a function of the frequency. Further, since the dq-reference frame is attached to the space vector, the real part of the current is  $i_d$  and the imaginary part of the current is  $i_q$ . Summing up all these deriviations, gives the open loop scalar controller given in equation 4.18, that are only dependent on current measurements and the nameplate of the motor.

$$V_s = R_s \cdot i_d + \sqrt{\left(\frac{U_{rated}}{\omega_{e,rated}} \cdot \omega_e\right)^2 - (i_q \cdot R_s)^2} \quad (4.18)$$

### 4.7.2 Obtaining the desired rotor speed

A given reference frequency command  $\omega_s$  will result in a slightly reduced electrical rotor frequency  $\omega_e$ , since slip is necessary in order to produce torque. Of course, at no load condition the slip of the motor is

approximately zero even though there are some electrical and mechanical losses in the motor. The desire speed can be obtained, if the frequency command is increased with the amount of the actual slip. For this to be true, the load torque has to stay constant for any given frequency, otherwise the required torque hence the slip has to change in order to carry the load.

The torque equation for the induction motor is derived in 2.5.3. In scalar control it is not the rotor current, but the airgap flux linkage that is kept constant. Therefore it is necessary to derive an expression for the airgap flux and the rotor current.

According to equation 4.12 the flux linkage between the stator and the rotor is kept constant for proportional magnetization voltage and synchronous frequency. The rotor voltage  $E_r$  that is equal to the magnetization voltage  $E_m'$  is given in equation 4.19 and this represents the rotor winding voltage drop turns ratio transformed to the stator side.

$$E_{m'} = E_r = \underbrace{\frac{R_r}{s} \cdot I_r}_{(1)} + \underbrace{j \cdot \omega_s \cdot L_{lr}}_{(2)} \quad (4.19)$$

, where  $s$  is the rotor slip. Assuming that term (1) is much larger than term (2), since the slip is very low under normal operation, the second term can be neglected. Inserting equation 4.12 in equation 4.19 gives an expression for the rotor current that is proportional with the airgap flux linkage  $\theta_{AG}$  for constant slip  $\omega_{sl}$ , see equation 4.20.

$$I_r = \frac{N_s^2}{\sqrt{2} \cdot R_r} \cdot \omega_s \cdot s \cdot \theta_{AG} = \frac{N_s^2 \cdot \theta_{AG}}{\sqrt{2} \cdot R_r} \cdot \omega_{sl} \quad (4.20)$$

, where  $\omega_{sl}$  is the slip frequency and  $N_s$  is the equivalent number of turns between the stator and rotor.

Further more, inserting the current given in equation 4.20 in the torque equation givin in 2.23 yields the final expression for the torque as a function of the slip and the flux linkage.

$$\tau = \frac{p_b \cdot m \cdot R_r \cdot (\frac{N_s^2 \cdot \theta_{AG}}{\sqrt{2} \cdot R_r} \cdot \omega_{sl})^2}{\omega_{sl}} = \frac{p_b \cdot m \cdot N_s^4 \cdot \theta_{AG}^2}{2 \cdot R_r} \cdot \omega_{sl} \quad (4.21)$$

A typical torque frequency characteristic is given in figure 4.15.

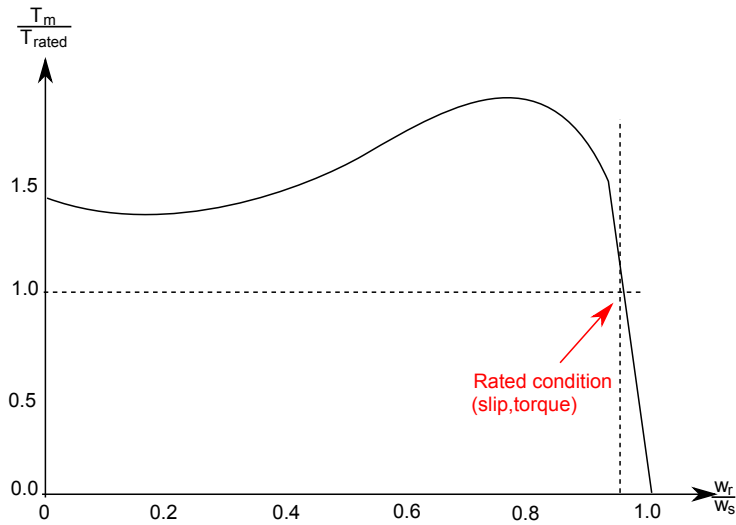


Figure 4.15: A typical torque frequency characteristic of an induction motor [14, p. 405]

Here it is seen that for low slip frequencies, which means that the rotor frequency  $\omega_r$  is very close to  $\omega_s$ , the torque is proportional to the slip. This linear relationship is weakened for larger slip values since the second term of equation 4.19 will have an increasing influence on the rotor voltage, thus rotor current and the airgap flux linkage. Because the rotor is operated around the rated frequency, this is not a concern under normal operation.

#### 4.7.3 Slip and torque estimation

Slip and torque estimation is a topic that is closely related. With the purpose of estimating the slip as a result of derivations from previous subsection, first of all the torque has to be estimated followed by the slip. After obtaining the slip estimation, the scalar controller will be able to make the motor reach a wide range of frequencies with small errors without using position or velocity feedback. Figure 4.16 shows a block diagram of the scalar controller to be implemented in the DSP.

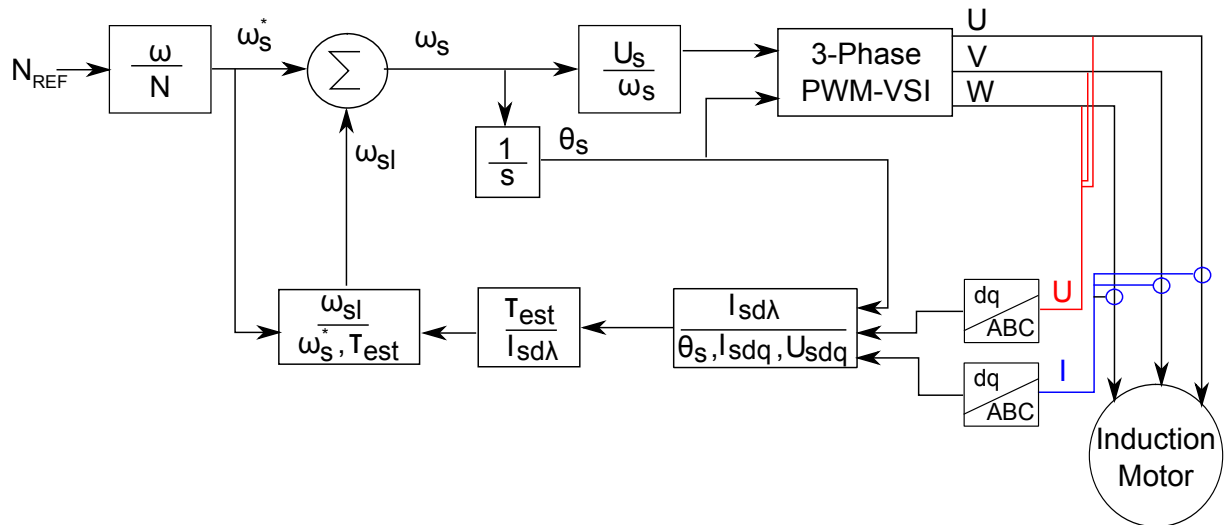


Figure 4.16: A block diagram of a scalar controller with torque and slip estimation

This controller needs stator current  $I_s$  and voltage  $U_s$  in the estimation algorithm. The current is measured with LEM modules, see section .3.2 for details, and the voltage is collected from the voltage commands to the inverter. The output voltage amplitude  $U_s$  is the scaled voltage signal that accounts for the stator voltage drop over the windings. This is given in equation 4.18. The park transformation from  $ABC$  to  $dq0$  is applied on both the current and voltage signals. Utilizing KVL on the motor model in figure 4.12 in the loop containing the supply voltage  $V_s$ , the voltage drop over the stator windings  $I_s \cdot R_s$  and the voltage drop over the remaining circuit  $E_m$  gives the vectors illustrated in figure 4.17.

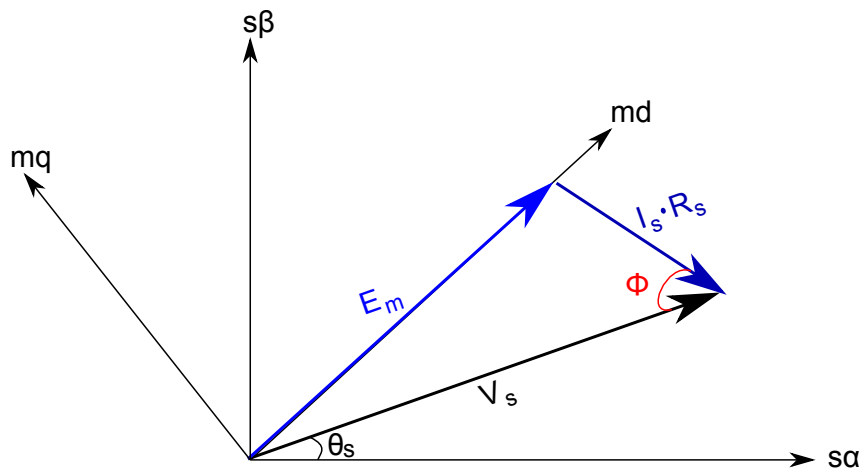


Figure 4.17: Vector representation of the space vectors for the current and voltages in a flux oriented dq reference frame

The dq reference frame is attached to the voltage vector  $E_m$  that is approximately the voltage drop over the magnetization inductance that generates the airgap flux linkage [25]. Using the general motor model given in equation 2.42 and remembering that the stator resistance  $R_s$  is accounted for in the scalar control, yields an expression for the instantaneous flux oriented stator voltage and stator flux linkage.

$$\begin{aligned} U_{msdq} &= R_s \cdot i_{msdq} + \frac{d\lambda_{msdq}}{dt} + j \cdot \omega_s \cdot \lambda_{msdq} \\ &= j \cdot \omega_s \cdot \lambda_{msdq} \end{aligned} \quad (4.22)$$

This reference frame is rotating with synchronous speed  $\omega_s$  for the reason that the reference frame is just an offset from the stator space vector. Attaching the reference frame to the voltage vector  $E_m$  means that the q-axis component will be zero, hence simplifying the equation to the following expression:

$$U_{msd} = -\omega_s \cdot \lambda_{msq} \quad (4.23)$$

The torque equation for the induction motor as a function of the stator flux linkage and the stator currents are given as:

$$\tau = \frac{m \cdot p_b}{2} \cdot Im(\lambda_{msdq}^* \cdot i_{msdq}) \quad (4.24)$$

Inserting the d and q component for the stator current  $i_{msdq}$  and equation 4.23 in equation 4.24 yields

$$\begin{aligned}
\tau &= \frac{m \cdot p_b}{2} \cdot \text{Im} \left( \left( 0 + j \cdot \left( -\frac{U_{msd}}{\omega_s} \right) \right)^* \cdot (i_{msd} + j \cdot i_{msq}) \right) \\
&= \frac{m \cdot p_b}{2} \cdot \text{Im} \left( j \cdot \frac{U_{msd}}{\omega_s} \cdot (i_{msd} + j \cdot i_{msq}) \right) \\
&= \frac{m \cdot p_b}{2} \cdot \underbrace{\frac{U_{msd}}{\omega_s} \cdot i_{msd}}_{(1)} \quad (4.25)
\end{aligned}$$

where the term (1) is constant due to scalar control, hence the term can be replaced by the rated voltage and the rated frequency  $\frac{U_0}{\omega_0}$ . When the parameters of the induction motor is given, only the flux oriented dq current needs to be calculated. In order to calculate this both the current and voltage space vectors are needed. First the angle to the  $mdq$  reference frame is calculated and afterwards the current space vector is projected to the d-axis, see following calculations.

$$\theta_{msd} = \tan \left( \frac{i_q}{i_d} \right) + \tan \left( \frac{u_q - R_s \cdot i_q}{u_d - R_s \cdot i_d} \right) \quad (4.26)$$

$$i_{msd} = \sqrt{i_d^2 + i_q^2} \cdot \cos(\theta_{msd}) \quad (4.27)$$

Now inserting this current in the torque equation in equation 4.25 gives an estimation of the torque needed to carry the load. Shifting the frequency command with this amount should make the motor reach the desired speed.

There are numerous ways to estimate the slip when the torque is given, one of the most popular methods is using the Kloss Formula [26], see equation 4.28.

$$\frac{\tau}{\tau_{max}} = \frac{2 \cdot (1 + s_{max} \cdot \frac{R_s}{R_r})}{\frac{s}{s_{max}} + \frac{s_{max}}{s} + \frac{2 \cdot s_{max} \cdot R_s}{R_r}} \quad (4.28)$$

, where the  $s_{max}$  and  $\tau_{max}$  refers the the pull-out torque and slip rates. These parameters can be calculated in following manner:

$$\tau_{max} = \frac{3 * U_s^2}{p_b * \omega_s / p_b * (R_s + \sqrt{R_s^2 + (L_s s + L_r r)^2})} \quad (4.29)$$

$$s_{max} = \frac{R_r}{\sqrt{R_s^2 + (L_s s + L_r r)^2}} \quad (4.30)$$

The Kloss Formula can be simplified based on the observation of the  $R_s$  resistor. This parameter can be neglected since the scalar control is targeted as the voltage behind this resistance i.e.  $E_m$ , following this observation both a term in the denominator and nominator can be neglected. In order to solve for the slip in the Kloss Formula requires, either has to be rewritten as a second order equation to obtain an explicit solution or approximated using assumption. Assuming that the motor will operate under small

slip values, results in the following approximation.

$$\frac{\tau}{\tau_{max}} \approx \frac{2 \cdot (1 + s_{max})}{\frac{s}{s_{max}} + \frac{s_{max}}{s}} \approx \frac{2 \cdot (1 + s_{max})}{\frac{s_{max}}{s}} \quad (4.31)$$

Rearranging the terms and multiplying with the synchronous frequency gives an estimation of the slip frequency, see equation 4.32. 2.22

$$\omega_{sl} = \frac{\tau \cdot s_{max}}{\tau_{max} \cdot 2 \cdot (1 + s_{max})} \cdot \omega_s \quad (4.32)$$

This simplification in Equation 4.31 has shown to be inaccurate. Therefore a better proposal for the solution is given in [27]. The equation is:

$$s = \frac{K \cdot K_0 \cdot \tau_{rated} \cdot s_{slip,rated}}{\tau_{load}} \cdot \left( 1 - \sqrt{1 - \frac{\tau_{load}^2}{K_0 \cdot \tau_{rated}}} \right) \quad (4.33)$$

where the coefficient  $K$  and  $K_0$  is found from the following relation:

$$\tau_{max} = K_0 \cdot \tau_{rated} \quad (4.34)$$

$$\frac{s_{max}}{s_{rated}} = K = K_0 \sqrt{K_0^2 - 1} \quad (4.35)$$

The slip and torque estimator is simulated in the model in order to verify the accuracy of it. Figure 4.18 shows the torque estimator and 4.19 shows the slip estimator. The torque estimator initially has overshoot but later estimates the real torque accurately, while the slip estimator .

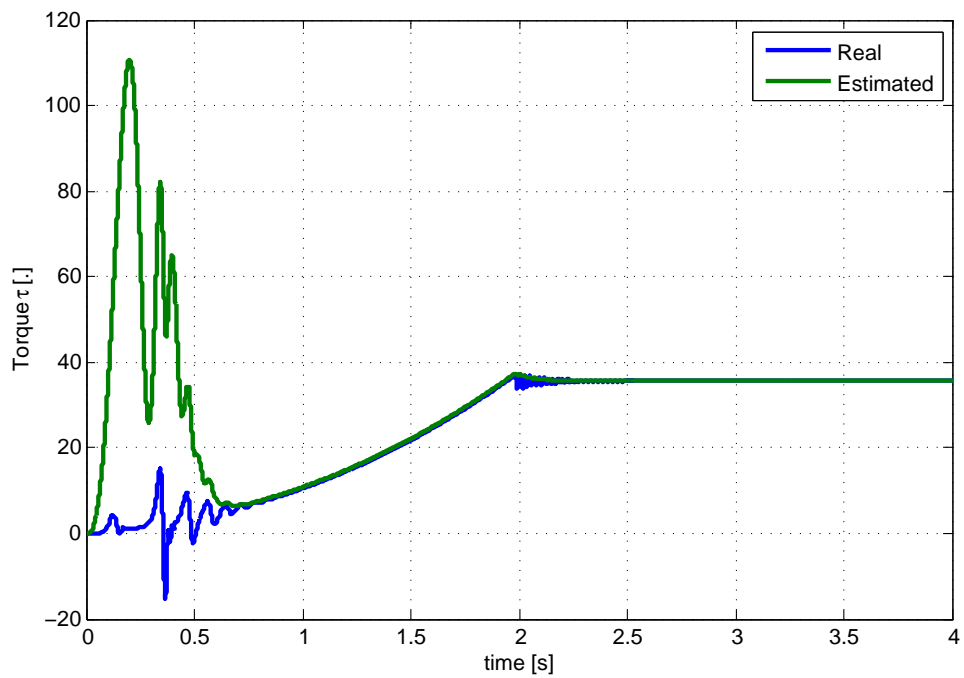


Figure 4.18: The estimated torque compared with the actual torque in the model

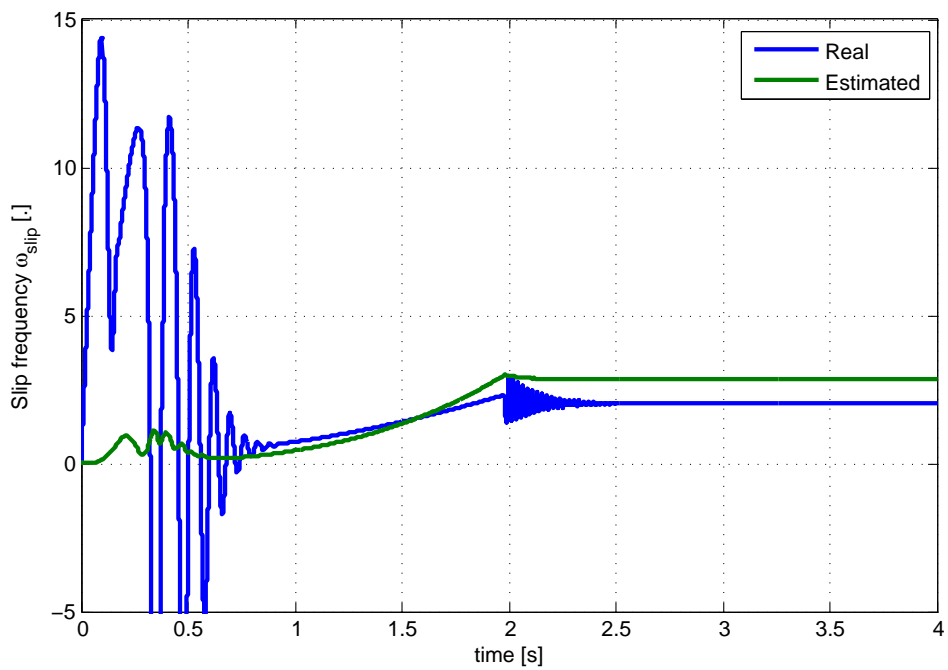


Figure 4.19: The estimated slip compared with the actual slip in the model

## 4.8 Field Oriented Control (FOC)

Field Oriented Control (FOC), which is also known as Vector Control, is a control method for Induction Motors that comes with a lot of benefits to ease closed loop control of a motor. Instead of controlling the three phase input voltages  $V_{abc}$  the controller uses Park Transformation in order to reduce the number of equations. The advantages of this transformation is that it gives access to manipulating the equation so the airgap flux linkage  $\lambda_{AG}$  is controlled through the d-axis current component  $i_d$  and torque of the motor is directly controlled by the q-axis current  $i_q$  [28]. This will be evident from the following manipulations of the general torque equation which is given in equation 4.36 for an arbitrary two phase reference frame.

$$\tau_{dq} = p_b \cdot \frac{p_b \cdot m}{2} \cdot L_m \cdot \text{Im}(i_s^* \cdot i_r) \quad (4.36)$$

Inserting the d and q components of the stator and rotor currents in the torque equation yields the result given in equation 4.37 as a result of the following derivation.

$$\begin{aligned} \tau_{dq} &= \frac{p_b \cdot m}{2} \cdot L_m \cdot \text{Im}((i_{sd} + j \cdot i_{sq})^* \cdot (i_{rd} + j \cdot i_{rq})) \\ &= \frac{p_b \cdot m}{2} \cdot L_m \cdot \text{Im}((i_{sd} - j \cdot i_{sq}) \cdot (i_{rd} + j \cdot i_{rq})) \\ &= \frac{p_b \cdot m}{2} \cdot L_m \cdot \text{Im}((i_{sd} - j \cdot i_{sq}) \cdot (i_{rd} + j \cdot i_{rq})) \\ &= \frac{p_b \cdot m}{2} \cdot L_m \cdot \underbrace{(i_{rq} \cdot i_{sd} - i_{sq} \cdot i_{rd})}_{(1)} \end{aligned} \quad (4.37)$$

This expression for the motors torque is not easy to handle, since rotor currents are needed. Instead, it is desired that the underlined part (1) of the torque equation is modified in order to avoid any rotor variables (fluxlinkage  $\lambda_r$  and current  $i_r$ ). Looking at the general equation of the induction motor given in section 2.5 shows that there are various possibilities. One is given using the imaginary part of the stator flux multiplied with the conjugated stator current, see 4.39.

$$\text{Im}(i_{dqs}^* \cdot \lambda_{dqs}) = \text{Im}((i_{sd} + j \cdot i_{sq})^* \cdot (\lambda_{sd} + j \cdot \lambda_{sq})) \quad (4.38)$$

$$\begin{aligned} &= i_{sd} \cdot \lambda_{sq} - i_{sq} \cdot \lambda_{sd} \\ &= i_{sd} \cdot (L_s \cdot i_{sq} + L_m \cdot i_{rq}) - i_{sq} \cdot (L_s \cdot i_{sd} + L_m \cdot i_{rd}) \\ &= i_{sd} \cdot L_m \cdot i_{rq} - i_{sq} \cdot L_m \cdot i_{rd} \end{aligned} \quad (4.39)$$

In that way it follows that the torque equation can be replaced by the equation 4.39 thus using the stator parameters. Another approach is to attach the qd-reference frame to the airgap flux, and then derive the torque equation given as the stator currents and the conjugated rotor flux linkages, see figure 4.20

Figure 4.20: A qd-reference frame attached to the airgap flux linkage vector

When the reference frame follows the airgap flux, the whole flux will be given in  $\lambda_{rd}$  and as a result the

perpendicular component  $\lambda_{rq}$  will be zero. This can also be observed from the previous figure, hence the torque equation reduces to the following expression.

$$\tau = \frac{p_b \cdot m}{2} \cdot \frac{L_m}{L_r} \cdot i_{qs} \cdot \lambda_{rd} \quad (4.40)$$

As it follows from the equation, the torque is controlled by the stator current and the rotor flux in dq reference frame. In order to hold the rotor flux constant, the dq-reference frame has to follow the synchronous speed. There are two ways to obtain this speed, either by measuring the rotor speed  $\omega_r$  and calculating the slip  $s \cdot \omega_e$  (indirect method) or by estimating the synchronous speed  $\omega_e$  with current and voltage measurements (direct method).

#### 4.8.1 The Indirect Field Oriented Control Method

The task is to determine the synchronous speed, so a dq reference frame can be used to obtain the values for both axis. It is assumed that the rotor speed is known either from estimation or from encoder measurement. The only thing left is to calculate the slip to fulfill the task. Since the slip is present in the rotor voltage equations, see section 2.5, this is where the derivation set off.

The voltage equations are reprinted bearing in mind that the q component of the flux linkage is zero  $\lambda_{qr} = 0$  and the rotor conductors are short circuited  $u_{dr} = u_{qr} = 0$ .

$$0 = R_r \cdot i_{dr} + \frac{d\lambda_{dr}}{dt} \quad (4.41)$$

$$0 = R_r \cdot i_{qr} + (\omega_e - \omega_r) \cdot \lambda_{dr} \quad (4.42)$$

$$\lambda_{dr} = L_r \cdot i_{dr} + L_m \cdot i_{ds} \quad (4.43)$$

$$0 = L_r \cdot i_{qr} + L_m \cdot i_{qs} \quad (4.44)$$

To estimate the slip the q-axis equations are used. The rotor current  $i_{qr}$  is isolated in equation 4.44 and inserted in equation 4.42.

$$0 = R_r \cdot \left( -\frac{L_m}{L_r} \cdot i_{qs} \right) + (\omega_e - \omega_r) \cdot \lambda_{dr}$$

Noticing that the slip can be rewritten as  $s \cdot \omega_e = \omega_e - \omega_r$  and isolating for this term yields an expression for the slip which is given in equation 4.45.

$$\begin{aligned} s \cdot \omega_e \cdot \lambda_{dr} &= R_r \cdot \frac{L_m}{L_r} \cdot i_{qs} \\ s \cdot \omega_e &= R_r \cdot \frac{L_m}{L_r} \cdot \frac{i_{qs}}{\lambda_{dr}} \end{aligned}$$

Once the slip is known the dq componants for the current vectors can be obtained, hence one component of the torque equation is at hand (stator current  $i_{qs}$ ). The other component ( $\lambda_{dr}$ ) can also be estimated by

manipulating the motor equation, here it the d-axis equations that are considered. Firstly, isolating the rotor current  $i_{dr}$  in equation 4.41 and then inserting this in the flux linkage equation 4.43 shows a first order system in the relation between the stator d-axis current  $i_{ds}$  and the rotor flux d-axis flux  $\lambda_{dr}$ , see equation 4.45.

$$\lambda_{dr} = L_r \cdot \left( -\frac{1}{R_r} \cdot \frac{d\lambda_{dr}}{dt} \right) + L_m \cdot i_{ds} \quad (4.45)$$

Taking laplace and solving for the rotor flux yields equation 4.46.

$$\begin{aligned} \lambda_{dr} \cdot \left( 1 + s \cdot \frac{L_r}{R_r} \right) &= L_m \cdot i_{ds} \\ \lambda_{dr} &= \frac{L_m}{\left( 1 + s \cdot \frac{L_r}{R_r} \right)} \cdot i_{ds} \end{aligned} \quad (4.46)$$

There will be a first-order delay defined by the time constant  $\tau = L_r/R_r$  from a stator d-axis current command is given till the airgap flux linkage is build up. When the airgap flux linkage is build, the torque can directly be controlled by the q-axis current. The block diagram of the indirect field oriented controller is given in figure 4.21 using a cascade controller with PI controllers for both current axis (dq) as the internal loop and a PI controller for the speed reference as outer loop.

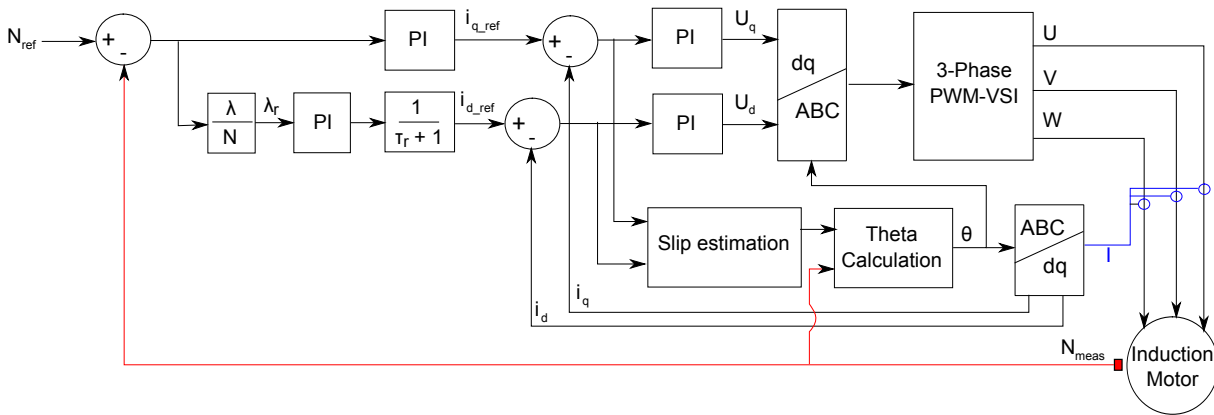


Figure 4.21: A block diagram of the indirect field oriented controller with flux and current reference created from a speed reference.

### 4.8.2 Controller design for q axis currents

The voltage stator equations for the motor will be considered in order to design a dq-axis PI current controller. These equation are laplace transformed for both axis and considered in a bodeplot. Using the bodeplot it will be possible to design the PI controllers using phase and gain margin as a goal. The values that are generally specified for a stable system and a relatively large bandwidth is 6[dB] and 45° for respectively the gain and phase margin.

The laplace transform of the stator voltage equation for the q-axis is given in equation 4.8.2 with the flux

linkages directly inserted.

$$U_{sd} = R_s \cdot I_{sd} + s \cdot (L_s \cdot I_{sd} + L_M \cdot I_{rd}) - \omega_e \cdot (L_s \cdot I_{sq} + L_M \cdot I_{rq}) \quad (4.47)$$

$$U_{sq} = R_s \cdot I_{sq} + s \cdot (L_s \cdot I_{sq} + L_M \cdot I_{rq}) + \omega_e \cdot (L_s \cdot I_{sd} + L_M \cdot I_{rd}) \quad (4.48)$$

Since the goal is to have a transfer function describing the dynamics from current to a voltage in the d and q axis, the rotor currents needs to be replaced using the rotor flux linkage equations, hence isolating the rotor currents.

$$I_{rd} = \frac{\lambda_{rd} - L_M \cdot I_{sd}}{L_r} \quad (4.49)$$

$$I_{rq} = \frac{\lambda_{rq} - L_M \cdot I_{sq}}{L_r} \quad (4.50)$$

Inserting equation and in equation and , respectivelly yields.

$$U_{sd} = R_s \cdot I_{sd} + s \cdot \left( L_s \cdot I_{sd} + L_m \cdot \frac{\lambda_{rd} - L_m \cdot I_{sd}}{L_r} \right) - \omega_e \cdot \left( L_s \cdot I_{sq} + L_m \cdot \frac{\lambda_{rq} - L_m \cdot I_{sq}}{L_r} \right) \quad (4.51)$$

$$U_{sq} = R_s \cdot I_{sq} + s \cdot \left( L_s \cdot I_{sq} + L_m \cdot \frac{\lambda_{rq} - L_m \cdot I_{sq}}{L_r} \right) + \omega_e \cdot \left( L_s \cdot I_{sd} + L_m \cdot \frac{\lambda_{rd} - L_m \cdot I_{sd}}{L_r} \right) \quad (4.52)$$

Isolating for the stator currents  $I_{sdq}$  and the rotor flux linkages  $\lambda_{rdq}$ .

$$U_{sd} = I_{sd} \cdot \left( R_s + s \cdot L_s - s \cdot \frac{L_m^2}{L_r} \right) - I_{sq} \cdot \omega_e \cdot \left( L_s - \frac{L_m^2}{L_r} \right) + s \cdot \lambda_{rd} \cdot \left( \frac{L_m}{L_r} \right) - \lambda_{rq} \cdot \omega_e \cdot \left( \frac{L_m}{L_r} \right) \quad (4.53)$$

$$U_{sq} = I_{sq} \cdot \left( R_s + s \cdot L_s - s \cdot \frac{L_m^2}{L_r} \right) + I_{sd} \cdot \omega_e \cdot \left( L_s - \frac{L_m^2}{L_r} \right) + s \cdot \lambda_{rq} \cdot \left( \frac{L_m}{L_r} \right) + \lambda_{rd} \cdot \omega_e \cdot \left( \frac{L_m}{L_r} \right) \quad (4.54)$$

The change in rotor fluxes are neglegible because of the large rotor time constant for both d and q axis which is defined by  $\tau_r = L_r/R_r$ . Furthermore, due to the dq-reference following the space vector the q component of the airgap flux linkage is zero ( $\lambda_{rq} = 0$ ). The equation reduces to the following.

$$U_{sd} = I_{sd} \cdot \left( R_s + s \cdot L_s - s \cdot \frac{L_m^2}{L_r} \right) - \underbrace{I_{sq} \cdot \omega_e \cdot \left( L_s - \frac{L_m^2}{L_r} \right)}_{(1)} \quad (4.55)$$

$$U_{sq} = I_{sq} \cdot \left( R_s + s \cdot L_s - s \cdot \frac{L_m^2}{L_r} \right) + \underbrace{I_{sd} \cdot \omega_e \cdot \left( L_s - \frac{L_m^2}{L_r} \right)}_{(2)} + \underbrace{\lambda_{rd} \cdot \left( \frac{L_m}{L_r} \right)}_{(3)} \quad (4.56)$$

The stator currents are measured and both the synchronous speed and the rotor d-axis flux linkage is

estimated equation 4.55 and 4.56 can be simplified using decoupling for term (1), (2) and (3). By decoupling it is meant that these underlined terms are added or subtracted in order to neglect these terms in the transfer function. This is illustrated in figure 4.22

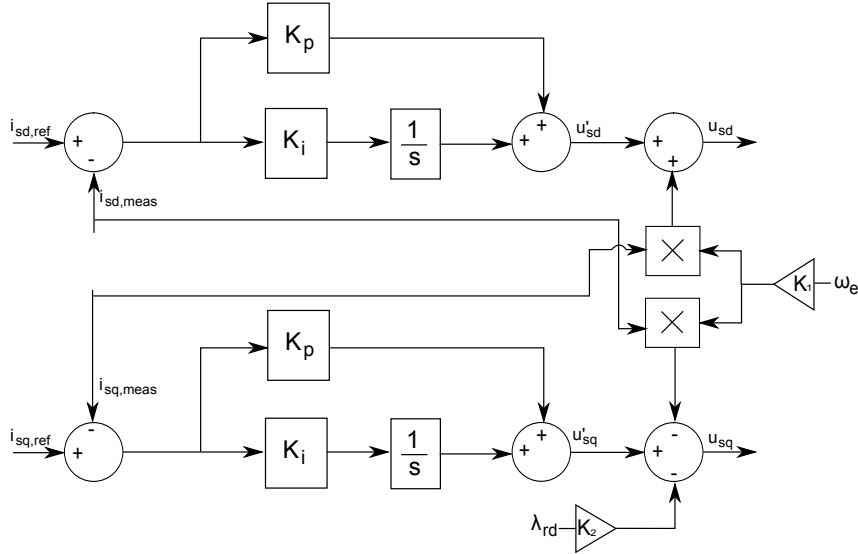


Figure 4.22: A block diagram of the decoupling in the current closed loop controllers

The final equation for the current transfer function becomes the ones given in equation 4.8.3 and 4.8.3.

$$\frac{I_{sd}}{U_{sd}} = \frac{1}{R_s + s \left( \cdot L_s - \frac{L_m^2}{L_r} \right)} \quad (4.57)$$

$$\frac{I_{sq}}{U_{sq}} = \frac{1}{R_s + s \left( \cdot L_s - \frac{L_m^2}{L_r} \right)} \quad (4.58)$$

It is seen that the transfer function for both axis is the same when using current and flux decoupling, hence the PI controller will be the same. On top of that it is noticed that it is a first order type 0 system which causes a steady state error for a step input. This steady state error is removed by the PI controller.

### 4.8.3 Determine gains from bode plot analysis

The bode plot of the transfer functions describing the relationship between input current and output voltage from equation (and equation ) is shown in figure 4.23.

The system ideally behaves as a first order system with a time constant around  $165[\mu\text{s}]$ . It has infinite gain margin and a  $90^\circ$  phase margin. The system is stable, but since it is a first order system there are no free integrators (type 0 system). As a consequence, there will be steady state error for closed loop control. In order to remove the steady state error a free integrator has to be introduced with e.g. a PI controller. Two identical PI controller are designed for the d and q axis stator currents. Also a PI controller is designed for the outer loop to control the speed reference. The system observed from this controller is similar to the current loops, due to the q-axis current directly affecting the torque. The only difference is the gain. The resulting controller becomes a closed loop cascade controller. The requirements for these type of

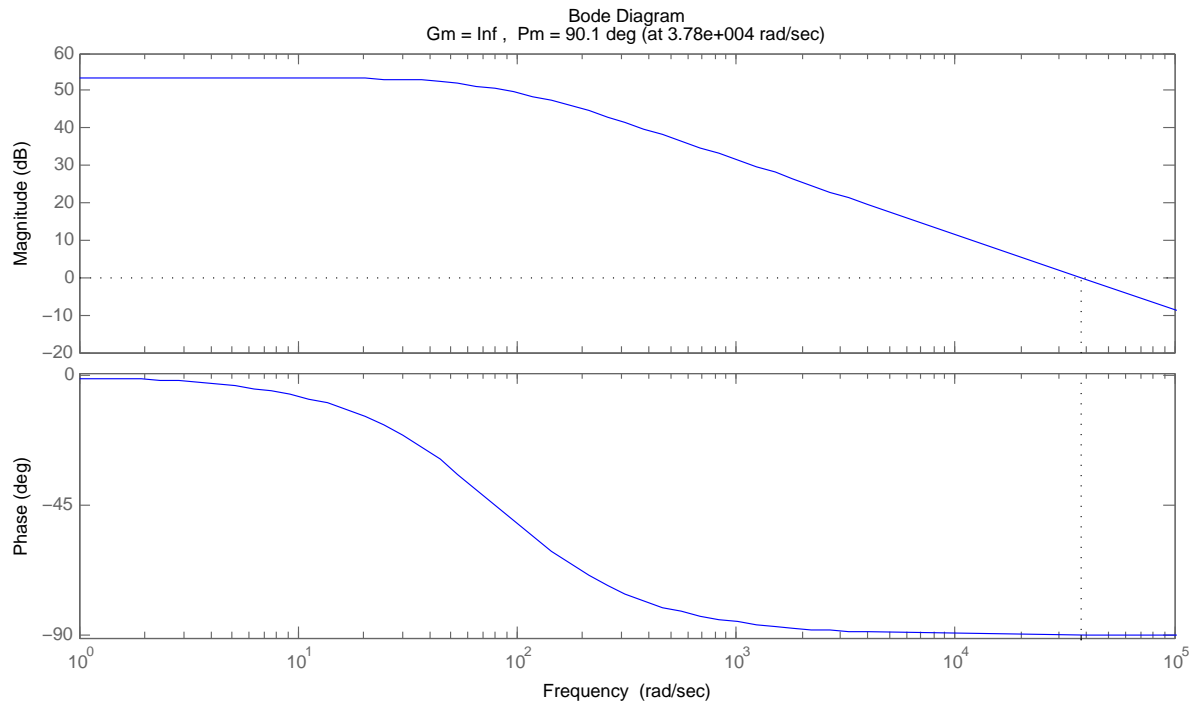


Figure 4.23: Bodeplot for the decoupled system from current to voltage in dq reference frame.

controllers are for the inner loop to be 4-5 times faster than the outer loop. This coefficient is because it approximately takes 5 time constant to reach a steady value. The controllers are designed in SISOTOOL which is a package in MATLAB. The controllers are designed for a phase margin of  $80^\circ$  and a bandwidth of  $2 * \pi * 65$  to the inner loop and 5 times less for the outer. The resulting gains are listed in table 4.8.3

The step response of the closed loop systems are plotted in figure 4.24 after adjusting the gains to obtain a desired performance. The step is a  $1[A]$  reference. Here it is seen the response of the system is fast with no steady state error. The large integral gain  $K_{i,adj}$  is naturally the cause of this response. Lowering this gain caused the step response to have undershoot and a large settling time, which is not desirable. The gain can however make it difficult to implement on a DSP. The response of the velocity reference is given in figure 4.25. Here again the controller gains are adjusted in order to track the reference. The controller has a lower settling time and tuning the gains did not help much on the settling time. Increasing the integral part results in larger overshoots.

	$K_{p,iso}$	$K_{i,iso}$	$K_{p,adj}$	$K_{i,adj}$
$i_d$	0.0105	1.24	0.4	60
$i_q$	0.0105	1.24	0.4	60
$\omega_{ref}$	2.39e-6	2.71e-4	0.6	0.5

Table 4.1: The controller gains for the field oriented controller system from SISOTOOL and the adjusted based on manual tuning.

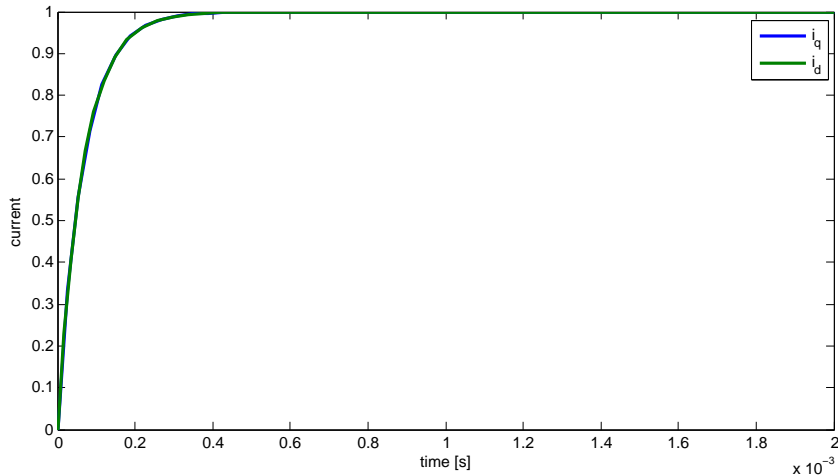


Figure 4.24: A block diagram of the indirect field oriented controller with flux and current reference created from a speed reference.PI controller output for the  $i_d$ s and  $i_q$ s axis stator currents feedback

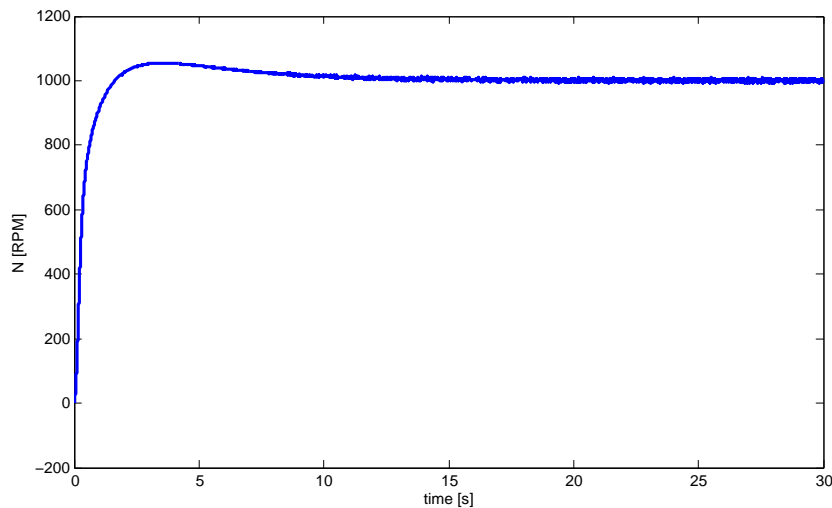


Figure 4.25: PI controller output for the velocity feedback

## 4.9 Flux Observer

The indirect field oriented controller derived in the previous section can have some limitation in the case of variation in motor parameters or in case of wrongfully estimated parameters. This will lead to reduced performance of the motor since the desired torque will not be equal to the actual torque gained from the controller. There are several methods to improve the performance of the controller.

- The flux could be measured through current measurements in a coil placed in the airgap between the stator and the rotor.
- Robust control strategies could be implemented in order to neglect the disturbances or the drift in parameter values.
- Adaptive control could be used to adapt the parameters that are uncertain or time-variant.
- An observer could be implemented in order to estimate the unknown states.

The later is chosen since the project group found it relavent based on the curriculum of the semester.

### 4.9.1 state space flux observer

As estimator it is chosen to look at whether the Luenberger, state observer can be used to estimate the rotor flux. Using a stator-fixed reference frame the state in the equations 4.59 and 4.60 can be set up. The derivation here of can be found in appendix .6.

$$\begin{bmatrix} \frac{di_s}{dt} \\ \frac{d\lambda_r}{dt} \end{bmatrix} = \left[ \begin{bmatrix} c_1 & -c_2 \\ \frac{L_m}{L_r} & -\frac{R_r}{L_r} \end{bmatrix} + \omega \begin{bmatrix} 0 & jc_3 \\ 0 & j \end{bmatrix} \right] \begin{bmatrix} i_s \\ \lambda_r \end{bmatrix} + \begin{bmatrix} -c_4 \\ 0 \end{bmatrix} u_s \quad (4.59)$$

$$y = [1 \ 0] \begin{bmatrix} i_s \\ \lambda_r \end{bmatrix} \quad (4.60)$$

The system is observable if the observability matrix  $O$  has full rank, where n is the number of states.

$$O = [C \ CA \dots CA^{n-1}]^T \quad (4.61)$$

$$CA = \begin{bmatrix} 1 & 0 \end{bmatrix} \begin{bmatrix} c_1 & -c_2 + j\omega c_3 \\ \frac{L_m}{L_r} & -\frac{R_r}{L_r} + j\omega \end{bmatrix} = \begin{bmatrix} c_1 & -c_2 + j\omega c_3 \end{bmatrix} \quad (4.62)$$

$$O = \begin{bmatrix} c_1 & -c_2 + j\omega c_3 \\ \frac{L_m}{L_r} & -\frac{R_r}{L_r} + j\omega \end{bmatrix} \quad (4.63)$$

because  $\omega$ , cannot take imaginary values the observability matrix has full rank, and the system is thus observable.

As estimator the Luenberger estimator is here used.

$$\bar{x} = A\bar{x} + Bu + L_p(y - C\bar{x}) \quad (4.64)$$

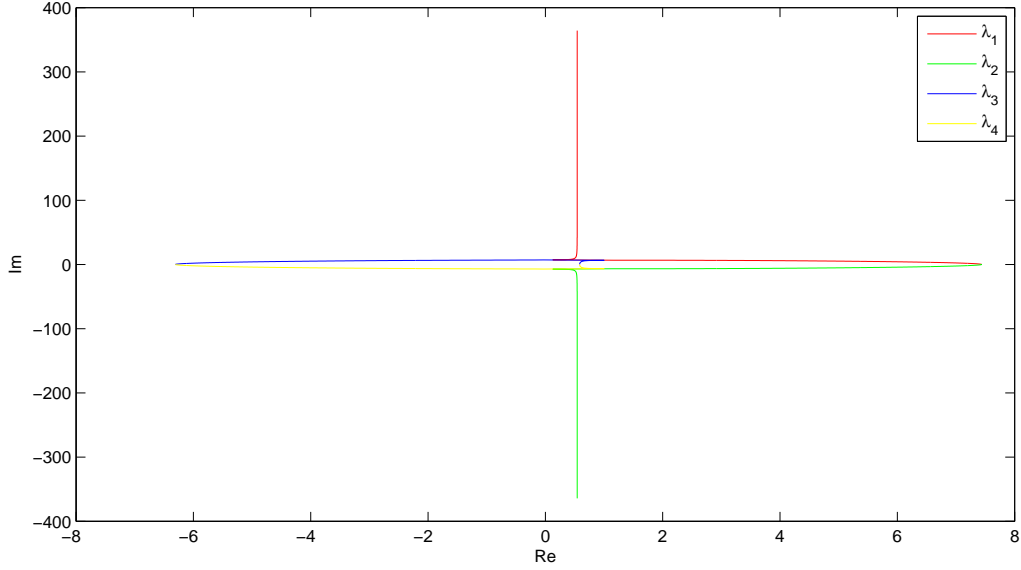
The estimator gain,  $L_p$ , is found by poleplacement. The estimator poles are placed 20 times faster then the fastest system poles. Figure 4.26 shows the poles of the system as  $\omega$  takes on the values from 0 to nominel velocity,  $\omega_{nom}$ .

The eigenvalues at  $\omega = 0$  and  $\omega = \omega_{nom}$  are given by

$$\lambda_{\omega=nom} = 1.0e+002 \{-0.8023 + j3.6442; -0.8023 - j3.6442; 0.0100 + j0.0000; 0.0100 - j0.0000\} \quad (4.65)$$

$$\lambda_{\omega=0} = \{0.9999; -80.2310; 0.9999; -80.2310\} \quad (4.66)$$

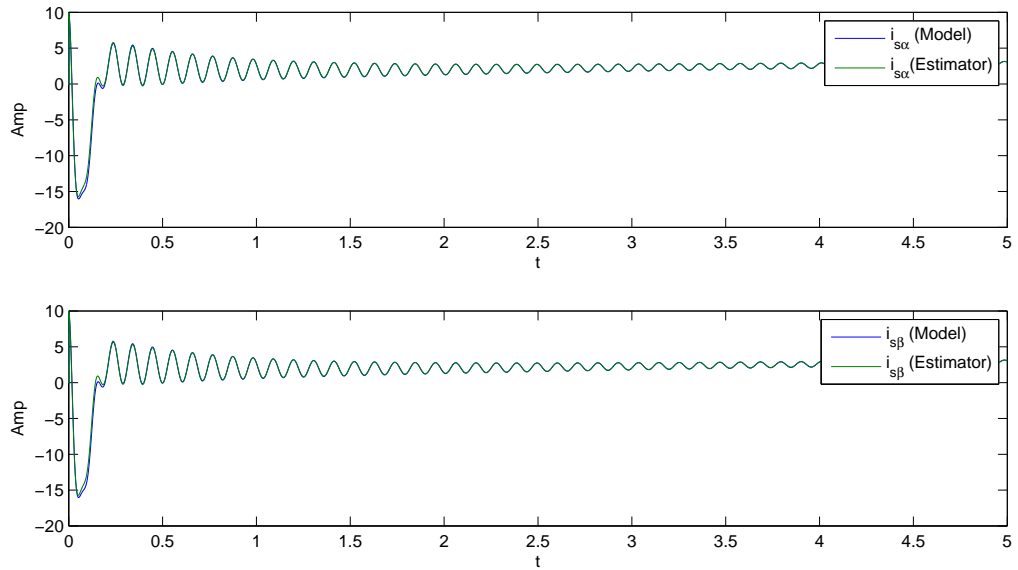
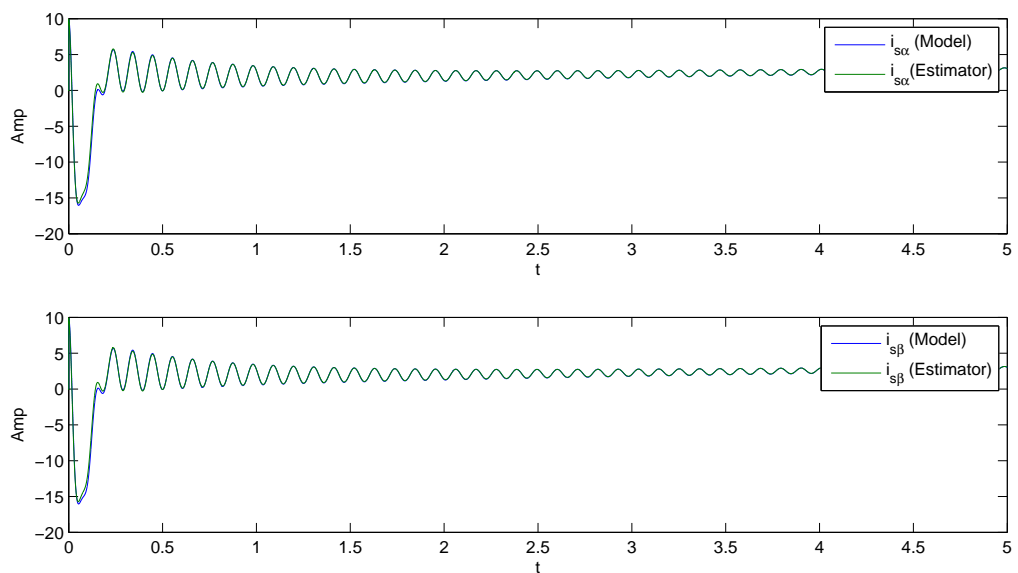
In order for the estimator to be fast enough the estimator poles are placed as 20 times the  $|\lambda_{\omega=nom}|$  at dampning of 0.7 in the left half plane of the S-domain. Figures 4.27 and 4.28 shows the currents of the

Figure 4.26: the eigenvalues in the range  $[0 \omega_{nom}]$ 

motor based on the model and the estimator at  $\omega = 0.1$  and  $\omega = \omega_{nom}$  respectively.

As can be seen the estimation of the current works to satisfaction. However, when looking at the flux in figures 4.29 and 4.30 it is not too satisfactory. It has been tried to place the poles as faster, slower and with less and more damping though still with out improving results.

Besides not working in this case the Luenberger observer also has another problem. The problem with this strategy is that for low values of  $\omega$ , the observer maybe be too fast. The fast observer leads to  $L_p$  having large values, which means that the sensitivity to disturbances and noises are also increased. It is therefore proposed in [29] that an Extended Kalman Filter instead is implemented to update the estimator gain,  $L_p$ , online.

Figure 4.27: Estimated  $i_{s\alpha}$  and  $i_{s\beta}$  at  $\omega = \omega_{nom}$ Figure 4.28: Estimated  $i_{s\alpha}$  and  $i_{s\beta}$  at  $\omega = 0.1$

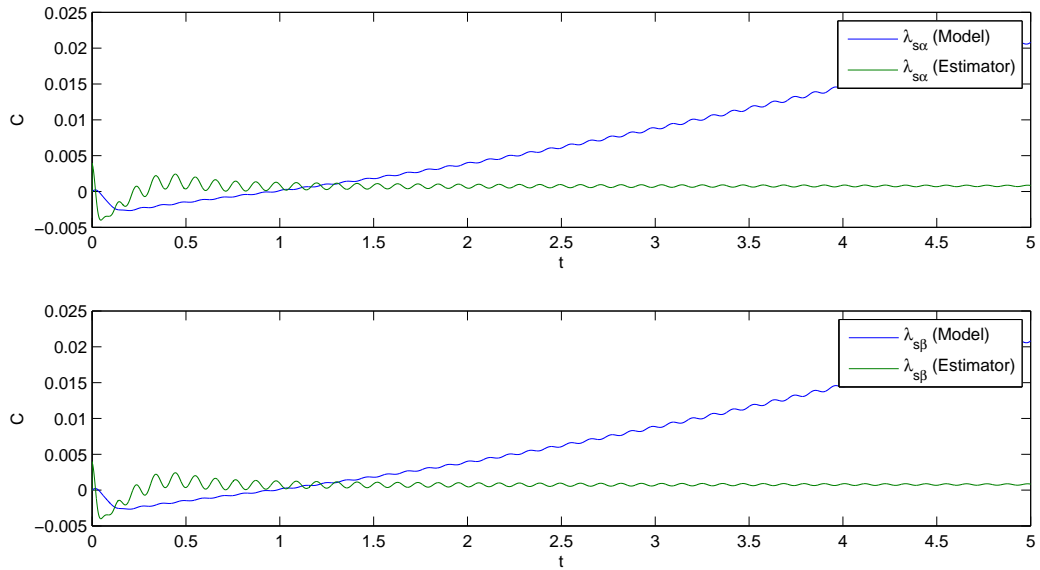


Figure 4.29: Estimated  $\lambda_{r\alpha}$  and  $\lambda_{r\beta}$  at  $\omega = \omega_{nom}$

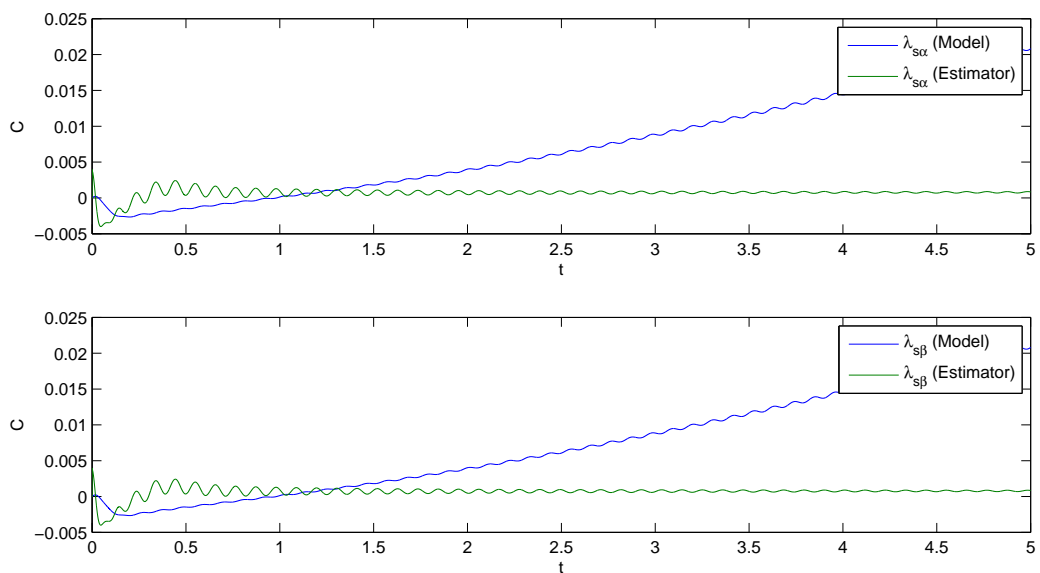


Figure 4.30: Estimated  $\lambda_{r\alpha}$  and  $\lambda_{r\beta}$  at  $\omega = 0.1$

---

# Conclusion

---

5

The objective of this project has been to convert a *Dino Leisure* go-cart that originally is delivered with a combustion engine, into a electric driven go-cart. The basic design was given from the start of the project, as the go-cart frame already was purchased for a former and similar project. Also the electric motor to implement on the go-cart was given from the start. An available *Sauer-Danfoss* induction motor, specially developed for traction operation on battery-powered vehicles was well suited for the electric go-cart.

Initially in the *System Analysis* the basic components required to design the electric drive system was presented. After investigating the design requirements for an inverter, it was decided to use an available *Sauer-Danfoss Battery Powered Inverter*, due to the limited time frame of the project. With the motor and inverter selected, the design was limited to specifying a suitable gear ratio, selecting the required batteries and dimensioning the cables needed to connect the power electronics.

To implement a controller and to generate the switching sequences of the inverter, a *Texas Instrument TMS320 C2000 Series* DSP was selected. A model of the induction motor was derived based on reference frame theory. To simulate the physical forces and reactions of the go-cart, a mechanical model was derived to be used as a load model to simulate road tests with the go-cart.

To estimate the motor parameters, the method of *Prediction-Error Minimization* have been tested with the intention of acquiring a Grey box model. However, the result of the method turned out to be unsatisfactory, as the estimated response was only valid for certain frequencies. This means, the actual parameters can not be found from the black box model obtained from this method. Another method based on *Least Mean Square* was also considered without reaching any feasible solutions.

An initial performance estimation states a steady state current draw from the batteries, at  $50[\text{km}/\text{h}]$ , of  $I_{\text{RMS}} = 34.98[\text{A}]$ . This revealed an estimated drive time of  $1.26[\text{hour}]$  based on the capacity of the batteries. This is of course a rough estimation; assuming that no accelerations are necessary.

The essential parts of the *problem statement* were to investigate different PWM modulation techniques and control strategies, in order to minimize switching/harmonic losses and to boost performance. Two different kinds of PWM techniques were investigate, continuous and discontinuous. The conclusion was to use the continuous space vector strategy for modulation indexes below  $M_{ix}$ , and one of the discontinuous above  $M_{ix}$ , dependent on the power-factor angle.

Two different controller structures were evaluated and implemented. A scalar controller with torque and slip estimation, based on the measured currents, was implemented and tested on the go-cart. Furthermore a field oriented vector controller with dq-decoupling was derived, and tested in the motor model with decent results. The vector controller was however not implemented successfully on the go-cart. The field oriented vector controller uses an estimate of the rotor flux to calculate the slip in the motor, to be used for calculating the angle for the dq-transformation. This makes the controller sensitive to estimation errors. Therefore a Luenberger estimator for the rotor flux was derived, but the estimated values were not satisfactory.

---

The go-cart was assembled with focus on the driver's safety, and the electronics were tested. A test drive was conducted, using the derived scalar controller implemented in the DSP. The go-cart reached a velocity of 38 [km/h] before the brakes had to be applied at the end of the track. In conclusion, more test drives and implementation of vector control is required to fully validate the potential performance of the go-cart.

---

# Future Work

---

# 6

---

The final test drives were performed under a very tight time schedule. This leaves room for several test to be performed during future work on the electric go-cart. Since the Vector Field Oriented Controller have shown good performance in the model, it is desirable to continue the work to get it debugged and implemented in the DSP.

The go-cart was usable to run the performed tests, but work to improve the design is needed. It turned out that the increased weight on the stiff rear axle made it very difficult to turn, due to the lack of a differential. It would be a great improvement to the handling if the axle was re-designed with a differential, or the weight reduced. The extra weight also had the effect on the frame of the go-cart that it bended slightly when subjected to shocks during drive tests, this could be improved by making the go-cart more robust.

Since the Luenberger estimator did not work, it would be interesting to see if an Extended Kalman filter might do better given that the estimator gain is updated online instead.



---

# Appendix 7

---

## .1 Inverter

### .1.1 Inverter interface PCB

The *Sauer-Danfoss BPI*, battery powered inverter, has been used for another project [20]. For that project an circuit board for interfacing the control signals from the DSP to the MOSFET drivers was designed. The PCB is seen on figure 1 where it is mounted on top of the BPI. The interface receives the PWM signals for the 3 phases through optical cables to ensure galvanic isolation for the DSP from the inverter, see description in section 2.3.4. The main purpose of the interface board is to ensure correct blanking time in the control of the MOSFETs in the tree H-bridges. The PWM signals are received by optical receivers, and converted to 5[V] logic signals. The signals are then processed by a FPGA (Field-programmable Gate Array) then sent to the upper and lower side of each canal in the inverter. The FPGA contains programmable logic that can be connected similar to more simple logic gates. The FPGA is programmed using HDL(Hardware Description Language) where the logic layout is programmed in the software, and then programmed in the memory of the FPGA.

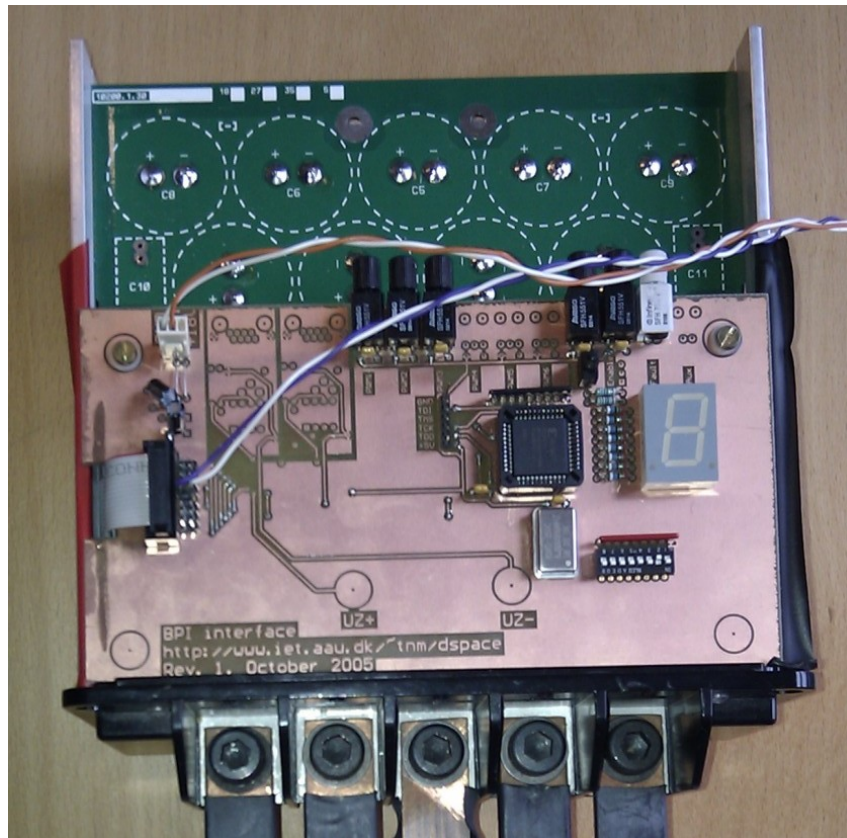


Figure 1: BPI interface PCB mounted on top of the Sauer-Danfoss inverter.

A block of DIP-switches on the interface board permits changing the blanking time, as the FPGA is programmed for different delay times between tuning on the hi-side and the low-side. The inverter has been tested with different blanking time settings to ensure optimal operation. Figure 2 and 3 shows the difference between minimum and maximum blanking time. The signals are inverted in the inverter, hence the control signals are never low at the same time instant. See section .1.1.1 for further description of the FPGA and the programming involved.

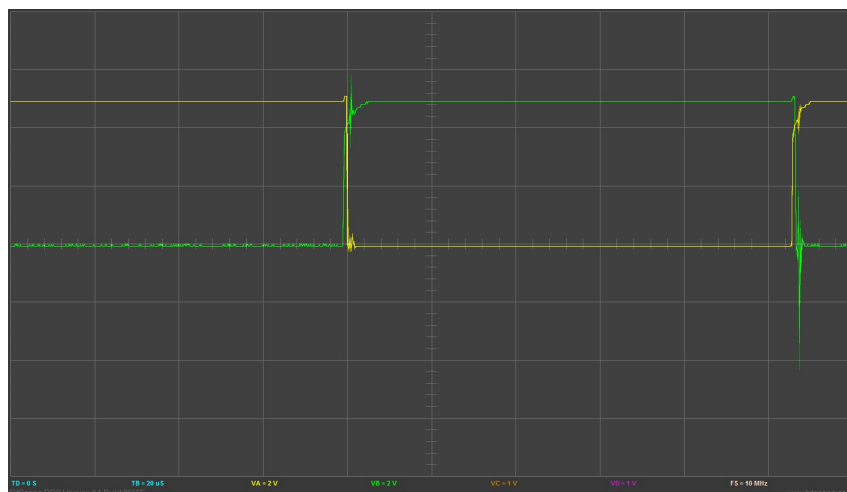


Figure 2: Screenshot of PWM signal at minimum blanking time.

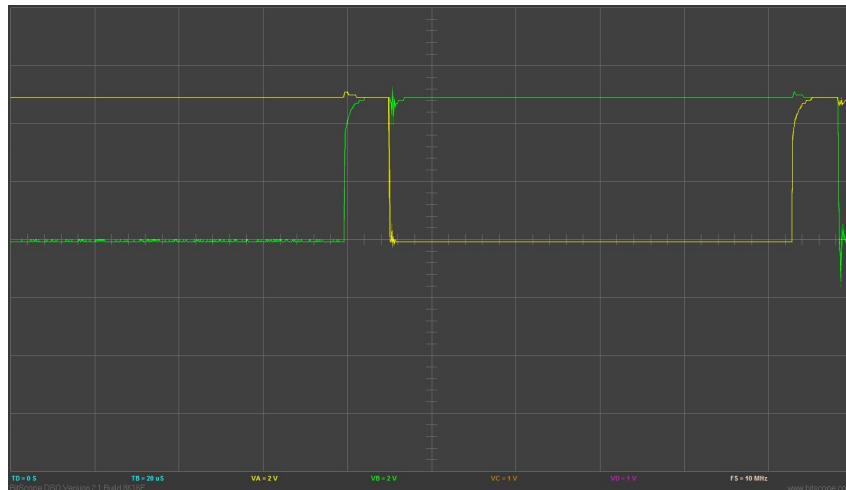


Figure 3: Screen shot of PWM signal at maximum blanking time.

The four DIP-switches allows for 16 different blanking time settings, when used binary. Table 1 shows the measured blanking times in [ $\mu\text{s}$ ].

The data sheet on the inverter has not been available, hence no data on turn-on, turn-off time for the used MOSFETs have been available for calculating the optimal blanking time. Instead a test have been made with no load connected to the inverter while a PWM signal was applied. At maximum blanking time no current was drawn from the DC supply. Then the blanking time was lowered step by step until a current draw was measured, meaning that a current was drawn directly through both the hi- and low-side MOSFET. The minimum blanking time without current draw was chosen at setting 0100, that is 3.6[ $\mu\text{s}$ ]. Blanking time

Binary switch	Blanking time [ $\mu\text{s}$ ]
0000	0.5
0001	1.6
0010	2.2
0011	2.9
0100	3.6
0101	4.2
0110	4.9
0111	5.6
1000	6.2
1001	6.9
1010	7.6
1011	8.2
1100	8.9
1101	9.6
1110	10.3
1111	10.9

Table 1: Available blanking time settings from minimum to maximum.

Furthermore the interface board contains a optical input to enable the PWM output to the inverter. A logic HI have to be applied to activate the output. The LED display on the board indicates when signal is active to the inverter.

### **.1.1.1 FPGA and VHDL programming**

A Field-programmable Gate Array (FPGA) is like a CPLD a programmable integrated circuit that contains logic gates and memory block functionalities. The FPGA is programmed using hardware description language *VHDL* and the software *Xilinx Design Studio*. Using this programming language it is possible to program a logical behavior which then will be compiled into logic gates and signals connections which will give the desired functionality. The advantage of using an FPGA is the chance to reprogram if there is a bug in the designed digital circuit. Simply, rewrite the code and reprogram the FPGA and a new digital circuit is obtained. Another advantage follows the *Xilinx Design Studio* software package. The software gives the capability to design a behavioral setup in order to test the functionality with simulation.

The purpose of the FPGA in this project is to implement a delay function on hardware level. The reason why the delay is chosen on hardware level is due to error control. If there is an error in the software caused by code or noise, it would be difficult to predict what kind of signal the DSP will send on its output ports. If a logical high signal (turn on signal) is sent to both power MOSFET's on the same leg, the consequences of this error could be destructive due to the short circuit. Therefore, to avoid putting faith in the reliability of the DSP, the security functionality is simply moved else where.

The VHDL program implemented on the FPGA is very basic. The function of the code is to take a given signal, send logical low at both output terminals, run a counter for a specific time and then send a logical high at one of the output ports. This functionality can be used to supply reference signals to two mosfets on the same leg. This will avoid both MOSFET's on the same leg to be turned on at the same time. The following code is used to setup the input and output ports of the FPGA.

```
entity dead_time is
    Port ( DTlen : in std_logic_vector (6 downto 0);
           CLK : in std_logic;
           LEG : in std_logic;
           HIGH, LOW : out std_logic);
end dead_time;
```

The *DTLen* port is used to determine the value for which the counter should count too, the *LEG* port is the port that specifies which MOSFET at the leg that should be turned on and the *CLK* signal is the clock crystal that generates a pulse for the digital circuit to run. The output ports high and low are the inverted signals one for each MOSFET in the leg.

The functionality is implemented using a state machine with the following states: *S<sub>HIGH</sub>*, *S<sub>LOW</sub>* and *S<sub>WAIT</sub>*. The function of the high and low states are basically to send a low signal on one part and a high on the other. The *S<sub>HIGH</sub>* state sends a logical high on the upper mosfet while the *S<sub>LOW</sub>* sends a logical high signal to the lower MOSFET. The essential part of the VHDL code comes in the *S<sub>WAIT</sub>* state, which is stated here:

```
when S_WAIT =>
    HIGH<= '0';
    LOW<= '0';
```

```

if DTcnt = DTlen then
    DTcnt:= 0;
    if LEG = '0' then
        Sreg0<= S_LOW;
    else
        Sreg0<= S_HIGH;
    end if;
else
    DTcnt:=DTcnt+1;
    Sreg0<= S_WAIT;
end if;

```

Until the counter *DTcnt* has reached the value specified in the input port *DTlen* (deadtime) the program will stay in the *S\_WAIT* state. Once the counter reaches the deadtime value according to value at the *LEG* input port the program will change to a state that turns one of the MOSFET's on.

This program can be programmed on an FPGA using *Xilinx* and a JTAG port. To implement this the path of the signals to each legs has to go through the FPGA.

## 2 Power supply PCB

During laboratory test the electronic control circuits can be supplied by desktop laboratory power supply's. Since the go-cart should be able to run only by on board batteries, the demand for the different voltages and currents necessary to supply the circuits have to be investigated, and a power supply PCB has to be designed.

As described in section 2.2.1, a 24[V] DC supply is available from two axillary batteries installed on the go-cart. Table 2 shows the required DC voltages for the circuits, and the minimum current demand determined from data sheets and from the laboratory test setup.

Circuit	Required DC supply [V]	Required current [mA]
Texas DSP board	5	150
Atmel MEGA328 DSP board + LCD display	5	150
Inverter interface PCB	5	300
Inverter interface PCB	18	100
Inverter current sensing PCB	$\pm 15$	500
Encoder PCB	12	100
Inverter cooling fans	12	300

Table 2: Required power supply's for control circuits.

The 12[V] and 18[V] supply are designed using 7812 and 7818 linear voltage regulators. It is possible to use a linear regulator only due to the limited current demand at these voltages.

For the 5[V] supply a *Turnigy 3[A]* DC-DC converter is used. Due to the larger voltage drop across the regulator,  $24 - 5 = 19[V]$ , and the higher current demand,  $150 + 150 + 300 = 600[mA]$ , it is decided to use this DC-DC converter with a efficiency of 92% [30] insted of a linear regulator to awoid excesive heat loss.

For the  $\pm 15[V]$  supply a *Traco Power* DC-DC converter module is used, due to the required negative

supply. The DC-DC converter delivers up to  $\pm 500[mA]$  at a efficiency of 86%[31].

The final schematic is seen in figure 4. The capacitors  $C_1-C_4$  are to eliminate electric noise. Each voltage output have been added a LED to indicate power on. The resistors  $R_6$  and  $R_7$  acts as a voltage divider of the 24[V] battery supply for the voltage not to exceed the limit of 5[V] on the Atmel MEGA328 micro processor A/D converter. This allows the driver to monitor the axillary battery voltage on the LCD display.

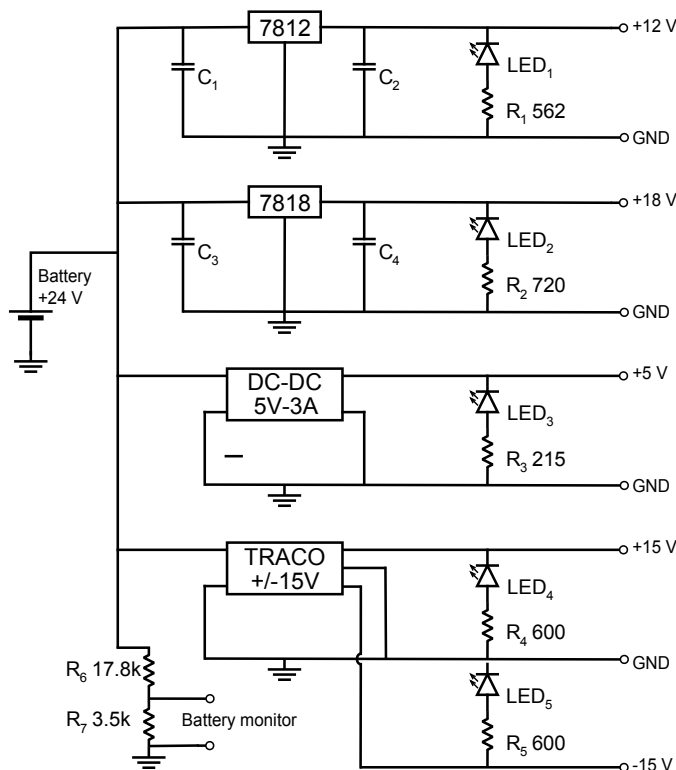


Figure 4: Schematic of power supply PCB.

The final power supply PCB is seen in figure 5, where it is mounted on the go-cart. Due to the limited time, only a prototype has been developed on a Veroboard PCB.

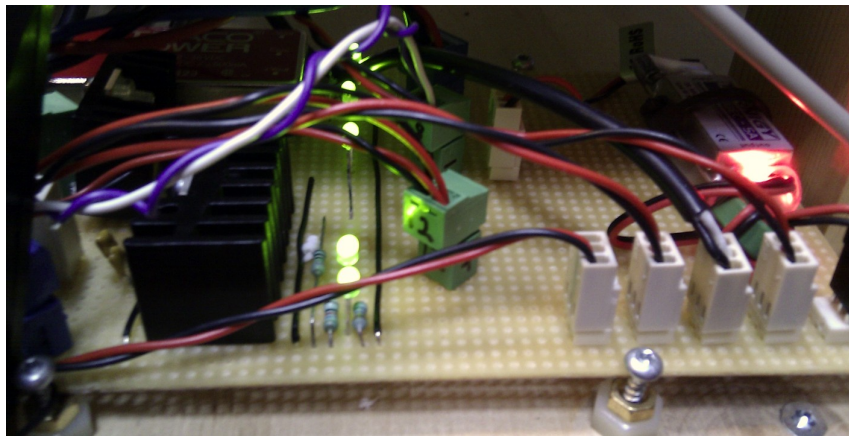


Figure 5: Power supply PCB mounted on the go-cart.

## .3 Sensors

### .3.1 Rotary encoder

For feedback control of the motor, a sensor is needed to measure the angular position of the rotor. For that use a incremental rotary shaft encoder is used. It has an internal rotating disk with slots cut out that can be read by two optical sensors, see figure 6. The sensors, and therefore the two digital outputs, are 90 degrees out of phase, as illustrated in figure 7. By decoding the signals, information about angular speed, position of the rotor and direction of rotation can be obtained and used by the DSP in the control of the motor [32]. The signals are commonly called the quadrature signals because of the 90 degrees phase shift.

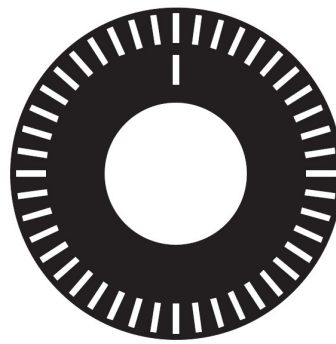


Figure 6: Incremental encoder disc [32].

When the *channel A* signal is detected to go positive before the *channel B* signal, it is most commonly defined as clockwise rotation. The opposite signal pattern hence reveals a counter clockwise rotation of the rotor.

A third sensor is used to read a home position or index signal on the encoder disc. This signal occurs only once per revolution and can be used if a absolute position is required.

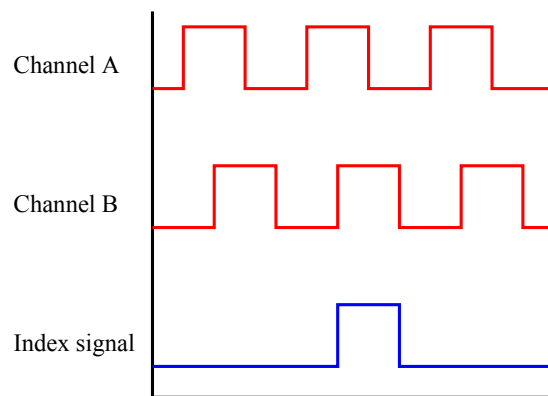


Figure 7: Pulse pattern from the incremental encoder.

The rotary encoder available for the Sauer-Danfoss motor is a *Scancon* incremental shaft encoder model R2, seen in figure 8.



Figure 8: Scancon encoder.

The main specifications of the Scancon encoder are listed in table 3.

Housing diameter	50[mm]
Max.rev.	12.000[rev/min]
Pulses pr. rev.	2000
Supply voltage	4.5 to 30[VDC]
Output signals	Standard, Inverted, Differential, 5[V]
Output waveform	Incremental (Ch. A,B and home pos.) and inverted

Table 3: Scancon encoder specifications.

The encoder is mounted directly on the rotor axis on the rear end of the motor. For the Sauer-Danfoss mo-

tor running at the rated nominal speed of 1685[rev/min], and with a encoder resolution of 2000[pulses/rev], the output frequency from the encoder will be:

$$Frequency = \frac{1685 \cdot 2000}{60} \approx 56.2[\text{kHz}] \quad (1)$$

By measuring the frequency of either channel A or B the DSP can calculate the velocity of the motor.

### **.3.1.1 Enhanced Quadrature Encoder Pulse (eQEP) Module**

The *TI TMS320 C2000* DSP is equipped with the eQEP module to be used for a direct interface with an incremental encoder. Depending on the velocity of the rotor, two different first order approximations is used to derive the velocity:

$$v(k) = \frac{x(k) - x(k-1)}{T} = \frac{\Delta X}{T} \quad (2)$$

$$v(k) = \frac{X}{t(k) - t(k-1)} = \frac{X}{\Delta T} \quad (3)$$

Where:

$v(k)$	Velocity at time instant k
$x(k)$	Position at time instant k
$x(k-1)$	Position at time instant k-1
$T$	Fixed unit time or inverse of velocity calculation rate
$\Delta X$	Incremental position movement in unit time
$t(k)$	Time instant "k"
$t(k-1)$	Time instant "k - 1"
$X$	Fixed unit position
$\Delta T$	Incremental time elapsed for unit position movement

### **.3.1.2 Signal level converting**

The *Texas Instrument TMS320 C2000* DSP that receives the encoder signals is based on 3.3[V] logic, whereas the Scancon encoder outputs 5[V] digital signals. Therefore it is required to convert the signal level from 5 to 3.3[V] logic. For that purpose a PCB is designed based on a *MC14504BCP* 6 channel, non-inverting level shifter IC. The full schematic is shown in figure 9. Only 2 channels of the level shifter IC are used for the encoder channel A and B. The voltage regulator,  $U1$ , supply the 5[V] to the logic ,as well as power to the encoder. The voltage regulator,  $U2$  regulates the 5[V] down to 3.3[V] to the output side of the level shifter IC.

### .3 Sensors

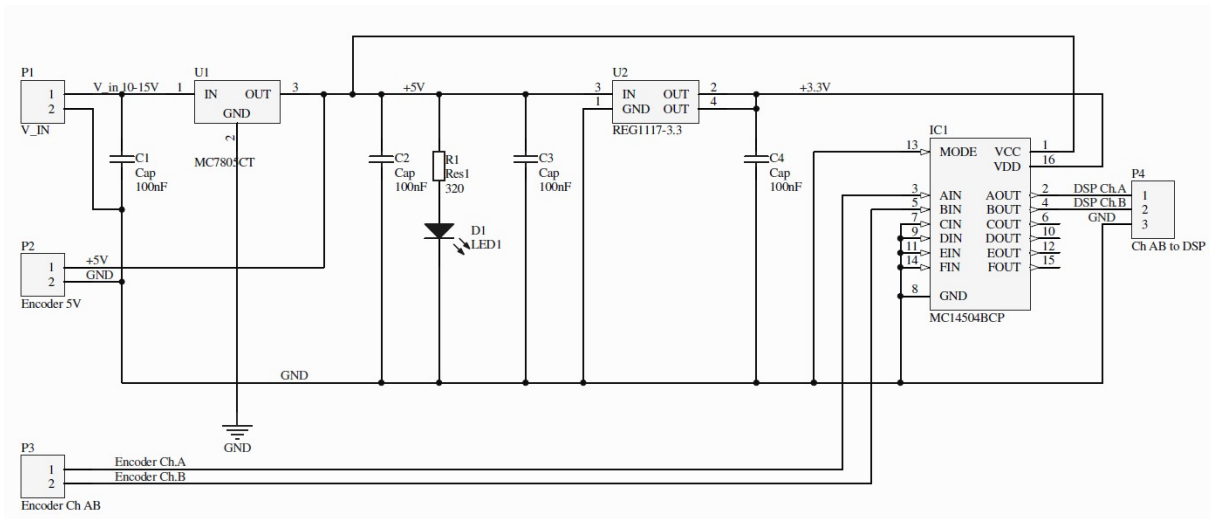


Figure 9: Scematic for signal level converting.

A green LED indicates power on the circuit. The final PCB is seen in figure 10.

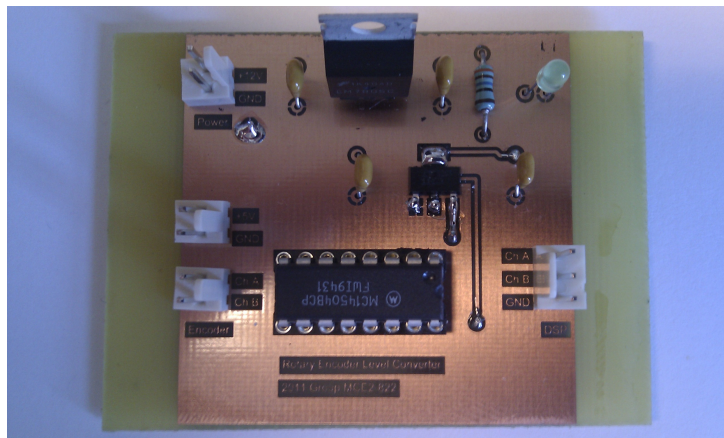


Figure 10: Encoder signal level converter PCB.

### .3.2 Current measurement - LEM-module

For closed loop control with current feedback, a sensor to measure the current is needed. For that use a current transducer *LEM LA 200-P* is used. It offers a current measurement with galvanic isolation between the high power circuit and the control circuit. The main specifications of the LEM LA 200-P module [33] are listed in table 4.

Nominal current rms	200[A]
Current measuring range	0..±300[A]
Supply voltage	±12..15[V]
Conversion ratio	1 : 2000[.]
Frequency bandwidth(-1dB)	DC..100[kHz]

Table 4: Current transducer LEM LA 200-P specifications.

The LEM module converts the current passing through by a ratio of 1:2000, and outputs the current on the pin  $M$ , as seen on the schematic in figure 11. To read the measured current with the A/D converter in the DSP the current has to be converted to a voltage between 0 and 3[V]. For that use the shunt resistor  $R_m$  is inserted in the circuit to produce a voltage drop. Since the AC-current measured is expected to be between -300 and +300 [A], the total span is 600[A]. The resistor  $R_m$  is calculated to be:

$$R_m = \frac{V_{ADC\_max}[V] \cdot LEM\_{ratio}[\cdot]}{I_{total}[A]} = \frac{3 \cdot 2000}{600} = 10[\Omega] \quad (4)$$

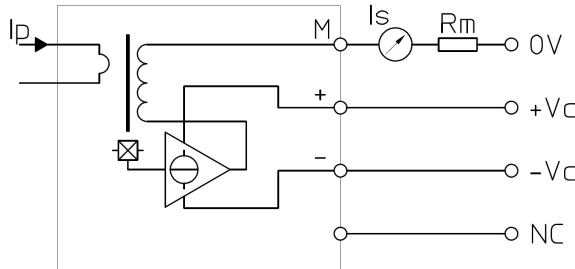


Figure 11: Scematic of the LEM LA 200-P current transducer [33].

For the complete interfacing to the DSP, the level of the current signal have to be shifted from ±1.5[V] to 0 – 3[V]. This is done using an interface PCB developed especially for AC-motor control at AAU [34]. The circuit for analog input is seen on figure 12. The voltage signal across  $R_m$  is passed through an OP-AMP,  $U4A$ , coupled as an inverting unity gain buffer. Then the signal of ±1.5[V] is passed through the second OP-AMP,  $U4B$ , also coupled as an inverting unity gain, but with the positive input locked to  $V_{ref} = 1.5[V]$ , thereby shifting the signal to 0 – 3[V] which is connected directly to the DSPs A/D Converter port.

A total of four LEM-modules are to be used. One for the DC current,  $I_{DC}$ , drawn from the battery, and one for each phase of the motor,  $I_U$ ,  $I_V$  and  $I_W$ .

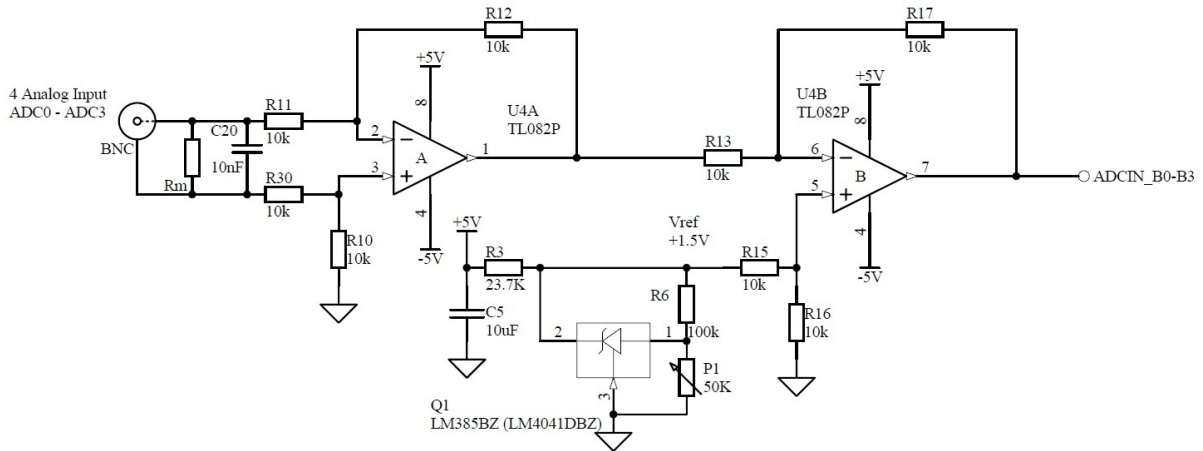


Figure 12: Level converting of current signal to the DSP.

#### .4 Derivation of the time constants for SVPWM

Over the time interval  $T_s$  the space vector  $V$  can be expressed by components  $V_1$  and  $V_2$  as seen in equation 5

$$T_s V = T_1 V_1 + T_2 V_2 \quad (5)$$

In polar coordinates this yields equation 6, where  $n$  defines the section the space vector is in.

$$T_s |V| \begin{bmatrix} \cos\alpha \\ \sin\alpha \end{bmatrix} = T_1 |V_1| \begin{bmatrix} \cos(\frac{n-1}{3}\pi) \\ \sin(\frac{n-1}{3}\pi) \end{bmatrix} + T_2 |V_2| \begin{bmatrix} \cos(\frac{n}{3}\pi) \\ \sin(\frac{n}{3}\pi) \end{bmatrix} \quad (6)$$

The size of  $V_1$  and  $V_2$  are  $\frac{2}{3}V_{dc}$ . This comes from the consideration that  $V_1$  and  $V_2$  are simply the DC link voltage scaled by the Clarke transformation amplitude invariance scaling factor. For ease of notation is used the following substitution is made

$$x = \frac{n}{3}\pi, \quad y = \frac{n-1}{3}\pi \quad (7)$$

Yielding the following set of equations

$$\begin{cases} T_s |V| \cos\alpha = T_1 \frac{2}{3} V_{dc} \cos y + T_2 \frac{2}{3} V_{dc} \cos x \\ T_s |V| \sin\alpha = T_1 \frac{2}{3} V_{dc} \sin y + T_2 \frac{2}{3} V_{dc} \sin x \end{cases} \Leftrightarrow \begin{cases} T_1 = -T_2 \frac{\cos x}{\cos y} + \frac{T_s |V| \cos\alpha}{\frac{2}{3} V_{dc} \cos y} \\ T_2 = -T_1 \frac{\sin y}{\sin x} + \frac{T_s |V| \sin\alpha}{\frac{2}{3} V_{dc} \sin x} \end{cases} \Leftrightarrow \quad (8)$$

$$\begin{cases} T_1 = \left( T_1 \frac{\sin y}{\sin x} - \frac{T_s |V| \sin\alpha}{\frac{2}{3} V_{dc} \sin x} \right) \frac{\cos x}{\cos y} + \frac{T_s |V| \cos\alpha}{\frac{2}{3} V_{dc} \cos y} \\ T_2 = \left( T_2 \frac{\cos x}{\cos y} - \frac{T_s |V| \cos\alpha}{\frac{2}{3} V_{dc} \cos y} \right) \frac{\sin y}{\sin x} + \frac{T_s |V| \sin\alpha}{\frac{2}{3} V_{dc} \sin x} \end{cases} \Leftrightarrow \quad (9)$$

$$\begin{cases} T_1 \left( 1 - \frac{\sin y \cos x}{\sin x \cos y} \right) = \frac{T_s |V| \cos\alpha \sin x - T_s |V| \sin\alpha \cos x}{\frac{2}{3} V_{dc} \sin x \cos y} = T_1 \left( \frac{\sin x \cos y - \sin y \cos x}{\sin x \cos y} \right) \\ T_2 \left( 1 - \frac{\sin y \cos x}{\sin x \cos y} \right) = \frac{T_s |V| \sin\alpha \cos y - T_s |V| \cos\alpha \sin y}{\frac{2}{3} V_{dc} \sin x \cos y} = T_2 \left( \frac{\sin x \cos y - \sin y \cos x}{\sin x \cos y} \right) \end{cases} \Leftrightarrow \quad (10)$$

$$\begin{cases} T_1 = \frac{T_s |V|}{\frac{2}{3} V_{dc}} \left( \frac{\cos\alpha \sin x - \sin\alpha \cos x}{\sin x \cos y - \sin y \cos x} \right) = \frac{T_s |V|}{\frac{2}{3} V_{dc}} \frac{\sin(x-\alpha)}{\sin(x-y)} \\ T_2 = \frac{T_s |V|}{\frac{2}{3} V_{dc}} \left( \frac{\sin\alpha \cos y - \cos\alpha \sin y}{\sin x \cos y - \sin y \cos x} \right) = \frac{T_s |V|}{\frac{2}{3} V_{dc}} \frac{\sin(\alpha-y)}{\sin(x-y)} \end{cases} \quad (11)$$

Looking at  $\sin(x-y)$  and substituting back

$$\sin(x-y) = \sin\left(\frac{n}{3}\pi - \frac{n-1}{3}\pi\right) = \sin\left(\frac{\pi}{3}\right) = \frac{2}{\sqrt{3}} \quad (12)$$

$T_1$  and  $T_2$  can now be expressed as

$$T_1 = \frac{\sqrt{3} T_s |V|}{2 V_{dc}} \sin\left(\frac{n}{3}\pi - \theta\right) \quad (13)$$

$$T_2 = \frac{\sqrt{3} T_s |V|}{2 V_{dc}} \sin\left(\theta - \frac{n-1}{3}\pi\right) \quad (14)$$

## 5 Harmonic Distortion and Switching Loss Functions

The following HDFs and SLFs are taken from [24].

### 5.1 HDFs

$$HDF_{SVPWM} = \frac{3}{2} \left( \frac{4}{\pi} M_i \right)^2 - \frac{4\sqrt{3}}{\pi} \left( \frac{4}{\pi} M_i \right)^3 + \left( \frac{27}{16} - \frac{81\sqrt{3}}{64\pi} \right) \left( \frac{4}{\pi} M_i \right)^4 \quad (15)$$

$$HDF_{DMAX} = 6 \left( \frac{4}{\pi} M_i \right)^2 - \frac{8\sqrt{3}+45}{2\pi} \left( \frac{4}{\pi} M_i \right)^3 + \left( \frac{27}{8} + \frac{27\sqrt{3}}{32\pi} \right) \left( \frac{4}{\pi} M_i \right)^4 \quad (16)$$

$$HDF_{DMIN} = 6 \left( \frac{4}{\pi} M_i \right)^2 + \frac{45-62\sqrt{3}}{2\pi} \left( \frac{4}{\pi} M_i \right)^3 + \left( \frac{27}{8} + \frac{27\sqrt{3}}{16\pi} \right) \left( \frac{4}{\pi} M_i \right)^4 \quad (17)$$

$$HDF_{DPWM3} = k_f^2 HDF_{DMIN} \quad (18)$$

$$HDF_{DPWMMIN} = HDF_{DPWMMAX} = \frac{k_f^2}{2} (HDF_{DMIN} + HDF_{DMAX}) \quad (19)$$

$k_f$  is a carrier frequency coefficient, due to fact that the three DPWMs do not switch for a period of 120 degrees,  $k_f$  is set to  $\frac{2}{3}$

### 5.2 SLF

$$SLF_{DPWMMIN} = SLF_{DPWMMAX} = \begin{cases} \frac{1}{2} - \frac{1}{4} \sin \varphi & -\frac{\pi}{2} \leq \varphi \leq -\frac{\pi}{6} \\ 1 - \frac{\sqrt{3}}{4} \cos \varphi & -\frac{\pi}{6} \leq \varphi \leq \frac{\pi}{6} \\ \frac{1}{2} + \frac{1}{4} \sin \varphi & \frac{\pi}{6} \leq \varphi \leq \frac{\pi}{2} \end{cases} \quad (20)$$

$$SLF_{DPWM3} = \begin{cases} 1 + \frac{1}{2}(\sqrt{3}-1) \sin \varphi & -\frac{\pi}{2} \leq \varphi \leq -\frac{\pi}{3} \\ \frac{1}{2}(\cos \varphi - \sin \varphi) & -\frac{\pi}{3} \leq \varphi \leq -\frac{\pi}{6} \\ 1 - \frac{1}{2}(\sqrt{3}-1) \cos \varphi & -\frac{\pi}{6} \leq \varphi \leq \frac{\pi}{6} \\ \frac{1}{2}(\cos \varphi + \sin \varphi) & \frac{\pi}{6} \leq \varphi \leq \frac{\pi}{3} \\ 1 - \frac{1}{2}(\sqrt{3}-1) \sin \varphi & \frac{\pi}{3} \leq \varphi \leq \frac{\pi}{2} \end{cases} \quad (21)$$

(22)

## 6 Derivation of the state space flux model

In a stator fixed reference frame the voltage and flux linkage equations are given by.

$$u_s = R_s i_s + \frac{d\lambda}{dt} \quad (23)$$

$$0 = R_r i_r + \frac{d\lambda_r}{dt} - j\omega_r \lambda_r \quad (24)$$

$$\lambda_s = L_s i_s + L_m i_r \quad (25)$$

$$\lambda_r = L_r i_r + L_m i_s \quad (26)$$

Isolating the first order term of the stator and rotor voltage equations and taking the derivative of the last

two equations.

$$\frac{d\lambda_s}{dt} = -R_s i_s + u_s \quad (27)$$

$$\frac{d\lambda_r}{dt} = j\omega_r \lambda_r - R_r i_r \quad (28)$$

$$\frac{d\lambda_s}{dt} = L_s \frac{di_s}{dt} + L_m \frac{di_r}{dt} \quad (29)$$

$$\frac{d\lambda_r}{dt} = L_r \frac{di_r}{dt} + L_m \frac{di_s}{dt} \quad (30)$$

Setting up the differential equation for  $i_s$  expressed by  $u_s$ ,  $\lambda_r$  and  $i_s$  itself.

$$\frac{di_s}{dt} = \frac{1}{L_m} \frac{d\lambda_r}{dt} - \frac{L_r}{L_m} \frac{di_r}{dt} = \frac{1}{L_m} j\omega_r \lambda_r - \frac{R_r}{L_m} i_r - \frac{L_r}{L_m} \frac{di_r}{dt} \quad (31)$$

$$= \frac{1}{L_m} j\omega_r \lambda_r - \frac{R_r}{L_m} i_r - \frac{L_r}{L_m} \left( \frac{1}{L_m} \frac{d\lambda_s}{dt} - \frac{L_s}{L_m} \frac{di_s}{dt} \right) \Leftrightarrow \quad (32)$$

$$\frac{di_s}{dt} - \frac{L_r}{L_m} \frac{L_s}{L_m} \frac{di_s}{dt} = \frac{1}{L_m} j\omega_r \lambda_r - \frac{R_r}{L_m} i_r - \frac{L_r}{L_m^2} (-R_s i_s + u_s) \Leftrightarrow \quad (33)$$

$$\frac{di_s}{dt} = \left( 1 - \frac{L_s L_r}{L_m^2} \right)^{-1} \frac{1}{L_m} j\omega_r \lambda_r - \frac{R_r}{L_m} \left( \frac{1}{L_r} \lambda_r - \frac{L_m}{L_r} i_s \right) - \frac{L_r}{L_m^2} (-R_s i_s + u_s) \quad (34)$$

For ease of notation the constants  $c_1, c_2, c_3$  and  $c_4$  are introduced.

$$\frac{di_s}{dt} = \left( 1 - \frac{L_s L_r}{L_m^2} \right)^{-1} = \frac{L_m^2}{L_m^2 - L_s L_r} \left( \frac{1}{L_m} j\omega_r \lambda_r - \frac{R_r}{L_m} \left( \frac{1}{L_r} \lambda_r - \frac{L_m}{L_r} i_s \right) - \frac{L_r}{L_m^2} (-R_s i_s + u_s) \right) \quad (35)$$

$$= \frac{R_r L_m^2 + L_r^2}{L_r (L_m^2 - L_s L_r)} i_s - \frac{L_m R_r}{L_r (L_m^2 - L_s L_r)} \lambda_r + \frac{L_m}{L_m^2 - L_s L_r} j\omega \lambda_r - \frac{L_r}{L_m^2 - L_s L_r} u_s \quad (36)$$

$$= c_1 i_s - c_2 \lambda_r + c_3 j\omega \lambda_r - c_4 u_s \quad (37)$$

Now it just remains to set up the differential equation for  $\lambda_r$  expressed by itself and  $i_s$ .

$$0 = R_r i_r + \frac{d\lambda_r}{dt} - j\omega \lambda_r = R_r (\lambda_r - L_m i_s) \frac{1}{L_r} + \frac{d\lambda_r}{dt} - j\omega \lambda_r \Leftrightarrow \quad (38)$$

$$\frac{d\lambda_r}{dt} = j\omega \lambda_r - R_r (\lambda_r - L_m i_s) \frac{1}{L_r} = j\omega \lambda_r - \frac{R_r}{L_r} \lambda_r + \frac{L_m}{L_r} i_s \quad (39)$$

In state space form the two equations can thus be written as.

$$\begin{bmatrix} \frac{di_s}{dt} \\ \frac{d\lambda_r}{dt} \end{bmatrix} = \left[ \begin{bmatrix} c_1 & -c_2 \\ \frac{L_m}{L_r} & -\frac{R_r}{L_r} \end{bmatrix} + \omega \begin{bmatrix} 0 & j c_3 \\ 0 & j \end{bmatrix} \right] \begin{bmatrix} i_s \\ \lambda_r \end{bmatrix} + \begin{bmatrix} -c_4 \\ 0 \end{bmatrix} u_s \quad (40)$$

## .7 Design of motor shaft extension

The cogwheel used for obtaining the gear ratio specified in section 2.2.3 between the motor shaft and the gocarts drive shaft has a cylindrical form while the end part of the motor shaft where the cogwheel is supposed to be mounted has a conic form. This means that cogwheel will not fit the shaft from the induction motor. Instead, a tooughtless and conic shaped cogwheel is found to fit the dimensions. The purpose of this tooughtless cogwheel is to transfer torque from one shaft to another for instance during experiments involving torque measurements. Mounting this on the motor shaft gives access to designing a new motor shaft extension with the correct dimensions and form for the cogwheel to fit in. The shaft extension is ment to be screw bolted on the tooughtless cogwheel in order to rotate with the rotor. On this extension shaft the cogwheel can be mounted. Therefore, a motor shaft extension is designed in *SpaceClaimEngineer* with three screw holes to connect the extension and the cylindrical shaped shaft extension for the cogwheel, see figure 13.

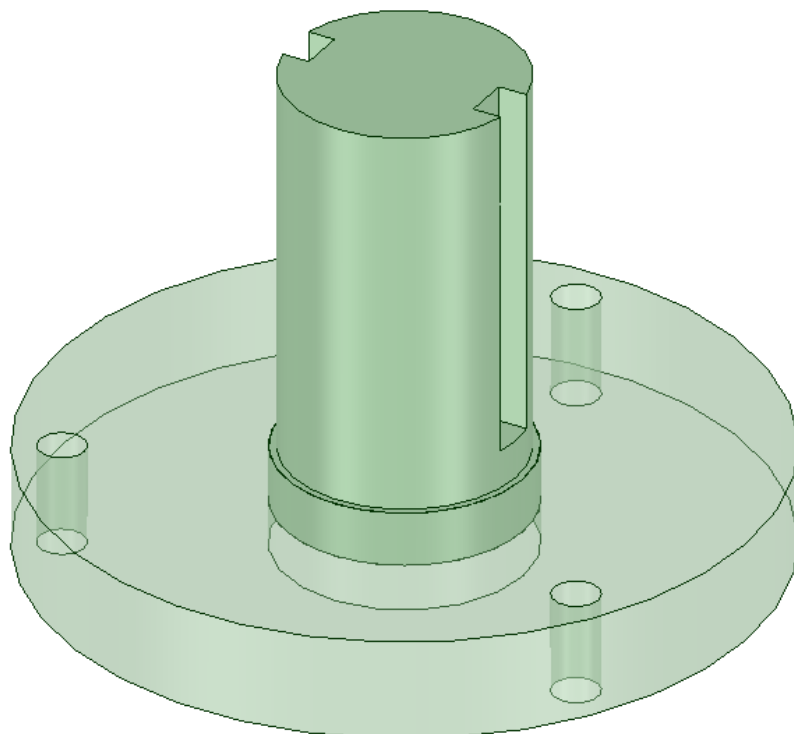


Figure 13: The motor shaft extension drawn in *SpaceClaimEngineer*.

The shaft has some holes for the splines to transfer torque from the rotor to the cogwheel and so forth. The bottom plate of the figure is the plate which is used to mount the extension shaft with the existing shaft. In the center of the plate there is a conic shaped cavity to fit with the motor shaft and three holes to be mounted on the tooughtless cogwheel on the motor shaft.

## .8 Contents of CD

The CD that comes with this report contains the following:

- Report: "Implementation and Control of an Induction Motor on a Go-cart"
- MATLAB ® m-scripts
- LabVIEW
- Datasheets
- Video of test drive



---

# Experiments

---

# A

---

## A.1 DC test

**Determine ohmic resistance in windings: ( $R_s$ )**

### A.1.1 Purpose

The purpose of the DC test is to determine the ohmic resistance of the stator winding Denoted  $R_s$  in the induction motor model section 2.5.

### A.1.2 Theory

The induction machine has three terminals which contains windings that are distributed  $120^\circ$  apart geometrically. The purpose of the windings is to create a varying electro magnetic field in order to generate a torque on the rotor. To achieve this, the supplied voltage at each terminal also has to be phase shifted by  $120^\circ$ . Each terminal is thus referred to as a phase, due to the phase shift between the supplied voltage and the geometric distribution of the windings.

Since the magnetic field of each phase ideally should be of the same magnitude, the three windings are assumed to be of the same length, yielding the same ohmic resistance for each phase. This means that it is only necessary to measure the resistance in one phase. The inductance in the windings will not cause any voltage drop when subjected to a DC current as it can be seen from Equation A.1.

$$v_L = L \cdot \frac{di_L}{dt} \quad (\text{A.1})$$

Therefore in the rest of this experiment description the voltage drop across the inductors are omitted from the equations.

### Wye or Delta connected

The Sauer Danfoss motor only has three external connectors to the windings. The rest of the connections are internal. To asses if the motor is internally wye- or delta-connected two different connection schemes are used in the experiment. One where two of the terminals are short-circuited and one where one of the terminals are floating. The two schemes and how the internal connections will be if the motor is either wye or delta connected are illustrated in Figure A.1.

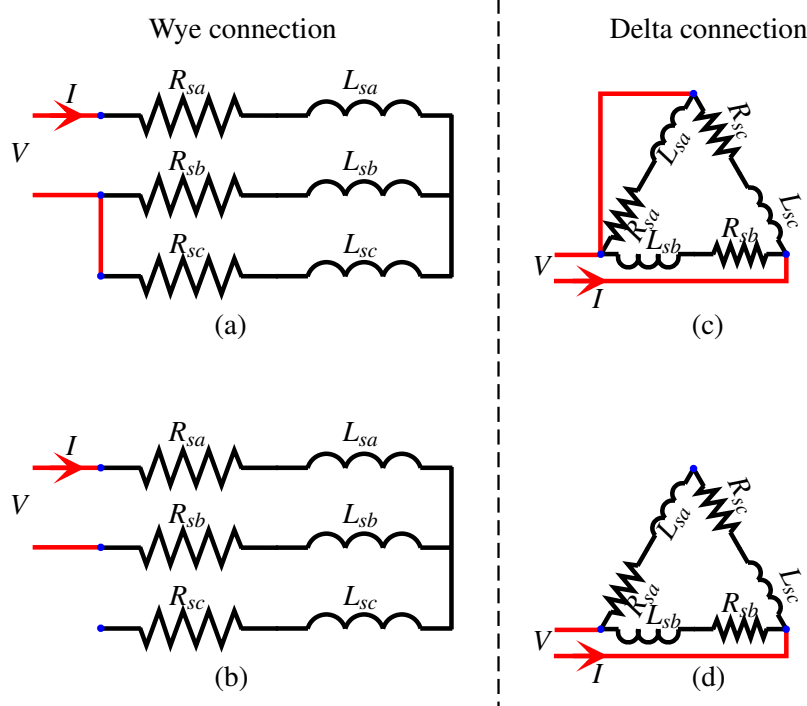


Figure A.1: Two test connection schemes to determine if the windings are wye or delta connected.  
Assumption:  $(R_s = R_{sa} = R_{sb} = R_{sc})$

In case **(a)**, where the voltage and current is known, the resistance  $R_s$  can be calculated using Ohm's law:

$$R_s = \frac{U}{I} \cdot \frac{2}{3} \quad (\text{A.2})$$

In case **(b)**, the resistance  $R_s$  is described by:

$$R_s = \frac{U}{I} \cdot \frac{1}{2} \quad (\text{A.3})$$

In case **(c)**, the resistance  $R_s$  is described by:

$$R_s = \frac{U}{I} \cdot 2 \quad (\text{A.4})$$

And finally in case **(d)**, the resistance  $R_s$  is described by:

$$R_s = \frac{U}{I} \cdot \frac{3}{2} \quad (\text{A.5})$$

The calculated resistances from **(a)** and **(b)** are then compared. As are the ones from **(c)** and **(d)** in order to determine the internal connections.

### A.1.3 Equipment

Equipment used to test the motor are listed in the table below.

Equipment	Description	AAU Number
Delta Eletronika SM45-140	Power supply	87766
Lenovo T500	Laptop to run Labview	77657
NI USB-6215	National Instruments interface for sampling data	74293
Fluke 179	Multimeter, used to calibrate measurements	83306

### A.1.4 Procedure

1. Connect the voltage source to the terminals as illustrated in Figure A.1(a).
2. Apply low voltage.
3. Log the voltage and current in the loop using Labview.
4. Connect the voltage source to the terminals as illustrated in Figure A.1(b) and repeat steps 2-3.

### A.1.5 Acquired data

The measured voltages and currents are plotted in Figure A.2

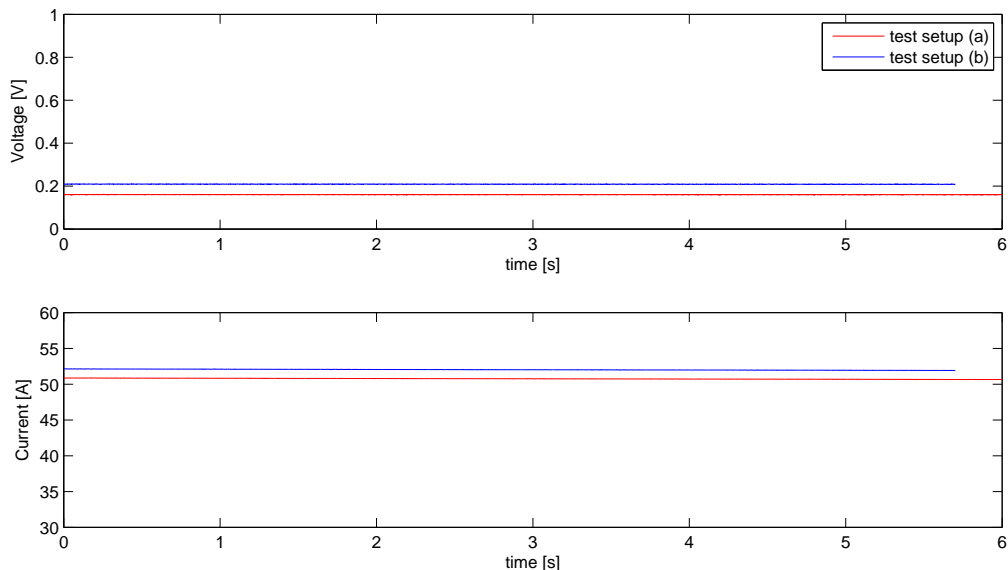


Figure A.2: Measured voltages and currents in the DC test

The mean value of the measured voltages and currents, plotted in Figure A.2 for each test setup are:

Test setup	U [V]	I [A]
(a)	0.1602	50.7281
(b)	0.2089	52.0264

Table A.1: Averaged values of the measured currents and voltages from the two test setups

### A.1.6 Data treatment

The values in Figure A.1.5 are inserted into the equations Equation A.2, Equation A.3, Equation A.4 and Equation A.5 in order to calculate the internal ohmic resistance for the different cases.

Test setup	$R_{sy}$ [ $m\Omega$ ]	$R_{s\Delta}$ [ $m\Omega$ ]
(a)	2.1053	8.0307
(b)	2.0077	6.0230

The results in the table strongly suggests that the motors windings are internally wye connected. As the calculated resistances in wye connection only differs by  $\approx 5\%$ . Where the calculated resistances in delta connection differs  $\approx 33\%$  with respect to the result from test setup (b).

### A.1.7 Sources of error

The calculated resistances in wye connection differs by  $\approx 5\%$ , in this subsection the reason for this difference is investigated.

As the voltages are measured at the terminals of the motor there should be no errors in the measured voltages.



Figure A.3: Picture of terminals on the motor in test setup (a)

The current measurements are conducted on the wire from the power supply, using a calibrated LEM module. This means that the current going through the voltage measurement in the Labview box is also measured. However as the internal resistance in the labview NI-usb-6215 is  $> 10[\text{G}\Omega]$ . So a voltage of  $\approx 0.2[\text{V}]$  as in the tests results in a current of  $< 20[\text{pA}]$ . This is not a concern as the measured currents exceed  $50[\text{A}]$ .

In test setup (a) the wire used to short-circuit two of the terminals, shown in Figure A.3, has an internal resistance. This resistance hereafter denoted  $R_l$  is neglected in the calculations of  $R_s$ . Taking this resistance into account leads to the network shown in Figure A.4, and Ohm's law of this circuit yields Equation A.6

$$\frac{U}{I} = R_s + \frac{1}{\frac{1}{R_s} + \frac{1}{(R_s+R_l)}} \quad (\text{A.6})$$

The resistance  $R_l$  a wire is given by Equation A.7.

$$R_l = \rho \cdot \frac{l}{q} \quad (\text{A.7})$$

Where:

$\rho$	Resistivity of the material	$[\Omega \cdot m]$
$l$	Length of the wire	$[m]$
$q$	Cross sectional area of the wire	$[m^2]$

The resistivity of copper at  $20^\circ C$  is  $1.68 \cdot 10^{-8} [\Omega \cdot m]$  [35]. The length of the wire is: 24 [cm], and the Cross sectional area is  $6 [mm^2]$ , yielding a resistance in the short-circuiting wire  $R_l = 0.68 [m\Omega]$ .

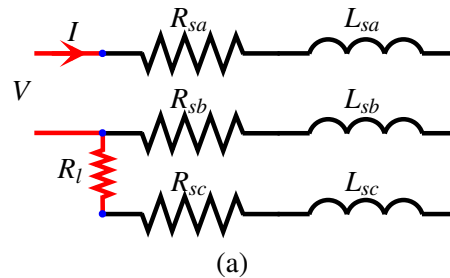


Figure A.4: Resistor network of test setup (a), when taking  $R_l$  into account. Assumption: ( $R_s = R_{sa} = R_{sb} = R_{sc}$ )

By solving Equation A.6 for  $R_s$ , yields  $R_s = 2.0083 [m\Omega]$ . This result only differs from the one obtained in test setup (b) by  $0.29 \text{ } ^\circ/\text{o}$ .

### A.1.8 Conclusion

Based on the discussions above it is concluded that the motor is wye connected, and the per phase internal ohmic resistance, to be used in the induction motor model is:  $R_s = 2.0077 [m\Omega]$ .

## A.2 Voltage measurements in labview

The phase voltages from the inverter are measured using a NI USB-6215 labview interface. This interface can measure voltages in the range of  $\pm 10[V]$ , and as the phase voltages are in the range of 0 - 48 V a voltage division is necessary. Furthermore the phase voltages are pulse width modulated at a frequency of 5 [kHz] so to sample above the Nyquist frequency a sampling frequency  $\geq 10[kHz]$ . This is not possible with the current configuration, so a low-pass filter is added to the voltage divider to allow the measurements to be more accurate. The configuration is shown in Figure A.5.

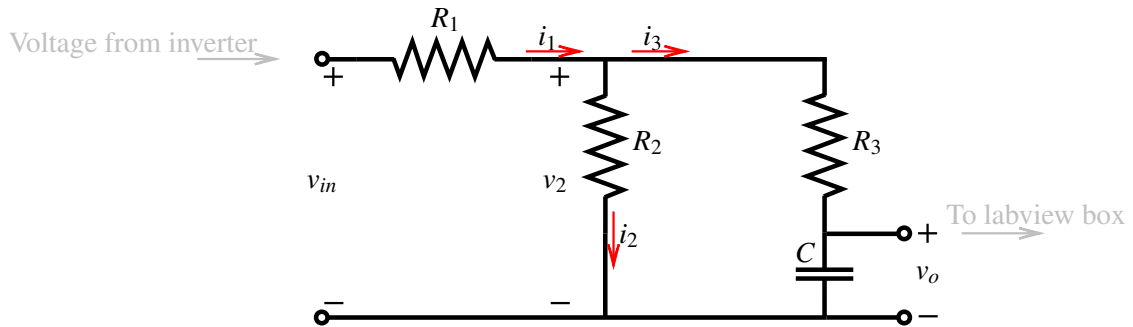


Figure A.5: Sketch of voltage divider including a low-pass filter.

To access the effects of the filter and divider the system is analyzed in the following.

Kirchoff's voltage law yields:

$$v_{in} = i_1 \cdot R_1 + i_3 \cdot R_3 + V_o \quad (\text{A.8})$$

And Kirchoff's current law gives an expression for  $i_1$  to be inserted into Equation A.8

$$i_1 = i_2 + i_3 \quad (\text{A.9})$$

$$v_{in} = (i_2 + i_3) \cdot R_1 + i_3 \cdot R_3 + V_o \quad (\text{A.10})$$

The current  $i_2$  can be described by:

$$i_2 = \frac{v_2}{R_2} = \frac{v_o + i_3 \cdot R_3}{R_2} \quad (\text{A.11})$$

And the current  $i_3$  through the capacitor can be described by:

$$i_3 = C \cdot \frac{dv_o}{dt} \xrightarrow{\text{laplace}} i_3 = C \cdot s \cdot v_o \quad (\text{A.12})$$

Inserting Equation A.11 and Equation A.12 into Equation A.10 yields:

$$v_{in} = v_o \cdot \left( \frac{R_1}{R_2} + \frac{C \cdot R_1 \cdot R_3 \cdot s}{R_2} + C \cdot R_1 \cdot s + C \cdot R_3 \cdot s + 1 \right) \quad (\text{A.13})$$

Rearranging Equation A.13 into Equation A.14 showing the first order system.

$$\frac{v_o}{v_{in}} = \frac{1}{\left( \frac{R_1}{R_2} + 1 \right) + \left( \frac{R_1 \cdot R_3}{R_2} + R_1 + R_3 \right) \cdot C \cdot s} \quad (\text{A.14})$$

The four components are selected from the following considerations.

$R_1$  and  $R_2$  constitutes the voltage divider, to allow the phase voltages ( $V_{in}$ ) to be up to  $\pm 60[V]$ , a ratio of 6:1 is necessary for the voltage divider. Assuming that  $R_3 >> R_2$  allows to select the two resistors for the voltage divider. if  $R_1 = 5.5[k\Omega] \Rightarrow R_1 = 1.1[k\Omega]$ .

To assure the assumption above is valid the value of  $R_3$  is selected to be  $\approx 50[k\Omega]$ . The only unspecified component is the capacitor, which should be dimensioned from the wanted filter characteristics. The break frequency of the system is determined by the system's pole. To ensure attenuation of the switching "noise" from the inverter the break frequency should be placed well below the switching frequency of  $5[kHz]$ . To avoid damping and phase delay of the fundamental frequency, of  $\approx 50[Hz]$ , the break frequency should be placed above this. Through testing in MATLAB ® Simulink a compromise of these two demands is found to give a break frequency( $f_{break}$ ) of 200 [Hz], making it possible to select a capacitor by using Equation A.15

$$C = \frac{\left( \frac{R_1}{R_2} + 1 \right)}{\left( \frac{R_1 \cdot R_3}{R_2} + R_1 + R_3 \right) \cdot f_{break} \cdot 2 \cdot \pi} \quad (\text{A.15})$$

Inserting the selected values into Equation A.15 gives a value for the capacitor:  $C = 15[nF]$ . A bode plot of the system is shown in Figure A.6.

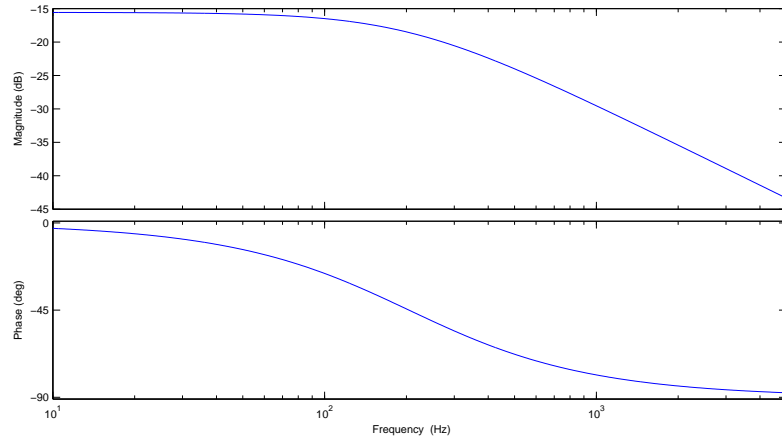


Figure A.6: Bodeplot of the voltage divider and first order low-pass filter in Figure A.5

## A.3 Test drive

### A.3.1 Final preparations

For the final test drive, the motor, the batteries and all the required electronics has to be mounted on the go-cart. To assure safety for the driver some safety features have to be implemented. Main safety priorities are:

- Secure mounting of batteries.
- Main power switch and main fuse
- Shielding of chain drive.
- Shielding of electric motor connections.

The two main batteries on each side of the driver, as well as the two auxiliary batteries mounted in the center of the go-cart have all been bolted securely to the main frame of the go-cart with custom made aluminum brackets. The auxiliary batteries have been connected up to the power supply PCB through a 2[A] fuse. The main cables connecting the main batteries have been connected up through a fuse box holding a 250[A] fuse and a main switch.

A chain guard have been fabricated with a frame of aluminum and a plywood side panel, completely shielding all moving parts from the driver.

All main power connections on the motor and the inverter have been shielded with electric isolating plastic sheets. In figure A.7 is seen the mounting for the batteries, the main fuse box with the main power switch on top, and the chain guard.

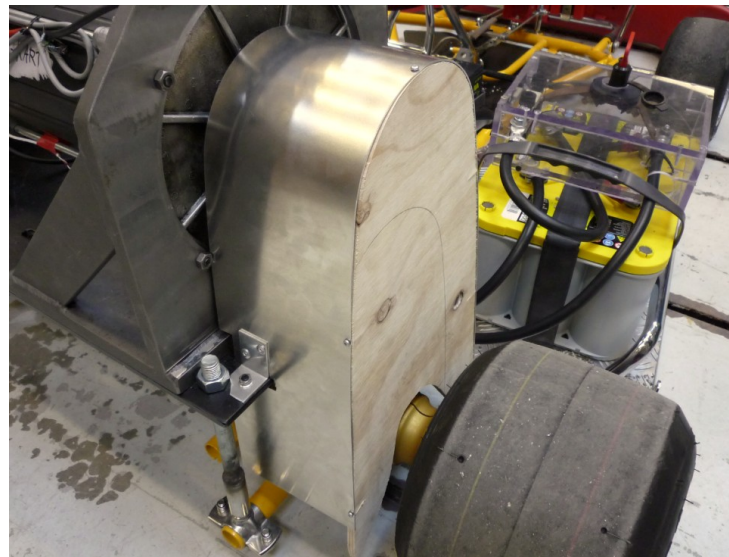


Figure A.7: Battery mountings and chain guard.

To implement the required electronics to drive the motor, a plywood plate have been mounted on top of the left main batteries. The plate is mounted to the main frame using aluminum brackets. The electronics circuits required for motor control and logging of data, that are to be mounted on the plate are:

- Sauer-Danfoss Inverter.
- Current measuring box.
- Power supply PCB.
- Main DSP with interface board.
- Encoder level converter PCB.
- Atmel DSP with LCD display.
- National Instruments 6215 interface for data logging.

Figure A.8 shows the electronics mounted on the go-cart. As seen in the photo, additional fans have been added to assure sufficient cooling to the inverter. An extra DSP have been mounted to supply information to the driver when driving. It is based on a *Atmel Mega328* DSP and is connected to a LCD display. The DSP is connected to the encoder to derive information about motor speed in [rpm] and overall speed of the go-cart in [km/h]. Furthermore the battery voltage of the auxiliary batteries are displayed together with the DC-current drawn from the main batteries. The mounting of the go-cart info display is seen in figure A.9.

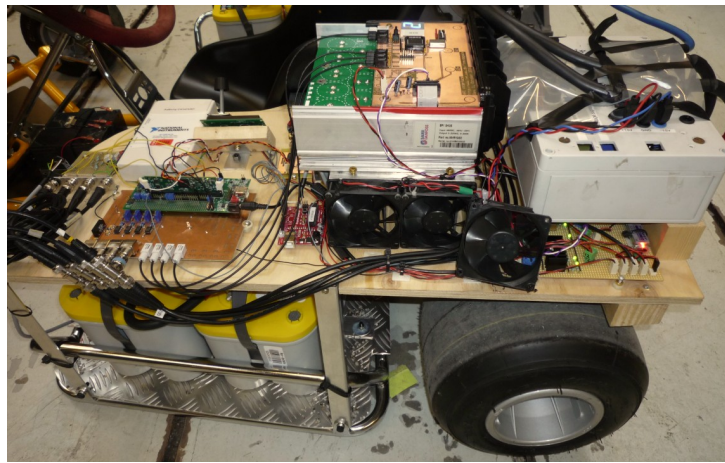


Figure A.8: Mounting of drive electronics.

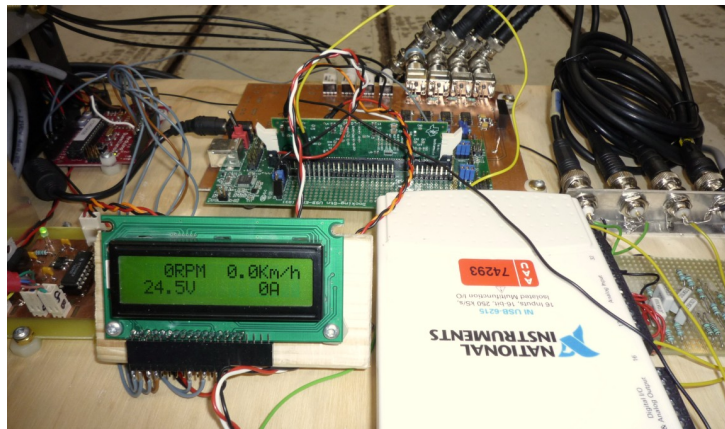


Figure A.9: Mounting of driver info display.

### A.3.2 Test drive 1 - no load/step load

To test the different controller strategies, the go-cart is first lifted from the ground to make a no-load test. The controllers are tested with ramp inputs in steps. The input reference is first raised, and then left to stabilize the speed before the input is raised further. Also a step load is tested. The motor is first accelerated up through a ramp input and left to stabilize the speed. Next a step load is applied by applying the break pedal for a period, and finally the step load is released again. The three phase currents, three phase voltages, DC voltage and current, reference input and encoder output are all logged using *LabVIEW*, running on a PC using a National Instruments 6215 interface.

The two main controller strategies to be tested are:

- Scalar Control.
- Field Oriented Control.

### A.3.2.1 Scalar Control

The implemented Scalar Controller was first limited to 10% output at the initial test. After confirming that the motor performed as expected, the output was raised first to 30% and finally to 100% .

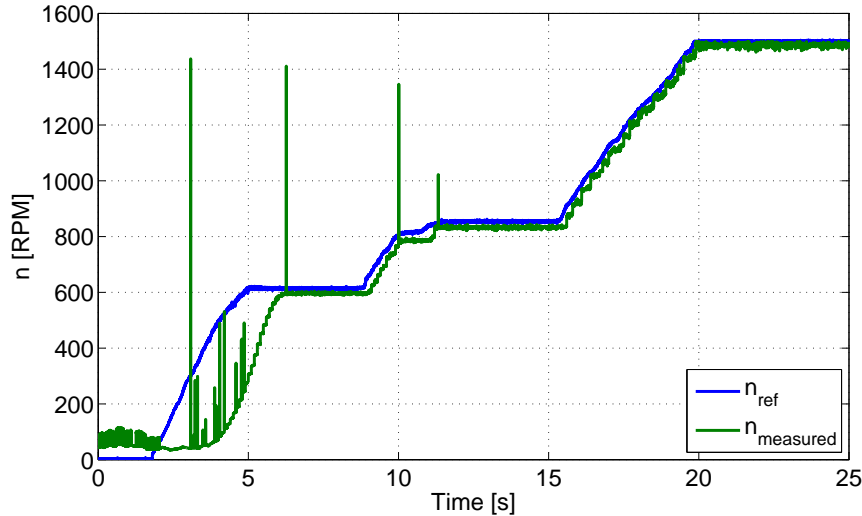


Figure A.10: Speed at ramp input in steps with Scalar Control, output limited to 30%.

In figure A.10 it is seen that the acceleration of the motor and rear wheels performs at a slower rate when the output is limited to 30% compared to figure A.11 where there is no output limit. The increase in the phase voltage as the reference speed is increased is seen in figure A.12. The spikes in the graphs for the measured speed are electrical noise on the encoder input.

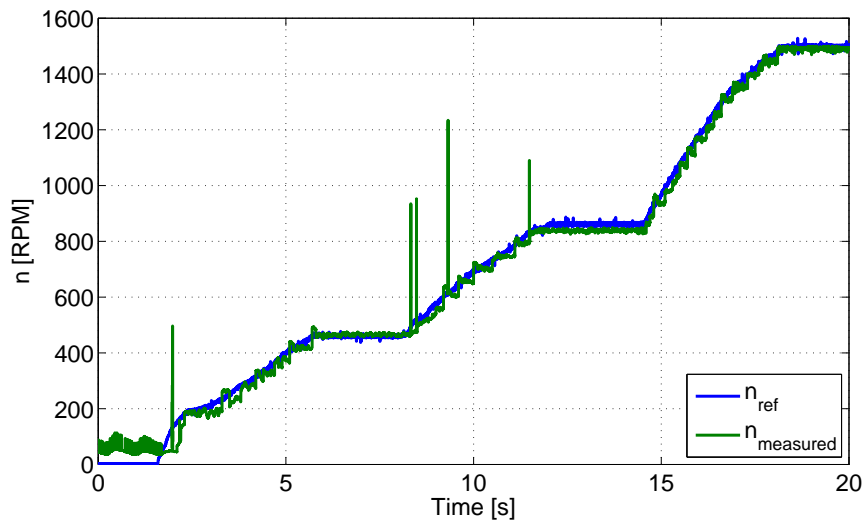


Figure A.11: Speed at ramp input in steps with Scalar Control, 100% output.

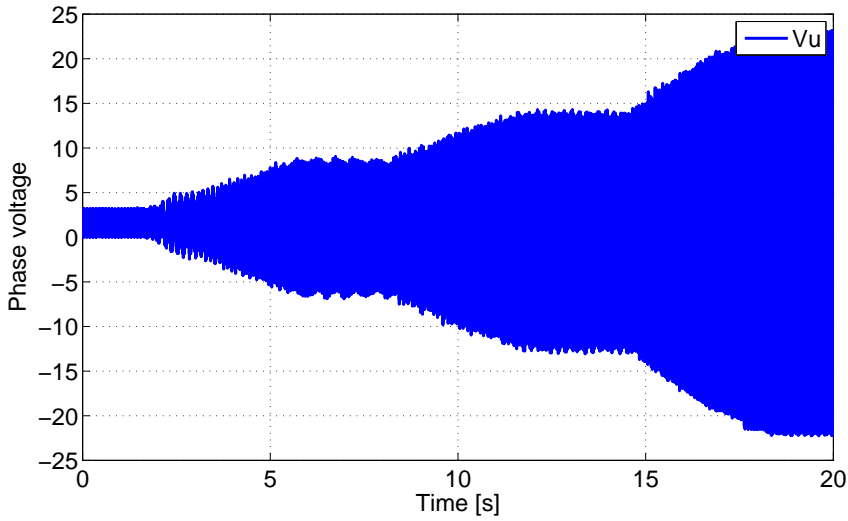


Figure A.12: Phase voltage at ramp input in steps with Scalar Control, 100% output.

Figure A.13 shows the test where a steady state speed is reached, and then a load is applied with the brake at  $Time = 3[S]$ . The drop in the measured speed is at a acceptable level considering the braking force applied. The braking force is increased until the brake is released again at  $Time = 4.5[S]$ . The result of the applied force is clearly seen in figure A.13 where the current  $I_{DC}$  is increased with the force.

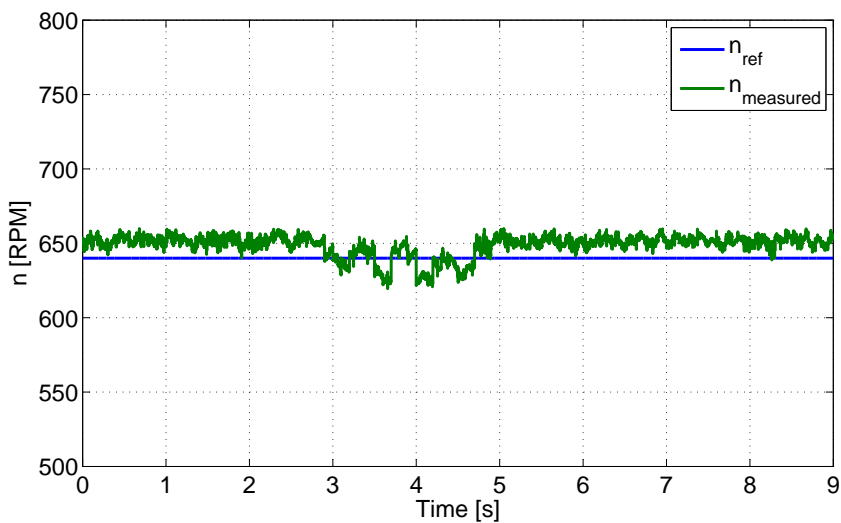


Figure A.13: Speed at step load test.

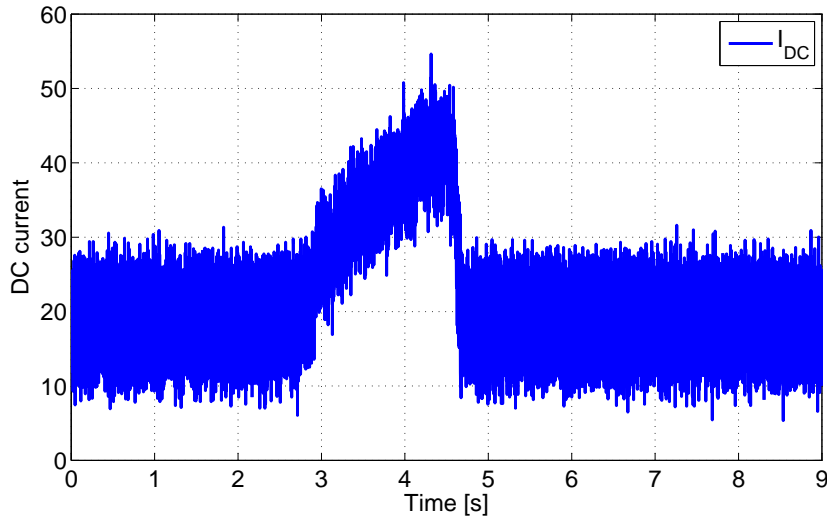


Figure A.14:  $I_{DC}$  at step load test.

Calculating the mean of the measured speed with no-load reveals 651[rpm], and 637.5[rpm] during the applied load. The deviation to the reference speed at 640[rpm] in percent can then be calculated to 1.7% and 0.4%.

### A.3.2.2 Field Oriented Control

Performing the tests with the Field Oriented Controller implemented in the DSP resulted in failure of the inverter. The Sauer-Danfoss inverter has a build-in safety circuit that turns on an output to indicate fail-mode. All output from the inverter is then stopped until a reset button is pushed.

After a thorough debugging of the C-code for the controller, some bugs were found and corrected. Unfortunately this was not enough to solve the problem during the time available for the laboratory test. As such the validation of the Field Oriented Control have not been successfully performed.

### A.3.3 Test drive 2 - acceleration test

The second and final test drive were an acceleration test of the go-cart with driver. The test was performed over a distance of approximately 150[m] on a tarmac surface. The controller was the Scalar controller without any limit in the output. It is seen that the go-cart accelerates up to 38[km/h], following the reference, without problems. After 14 seconds the test was aborted and the brakes applied, because of the limited test track.

Due to limited time this test was the final experimental test of the go-cart.

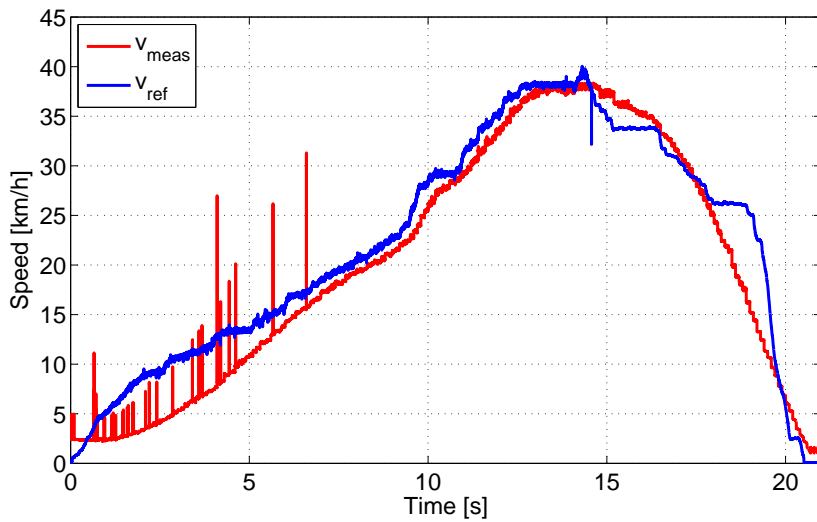


Figure A.15: Acceleration test.

#### A.3.4 Test drive conclusion

The Scalar Control of the AC-motor performed as expected. With a speed error of between 0.4 and 1.7% in the step-load test, the performance was very satisfying for an open loop controller.

The acceleration test gave a good impression of the performance of the go-cart. More Test drives are required to fully validate the performance of the go-cart, eg. top speed, drive time and steady-state power drain.

The validation of the Field Oriented Control failed due to problems with the implementation of the controller in the DSP.

# Bibliography

- [1] Den Store Danske Gylendals åbne encyklopædi. Bilisme, 2006. URL [http://www.denstoredanske.dk/Bil,\\_bbilisme](http://www.denstoredanske.dk/Bil,_bbilisme).
- [2] Klima og energi, 2011. URL <http://www.klimaogenergiguiden.dk>.
- [3] Energinet.dk, 2011. URL <http://www.energinet.dk/DA/KLIMA-OG-MILJOE/Sider/Miljoenoegletal-for-el.aspx>.
- [4] Tesla motors, 2011. URL <http://www.teslamotors.com/>.
- [5] DASU. Dasu karting, 2011. URL [http://www.dasu.dk/web/karting/karting\\_forside](http://www.dasu.dk/web/karting/karting_forside).
- [6] Dino. Dino kart, 2011. URL <http://dino.dk/>.
- [7] Sauer-Danfoss. Sauer-danfoss application note, 2004. Supplied on CD.
- [8] J.K.Thomsen J.K.Sørensen J.T.Juhl H.B Larsen J.B Jäpelt. Design of power transmission with an ac-motor. AAU EMSD8 project rapport, PDF, 2009.
- [9] C.Olesen R.Mark K.H.Henriksen M.Hvoldal. Design and control of dc-ac power transmission and implementation on a go-cart. AAU EMSD-8 project rapport, PDF, 2010.
- [10] Optima. Optima batteries - yellowtop, 2011. URL <http://www.optima-batterien.eu/optima-products/yellowtop.html>.
- [11] elfrasolen. El fra solen - batterier. WWW, 2011. URL [http://elfrasolen.dk/Support/Batterier/Batteri\\_11.htm](http://elfrasolen.dk/Support/Batterier/Batteri_11.htm).
- [12] Økonomi-og Erhvervsministeriet/ Elektricitetsrådet. Bek nr 12502 af 01/07/2001 - stærkstrømsbekendtgørelsen, afsnit 6 elektriske installationer. URL <https://www.retsinformation.dk/Forms/R0710.aspx?id=25862&exp=1>.
- [13] Vrej Barkhordarian. Power mosfet basics. URL <http://www.irf.com/technical-info/appnotes/mosfet.pdf>.
- [14] William P. Robbins Ned Mohan Tore M. Undeland. *Power Electronics - Converters, Applications and Design*.
- [15] International Rectifier. Data sheet mosfet irfp4368pbf. Datasheet available on CD.
- [16] International Rectifier. *Data Sheet No. PD60173 rev. H*.

- [17] International Rectifier. *Application Note AN-978*, 03 2007.
- [18] IPC. Ipc-2221 generic standard on printed board design, 1998. URL <http://www.jetpcb.com/Cht/Document/ipc-2221all.pdf>.
- [19] circuitcalculator.com. Pcb trace width calculator, 2011. URL <http://circuitcalculator.com/wordpress/2006/01/31/pcb-trace-width-calculator/>.
- [20] Torben N. Matzen og Erik Schaltz. Sensorless control of an ipmsm, October 2005.
- [21] Laszlo Mathe. Embedded microprocessors: Application and c programming. side 8 lectures, 2010.
- [22] *Værd at vide om frekvensomformere*. Danfoss, 1998.
- [23] M. E. Biancolini F. Renzi G. Manieri M. Urbinati. Evaluation of aerodynamic drag of go kart by means of coast down test and cfd analysis. *XXXVI Convegno Nazionale – 4-8 Settembre 2007*, side 13, 2007.
- [24] T.A.Lipo A.M.Hava R.J Kerkman. Simple analytical and graphical methods for carrier-based pwm-vsi drives. 1999.
- [25] Control Systems: Scalar Control of AC drives. Michael m. bech. 2010.
- [26] BME.HU. Asynchronous motor drives. Webpage. Timestamp 5/5-2011. URL <http://get.bme.hu/edu>.
- [27] Thomas A. Lipo Alfredo Munoz-Garcia og Donald W. Novotny. A new induction motor v/f control method capable of high-performance regulation at low speeds. 34, 1998.
- [28] Kaiyuan Lu. Advanced control of ac machines. 2011.
- [29] George C. Verghese og Seth R. Sanders. Observers for flux estimation in induction machines. 1988.
- [30] Rangevideo. Turnigy 5v dc-dc, 2011. URL [http://www.rangevideo.com/index.php?main\\_page=product\\_info&products\\_id=249](http://www.rangevideo.com/index.php?main_page=product_info&products_id=249).
- [31] Farnell. Traco power +/- 15v dc-dc, 2011. URL <http://www.farnell.com/datasheets/319814.pdf>.
- [32] Texas. Texas instruments - encoder pulse module, 2011. URL <http://focus.ti.com.cn/lit/ug/sprug05a/sprug05a.pdf>.
- [33] LEM. Current transducer la 200-p. Datasheet available on CD.
- [34] AAU Walter Neumayr Institute of Energy technology. Dsp ac-motor interface board.
- [35] Association for Science Education. Resistance and resistivity, 3/5 2011. URL <http://resources.schoolscience.co.uk/cda/16plus/copelech2pg1.html>.